Arctic cloud properties derived from ground-based sensor synergy at Ny-Ålesund

INAUGURAL-DISSERTATION

zur

Erlangung des Doktorgrades

der Mathematisch-Naturwissenschaftlichen Fakultät

der Universität zu Köln

vorgelegt von

Tatiana Nomokonova

aus

Krasnokamensk

Russland

Köln

2020

Abstract

Contemporary climate models show that clouds are one of the key components in the climate of the Arctic region experiencing rapid surface warming. Modeling of the cloud impact on the Arctic amplification is still uncertain not only because cloud life cycle is defined by large number of processes, but also because the clouds are closely related to other components of the Arctic climate, such as atmospheric water vapor, ocean, sea ice, and long-range air transport. In order to better understand the role of clouds in the Arctic, in June 2016 the French-German Arctic research station situated in Ny-Ålesund, Norway was complemented with a W-band cloud radar within the Transregional Collaborative Research Center (TRR 172) "Arctic Amplification: Climate Relevant Atmospheric and Surface Processes, and Feedback Mechanisms (AC)³". This observation site became one of a few Arctic sites capable of state-of-the-art cloud profiling with high temporal and spatial resolution. This thesis summarizes the cloud macro and microphysical properties of clouds based on the first two and a half years of cloud measurements at Ny-Ålesund. The total occurrence of clouds was found to be ∼81%. The most predominant type of clouds is multi-layer clouds with the frequency of occurrence of 44.8%. Single-layer clouds occur 36% of the time. The most common type of single-layer clouds is mixed-phase with a frequency of occurrence of 20.6%. The total occurrences of single-layer ice and liquid clouds are 9% and 6.4%, respectively. A comparison of cloud occurrence at Ny-Ålesund with a numerical weather prediction model revealed an overestimation in the occurrence of single layer ice clouds and underestimation of the occurrence of mixed-phase clouds.

The cloud properties were further related to occurrence of anomalous atmospheric conditions often caused by transport of relatively warm and moist air from the North Atlantic and circulation of dry and cold air in the Arctic region. Dry anomalies are related to about 30% less cloud occurrence with respect to normal conditions. In contrast, during moist conditions the cloud occurrence typically reaches 90–99%. Excess and shortage in water vapor typically increases and decreases the amount of condensed water in cloud, respectively. The changes in cloud properties during moist and dry anomalies in turn affect the surface cloud radiative effect (CRE). In winter, spring, and autumn the net surface CRE is dominated by the longwave (LW) CRE and, therefore, during these seasons dry and moist conditions are related to lower and higher cloud related surface warming in Ny-Ålesund, respectively. In summer, shortwave CRE becomes dominant and moist conditions cause stronger surface cooling relative to normal cases, while dry conditions tend to reduce the cloud related surface cooling.

Moist anomalies show significant positive trends varying for different seasons from 2.8 to 6.4% decade^{-1}. In contrast, the occurrence of dry anomalies has been de-

clining at rates from -12.9 to -4% decade^{-1}. A novel technique for the estimation of LW CRE developed within this study shows that the long-term trends in the thermodynamic conditions at Ny-Ålesund are related to significant positive trends in longwave CRE of 3.4 and 2.2 W m^{-2} decade^{-1} in winter and autumn, respectively. In summer, a negative trend of -1.8 W m^{-2} decade^{-1} was found, while no significant trends were found for the spring season. The database with cloud profiles obtained within this work can be used for an evaluation of numerical weather prediction models, while radiative cloud properties estimated from reanalysis models can be evaluated with long-term LW CRE retrieved with the developed method.

Zusammenfassung

Aktuelle Klimamodelle wie auch Beobachtungen zeigen, dass sich die Oberfläche der Arktis schneller erwärmt als die globals Mitteltemperature, diesen Effect bezeichnet man als "Arctic Amplicfication". Der Einfluss von Wolken auf "Arctic Amplification" ist immer noch unsicher. Dies liegt nicht nur an den vielen verschiedenen Prozesse welche zum Teil noch nicht vollständig verstanden sind, sonder auch an anderen Komponenten des Klimasystems wie Wasserdampfgehalt der Luft, Interaktion von Ozean oder Meereis mit der Atmosphäre, und dem Luftmassenferntransport in die Arktis. Um die Rolle arktischer Wolken besser zu verstehen, wurde im Rahmen des überregionalen Forschungsverbundes (TRR 172) "Arctic Amplification: Climate Relevant Atmospheric and Surface Processes, and Feedback Mechanisms (AC)^3" im Juni 2016 die deutsch-französische Forschungsstation AWIPEV um ein W-Band-Radar ergänzt. Somit ist diese Beobachtungsstation eine der wenigen in der Arktis, die "state-of-the-art" Wolkenbeaobachtungen mit hoher zeitlicher und räumlicher Auflösung ermöglichen. Diese Arbeit fasst die makro- und mikrophysikalischen Eigenschaften der Wolken in den Messungen der ersten zweieinhalb Jahre in Ny-Ålesund, Spitzbergen, zusammen. Dabei war es über 81% der Beobachtungsyeitraumes bewölkt, 44.8% der Zeit dominierten Mehrschichtenwolken beobachtet, 36% der Zeit einschichtige Wolken. Unter den Einschichtwolken traten Mischphasenwolken mit 20.6% am häufigsten auf, Eiswolken mit 9% und Wasserwolken mit 6.4%. Ein Vergleich der Auftretenshäufigkeit der verschiedenen einschichtigen Wolkenarten zwischen nummerischen Wettervorhersage und Beobachtungen in Ny-Ålesund zeigte, dass das Vorkommen von einschichtigen Eiswolken im Model überschätzt und das Auftreten von Mischphasenwolken unterschätzt wird.

Weiter wurden die Wolkeneigenschaften mit dem Auftreten von ungewöhnlichen Wetterlagen detalieiert untersucht, insbesondere dem Anomalien des integrierten Wasserdampfgehalt. Diese Anomalien werde durch den Luftmassenferntransport in die Arktis herforgerufen. Eine feuche Anomalie wird durch den Transport von warmen und feuchte Luftmassen, die mit Anströmungen vom Nordatlantik einhergehen, erzeugt, eine trockene Anomalie wird durch die arktische Zirkulationen hervorgerufen. Bei einer feuchten Anomalie kam es zu einer Wolkenauftretenswahrscheinlichkeit von 90-99% bei den trockenen Anomalien wurde 30% weniger Wolkenbedeckung beobachtet, als unter normalen Bedinungen. Die Menge von verfügbarem Wasserdampf beeinflusst die Menge an kondensiertem Wasser in der Wolke, was zu Veränderungen der microphysikalischen Wolkeneigenschaften führt und somit zu einer eine Veränderung des "Cloud radiative effect" (CRE) am Boden. Im Winter, Frühling und Herbst ist der netto CRE in Ny-Ålesund vor allem von der langwelligen Strahlung abhängig und bringen so eine stärkere Oberflächenerwärnung während negativer Feuchteanomalien mit sich. Im Sommer hat die kurzwellige

Strahlung einen größeren Einfluss. Wolken, die während positiver Feuchteanomalien auftreten haben einen negativen CRE und während negativer Feuchteanomalien verringert sich die Kühlung, die mit den Wolken in dieser Jahreszeit einhergeht. Positive Feuchteanomalien zeigen je nach Jahreszeit positive Trends zwischen 2,8 und 6,4% pro Dekade. Im Gegensatz dazu nimmt die Auftretenshäufigkeit der negativen Feuchteanomalien mit -12,9 bis -4% ab.

In dieser Arbeit wurde eine neue Methode zur Abschätzung des langwellingen CRE entwickelt. Es konnte gezeigt werden, dass der langfristige Trends der thermodynamischen Bedingungen in Ny-Ålesund mit dem signifikanten positiven Trends des langwellingen CRE im Winter (3,4 W/m^{-2} pro Dekade) und Herbst (2,2 W/m^{-2} pro Dekade) in Verbindung steht. Im Sommer wurde eine Abnahme des langwellige CRE um 1,8 W/m^{-2} pro Dekade ermittelt wo hingegen sich für den Früling kein signifikanter Trend zeigte. Dieser Datensatz, mit den hier abgeleiteten Wolkenprofilen, kann auch zukünftig genutzt werden um numerische Wettermodelle zu evaluieren. Ebenfalls können die Strahlungseigenschaften aus der in dieser Arbeit entwickelten Methode benutzt werde um Reanalysedaten abgeleiteten langwelligen CRE zu verglichen.

Contents

Chapter 1

Introduction

It is well known that during the past 3 decades the Arctic climate has been drastically changing. The change in the annual near-surface temperature over the Arctic region has been found to be a factor of 2 to 3 larger compared to the global average (Solomon et al., 2007; Wendisch et al., 2017). In the period 1998–2012, the temperature increase in the Arctic was persistent in contrast to the "hiatus" in the global warming having been discussed in a number of studies (Wei et al., 2016; Huang et al., 2017).

This amplification of warming in the Arctic is caused by several feedback mechanisms. Among them are the reduced sea ice extent and high sea surface temperature (Serreze et al., 2011; Hegyi and Taylor, 2018), changes in the atmospheric circulation (Maturilli and Kayser, 2016; Overland et al., 2016; Overland and Wang, 2016; Wu, 2017) and energy transport (Graversen and Burtu, 2016; Hwang et al., 2011), surface albedo effect (Graversen et al., 2014), increased greenhouse effect of water vapor, and clouds (Taylor et al., 2013; Yoshimori et al., 2017). A number of studies emphasize that the feedback mechanisms are interrelated in a complex way and their relative importance is still unclear (Vihma et al., 2014; Yoshimori et al., 2017; Wendisch et al., 2017; Block et al., 2019).

The analysis of contemporary climate models shows that on average the mean cloud feedback is one of the major mechanisms opposing the Arctic amplification from a top of atmosphere (TOA) perspective with relatively small contribution to the warming at the surface (Pithan and Mauritsen, 2014). Modeling of the cloud impact on the Arctic amplification is still uncertain (Hwang et al., 2011; Taylor et al., 2013; Pithan and Mauritsen, 2014) due to a large number of microphysical processes (Morrison et al., 2012) and complex relations between clouds and other feedback mechanisms of the Arctic climate (Hwang et al., 2011; Graversen and Burtu, 2016). As a result some models underestimate amount of super-cooled liquid water (Sandvik et al., 2007; Cesana et al., 2012; Komurcu et al., 2014; Cesana et al., 2015; Nomokonova et al., 2019b), which may lead to a bias in the surface temperature ranging from -7.8 to $0°C$ (Kay et al., 2016; Miller et al., 2017).

Beyond the energy budget clouds are crucial for precipitation formation that significantly affects the Arctic climate. Precipitated water forms rivers and sustains a glacier flow into the sea, and thus influences the salinity of the Arctic ocean. Being essential for snowmelt (Zhang et al., 1996), sea-ice reduction (Kay et al., 2008; Kay

and Gettelman, 2009) and affecting the permafrost stability, Arctic clouds have a significant impact on productivity and variety in marine and terrestrial environments and thus influence the Arctic ecosystem (Vihma et al., 2016).

Formation of Arctic clouds is a complicated process associated with aerosol-cloud interactions, turbulence, phase transitions, heat and moisture exchanges between the surface and the atmosphere (Morrison et al., 2012). The interaction of clouds with radiation and aerosols remains the largest uncertainties in radiative forcing models (Walsh et al., 2009; Myhre et al., 2013). Many of the processes are not well resolved in global climate models (Klein et al., 2009; Vihma et al., 2016) indicating that parameterization of cloud properties still needs improvements (Morrison et al., 2008; Shupe et al., 2011).

Better understanding of Arctic cloud processes and feedbacks requires long-term and accurate observations (Blanchard et al., 2014; Devasthale et al., 2016). In particular, the knowledge of the vertical cloud structure and phase is crucial for an estimation of the cloud radiative impact (Curry et al., 1996; Shupe and Intrieri, 2004; Liu et al., 2012; Turner et al., 2018). In order to retrieve information on the vertical distribution of clouds and their properties, active remote sensing instruments such as lidars and cloud radars have to be exploited (Protat et al., 2006). However, there are only a few Arctic sites that provide long-term continuous information about the vertical cloud structure using the combination of ground-based remote sensing measurements. These sites are illustrated in Fig. 1.1. Until recently, there were only 4 sites equipped with a variety of instruments including but not limited to a lidar, a cloud radar, a microwave radiometer, and surface radiation and thermodynamic measurement tools, namely Barrow (Alaska; de Boer et al., 2009; Verlinde et al., 2016), Oliktok (Alaska; de Boer et al., 2019), Eureka (Canada; de Boer et al., 2009), and Summit (Greenland; Shupe et al., 2013).

In January 2016 the German Research Foundation started the Transregional Collaborative Research Center (TRR 172) called "Arctic Amplification: Climate Relevant Atmospheric and Surface Processes, and Feedback Mechanisms (AC)^3" (Wendisch et al., 2017). The aim of the (AC)^3 project is to better understand relations between all the components of the Arctic climate. Within this project space-borne, air-borne, ship-borne, and ground-based observations are analyzed to improve representation of local-to-global scale processes influencing the Arctic climate in models.

As a part of this project, comprehensive observations of the atmospheric column have been performed at the French-German Arctic Research Base AWIPEV station, operated by the Alfred Wegener Institute Helmholtz Centre for Polar and Marine Research (AWI) and the French Polar Institute Paul Emile Victor (PEV), at Ny-Ålesund. Within the (AC)^3 project the instrumentation of the AWIPEV station, was complemented with a cloud radar in 2016 and, thus, allows for state-of-the-art vertically resolved cloud observations.

Ny-Ålesund (78.92°N, 11.92°E) is situated at the coastline of Spitsbergen of the Svalbard archipelago. The Svalbard region is located in the area with the highest warming temperature trend in the Arctic (Susskind et al., 2019). In addition, the Svalbard region is often influenced by distinct synoptic regimes bringing either warm moist air from lower latitudes or cold and dry air circulating in the Arctic area (Dahlke and Maturilli, 2017; Mewes and Jacobi, 2019).
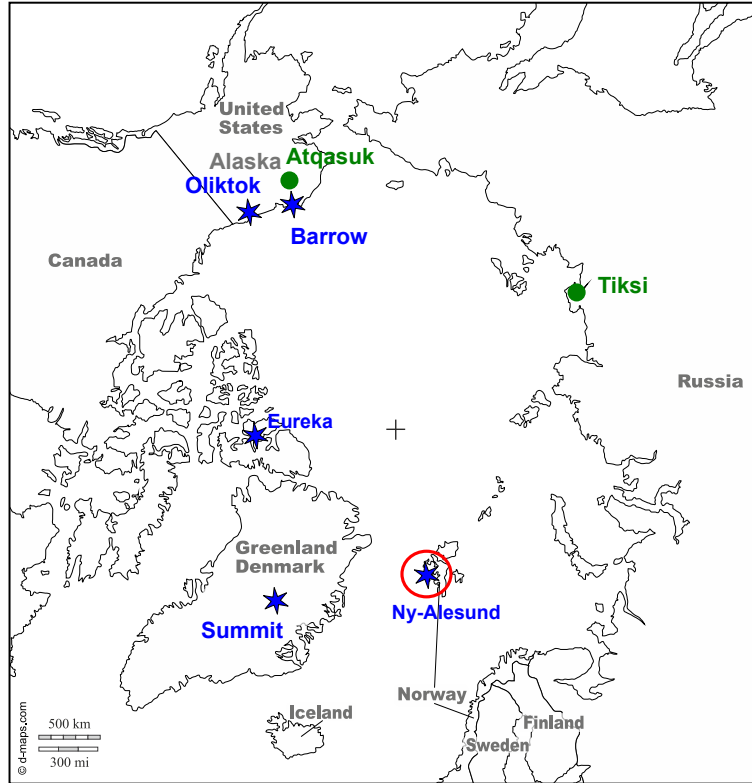
Figure 1.1: Ground-based Arctic observatories with long-term range re-solved cloud observations. The original map was taken from https://d-maps.com/m/world/arctique/arctique10.pdf. Green circle marks and blue stars show sites with ceilometer and radar-ceilometer observations, respectively. The red circle indicates the measurement site analyzed in this thesis.

This thesis is devoted to a characterization of an impact of thermodynamic conditions at Ny-Ålesund on cloud microphysical and radiative properties. The investigation is based on state-of-the-art active, passive, and in situ instruments, a numerical weather prediction model and radiative transfer calculations routinely performed within the $(AC)^3$ project for Ny-Ålesund.

1.1   Role of clouds in the radiation budget

The Earth climate is a complex system defined by the energy exchange between space and five climate components, namely atmosphere, hydrosphere, cryosphere, lithosphere, and biosphere (Trenberth and Stepaniak, 2004). The major part of this energy is received from the Sun in the form of electromagnetic waves. On average the Solar irradiance S_0 is 1361 W m^{-2} (Ohmura, 2012). The solar radiation consists predominantly of shortwave (SW) radiation, which includes near-infrared and visible wavelengths from 0.4–4 μm. On the way to the Earth's surface the solar radiation is partly attenuated by atmospheric components, such as gases, clouds, and aerosols. SW radiation reaching the surface ($F_{\downarrow SW}$) is partly absorbed by the surface, while another part is reflected up ($F_{\uparrow SW}$).

The Earth's surface emits longwave (LW) radiation ($F_{\uparrow LW}$) at wavelengths ranging

from 4 to 100 μm. The atmospheric components also emit LW radiation. The LW radiation can either reach the top of the atmosphere and escape to the space or be absorbed by atmospheric components and the surface. The down-welling LW radiation reaching the surface is further denoted as $F_{\downarrow LW}$.

The differences between incoming and outgoing radiation at the surface Q, also known as the surface net radiation budget, indicate how much radiative energy is absorbed by the surface:

$$Q = \underbrace{F_{\downarrow SW} - F_{\uparrow SW}}_{Q_{SW}} + \underbrace{F_{\downarrow LW} - F_{\uparrow LW}}_{Q_{LW}}. \tag{1.1}$$

In the case when $Q < 0$, more energy leaves the surface and, thus, the surface is radiatively cooled. When $Q > 0$ the surface is getting warmed by the radiation.

The effect of clouds on the radiation budget is characterized by the so-called cloud radiative effect (CRE). In general, CRE at the surface and at the top of atmosphere are often analyzed. Nevertheless, in this thesis the main focus is on the surface radiation budget because the Arctic warming is more pronounced at the surface (Serreze et al., 2009; Boeke and Taylor, 2018). In addition, Wild and Liepert (2010) showed that the surface radiation budget is a key determinant of the intensity of the hydrological cycle and may influence see and land ice coverage (van den Broeke et al., 2009). Therefore, hereafter only CRE at the surface is considered. The longwave (LW), shortwave (SW) and net CRE are defined as differences between corresponding all-sky and cloud-free radiation budgets according to (Ramanathan et al., 1989):

$$\mathrm{CRE}_{SW} = Q_{SW} - \underbrace{(F_{\downarrow \mathrm{clr,SW}} - F_{\uparrow \mathrm{clr,SW}})}_{Q_{SW\,clr}}, \tag{1.2}$$

$$\mathrm{CRE}_{LW} = Q_{LW} - \underbrace{(F_{\downarrow \mathrm{clr,LW}} - F_{\uparrow \mathrm{clr,LW}})}_{Q_{LW\,clr}}, \tag{1.3}$$

$$\mathrm{CRE} = \mathrm{CRE}_{SW} + \mathrm{CRE}_{LW}, \tag{1.4}$$

where $F_{\downarrow \mathrm{clr,SW}}$, $F_{\downarrow \mathrm{clr,SW}}$, $F_{\uparrow \mathrm{clr,LW}}$ and $F_{\uparrow \mathrm{clr,LW}}$ are surface down- and upwelling fluxes for SW and LW, respectively, which would be if the sky were cloud free.

Based on space-borne observations Matus and L'Ecuyer (2017) estimated SW, LW, and net CRE over the globe (Fig. 1.2). The authors showed that on average clouds produce surface radiative cooling of 24.9 W m^{-2}. The strongest cooling was found to occur in the Tropical area. In contrast, the strongest surface radiative warming by clouds is about 20 W m^{-2} in the polar regions.
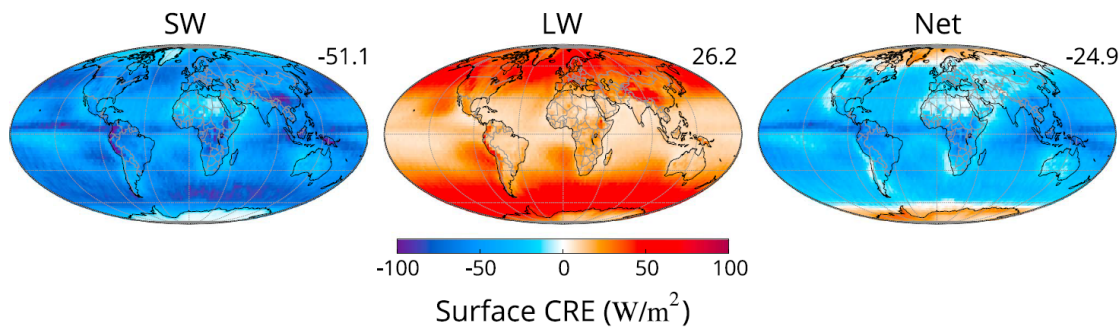
Figure 1.2: Annual average SW, LW, and net CRE at the surface. Figure adapted from (Matus and L'Ecuyer, 2017). The numbers indicate global averages of the corresponding CRE.

1.2 Role of clouds in the Arctic warming

The important role of clouds for the global climate was shown in many studies (Taylor et al., 2013; Matus and L'Ecuyer, 2017). First, clouds are the second largest contributor to the surface warming in polar regions in response to the anthropogenic CO_2 forcing. The surface warming due to green-house gases changes cloud properties and consequently their radiative effect. The exact response of clouds to the surface warming is not yet clear (Ceppi et al., 2017). Vavrus (2004) noticed that changes in clouds caused by CO_2 forcing may be associated with one third of the surface global warming signal at all latitudes, with up to 40 % in the Arctic region. The cloud-induced temperature response is associated with the enhanced downwelling LW flux at the surface due to the increased presence of low-level liquid-containing clouds. Second, most of the contemporary climate models show that from the top-of-the-atmosphere perspective clouds enhance warming in the Tropical region with a lesser impact in the Arctic region. This indicates, that clouds could be one of the atmospheric components opposing the Arctic amplification at TOA (Taylor et al., 2013; Pithan and Mauritsen, 2014; Block et al., 2019). Third, clouds tend to reduce the temperature gradient between the poles and equator at the surface, while they increase the gradient in the upper troposphere (Taylor et al., 2013).

The role of clouds in the global climate is inextricably linked to other components of the climate and the water cycle. A change in one component often leads to a response in many other components, which, in turn, have a feedback effect on the initially changed component. The feedback effects are especially crucial for the Arctic region having the complex environment characterized by a high seasonal variability of the sea/land ice coverage, frequent temperature inversions, drier air and lower temperatures with respect to the Tropics and mid-latitudes, transitions between polar night and polar day. For instance, the high surface albedo due to ice coverage leads to relatively low SW CRE (Miller et al., 2015), since the clouds and snow-covered surface have similar albedo (Cox et al., 2016). In the longwave, the surface downwelling flux depends on the atmospheric temperature (Cox et al., 2015) and, therefore, in the case of temperature inversions low-level clouds can emit at warmer temperatures than the surface (de Boer et al., 2011).
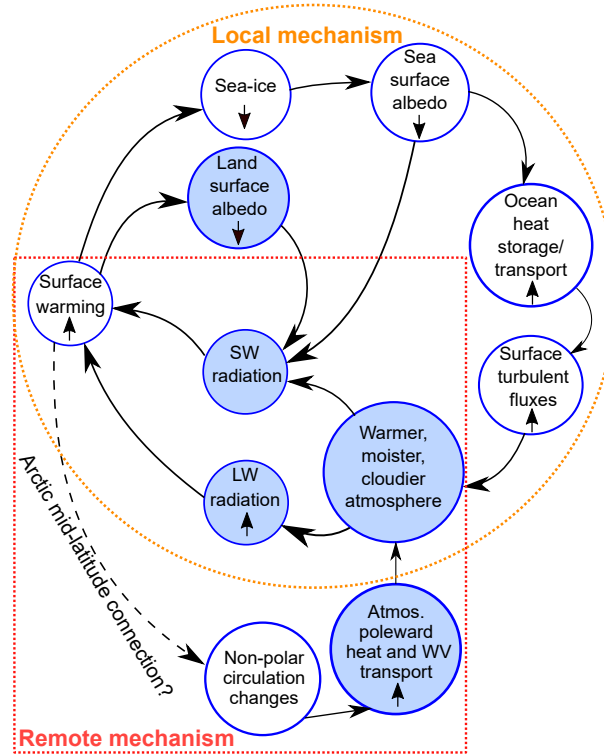
Figure 1.3: The schematic diagram of feedback processes induced by the surface warming in the Arctic. Figure adapted from (Boeke and Taylor, 2018). Remote feedback mechanisms are shown within the boarders of a red rectangular box, local feedback mechanisms are inside the orange circle.

Boeke and Taylor (2018) illustrated the feedback mechanisms related to the surface warming in the Arctic region (Fig. 1.3). The authors distinguish two major feedback mechanisms: local and remote. The local mechanism includes processes evolving in the Arctic region while the remote mechanism is related to an atmospheric poleward heat and water vapor transport into the Arctic from the mid-latitude region.

Boeke and Taylor (2018) consider the local mechanism as a combination of non-radiative and radiative mechanisms. In the non-radiative mechanism an increase in the surface temperature is associated with lower sea ice coverage, which leads to more open water that in turn enhances amount of energy collected by the ocean during the extended ice-free season (Serreze et al., 2009; Kapsch et al., 2013). Longer periods of open ocean are related to a warmer, moister, and cloudier atmosphere (Rinke et al., 2013; Palm et al., 2010; Kay and Gettelman, 2009; Mioche et al., 2015; Bennartz et al., 2013). More clouds and water vapor in the atmosphere lead to a stronger green-house effect, which further increases the surface temperature. On the other hand, the same atmospheric changes lead to less SW radiation reaching the surface. Another mechanism affects the surface temperature by the decrease in the surface albedo caused by the sea/land ice retreat. In the case of the decreased surface albedo, the surface absorbs more SW solar radiation, which leads to the surface temperature increase. Hence, the effects of the described mechanisms on the surface temperature due to the SW radiation oppose each other. The surface warming induces the positive albedo feedback, which is partly counteracted by the sun-shading effect by clouds in summer.

The Arctic climate is significantly affected by air masses transported from the mid-latitudes (Graversen and Burtu, 2016; Hwang et al., 2011). A number of studies have already related the air transport and atmospheric rivers to amount of water vapor, cloud properties, and the radiation budget (Hwang et al., 2011; Boisvert et al., 2016; Mortin et al., 2016; Sedlar and Tjernström, 2017; Hegyi and Taylor, 2018). Hegyi and Taylor (2018) reported that the episodes of poleward atmospheric water vapor transport are associated with periods of increased water vapor and cloud cover resulting in enhanced downwelling longwave surface fluxes and reduced surface cooling efficiency. Raddatz et al. (2013) analyzed the impact of cloud coverage and increased water vapor on the longwave downwelling radiation using ground-based observations installed at different sites in the Beaufort Sea–Amundsen Gulf region of the Canadian Arctic. The authors found that the cloud coverage and water vapor explain 84% of the variance of the longwave downwelling radiation, while the remaining 16% are associated with cloud composition, cloud thickness and cloud-base height. Raddatz et al. (2013) estimated differences in the longwave downwelling radiation between cases with typical and maximum values of water vapor. The authors associate the latter to moist intrusion events. The differences are 82 and 95 W m^{-2} in winter and 38 W m^{-2} and 45 W m^{-2} in summer for clear sky and cloudy conditions, respectively. A limited number of studies show that air transportation patterns may influence phase partitioning and amount of liquid in Arctic clouds (Qiu et al., 2018; Tjernström et al., 2019).

A number of recent studies shows an evidence that warmer Arctic temperatures may potentially change non-polar circulation and affect the weather at mid-latitudes (Cohen et al., 2014; Walsh, 2014; Francis and Vavrus, 2015; Boeke and Taylor, 2018; Coumou et al., 2018). However, it is often mentioned that currently there is no consensus on how strong the influence of the Arctic warming on the mid-latitude circulation is.

As depicted in Fig. 1.3, local and remote mechanisms defined by the energy exchange and the moisture transport, may have a strong impact on the Arctic cloud properties (Cesana et al., 2012; Morrison et al., 2012). It still remains difficult to fully understand the complexity of interactions between different components of the Arctic climate and to assert how they influence the cloud evolution (Vihma et al., 2014). Within the Coupled Model Intercomparison Project Phase 5 (CMIP5) Boeke and Taylor (2016) analyzed 17 climate models and found a larger inter-model spread in the surface radiation budget in the Arctic region. The authors noticed a large divergence in the modeled cloud occurence and CRE among the analyzed models. Differences in cloud occurrence and net surface CRE reached 60% and 40 W m^{-2}, respectively.

1.3 Studies on feedback processes in the Svalbard region

Ørbæk et al. (1999) showed the uniqueness of the radiation regime in Svalbard. In summer and autumn the radiation budget in the western and southern parts of Svalbard are influenced by the open-ocean climate characterized by the sea fog and the low albedo. In contrast, in winter and spring the radiation regime becomes

more continental similar to the central Svalbard area (Gjelten et al., 2016). Complex terrain in Svalbard leads to local variations in the surface radiation budget. These variations become especially pronounced during the melting and freezing periods. The radiation regime at Ny-Ålesund represents neither the oceanic nor continental types of the Arctic radiation pattern, but rather their combination (Ørbæk et al., 1999): ocean-like radiation climate in summer and autumn, and continental in the winter and spring.

Ohmura (2012) analyzed almost 20 years of surface radiation observations at Ny-Ålesund and found an increase in downwelling LW radiation and surface temperature of 4.9 W m^{-2} decade^{-1} and 1.18 °C decade^{-1}, respectively. The author stated that the increase in the downwelling LW radiation expected from a sheer temperature increase is 3.4 W m^{-2} decade^{-1}, while the remaining change should be attributed to changes in the atmospheric components such as greenhouse gases, water vapor feedback, and cloud properties.

Maturilli and Kayser (2016) showed a highly pronounced warming and moistening of the tropospheric column in the Svalbard region. Analyzing a 22-year dataset (1993-2014) from radiosondes the authors found that during winter time there has been a significant increase of atmospheric temperature (up to 3 K per decade) and mean integrated water vapor (+0.83±1.22 kg m^{-2} per decade). This tendency in winter is correlated with a strong increase in up- and downward longwave radiation of +11.6±10.9 W m^{-2} and 15.6±11.6 W m^{-2}, respectively (Maturilli et al., 2015).

Dahlke and Maturilli (2017) found a relation between the observed trend in warming and moistening in the winter season in the Svalbard region and the increasing air mass transport through the North Atlantic pathway and reduced flow from the north. Nevertheless, the authors emphasized a lack of understanding of how the circulation shift is connected to other feedback mechanisms including ocean heat transport, sea ice dynamics, and cloud and water vapor radiative effects.

Isaksen et al. (2016) analyzed relationships between the surface air temperature at 5 stations at Spitsbergen and the sea ice concentration. The authors found that the sea ice concentration outside the stations has been reduced on average from 58 to 6% during the period 1997–2015. According to Isaksen et al. (2016), these changes in the sea ice concentration may be important for the local climate. For instance, when the fjord is open, energy is transfered from water to the air and, therefore, convection develops. This transfer is blocked in the case of an ice-covered fjord. In this case, surface inversions can occur (Isaksen et al., 2016). On the regional scale the climate in Svalbard is sensitive to the location of the regional ice edge (Benestad et al., 2002; Isaksen et al., 2016). Isaksen et al. (2016) found a high correlation between the surface air temperature and the sea ice concentration for air masses coming from East and North of Spitsbergen, which indicates an importance of the heat exchange between open water in the Barents Sea and the atmosphere for the atmospheric warming in Spitsbergen. Tetzlaff et al. (2014) analyzed an effect of polynya on the surface temperature in Svalbard. The authors noticed that a larger extent of polynya is related to higher surface temperatures and may increase the potential temperature. The authors argue that polynya extent can lead to strong boundary layer convection, which, in turn, can influence cloud occurrence and precipitation intensity. A number of studies are focused on the energy interactions between the ocean, land, and the atmosphere in the area of Svalbard (Weill et al., 2012; Meyer et al., 2017; Peterson

et al., 2017). Nevertheless, such studies are mostly focused on non-radiative energy transfer effects. Persson et al. (2017) recently showed an analysis of a complete surface energy budget based on the multi year data set from the SHEBA (Surface Heat Budget of the Arctic Ocean) campaign. Such an analysis for Ny-Ålesund requires information on cloud radiative properties, which, until recently, were not available.

The climate at Ny-Ålesund exhibits not only the trends in temperature and humidity but also changes in occurrence of extreme events. For instance, Wei et al. (2016) found significant negative (positive) changes in occurrence of cold (warm) extremes over the last 3 decades. In addition, the authors report that the temperatures of the coldest events increase by 2.3 °C decade^{-1}, while temperatures of the hottest events did not change much. The number of extreme events has also changed (Wei et al., 2016). Cold spells are becoming less frequent ($\sim$–3% decade^{-1}), whereas the occurrence of warm spells increased by $\sim$ 1.5% decade^{-1}. Wei et al. (2016) mentioned that the changes in temperatures can be associated with the sea surface temperature and large-scale atmospheric circulation patterns. Yamanouchi (2018) showed a case study with a contrast in cloud conditions and longwave radiation during a transition from cold to warm periods. The authors concluded that the cold periods are associated with low occurrence of clouds and relatively thin clouds, while high cloudiness and thick clouds are typical for periods of warm and moist intrusions. Since the author investigated only a short period, an analysis of longer cloud observations is still needed. Yeo et al. (2018) investigated how the advection of warm and cold air masses affects cloudiness, longwave fluxes at the surface and near-surface temperature at Ny-Ålesund during winter. The authors analyzed a 10-day period in February with alternating warm and cold conditions related to distinct circulation patterns. During cold periods Yeo et al. (2018) observed a reduced cloudiness and down-welling longwave flux of 200-230 W m^{-2}. In contrast, warm periods were associated with cloud occurrence close to 100 % and enhanced down-welling longwave flux of 300 W m^{-2}. For this study the authors used a ceilometer and surface radiation measurements and, thus, could not analyze how warm and cold air masses affect microphysical properties of clouds and their radiative effect.

1.4 Coupling of cloud and environmental properties to SW and LW CRE

One of the most important cloud characteristics affecting the radiative properties of clouds is their phase composition (Shupe and Intrieri, 2004; Sun and Shine, 1994; Yoshida and Asano, 2005; Komurcu et al., 2014). Typically, according to the phase composition clouds are classified into three categories: liquid, ice, and mixed-phase. The first two categories consist purely of liquid and ice particles, respectively. A mixed-phase cloud has liquid and ice phases coexisting within boundaries of the cloud. Long-term in situ observations showed that liquid and ice particles have distinct microphysical properties (Korolev et al., 2003). Liquid droplets have nearly spherical shapes, sizes in the order of 10–20 μm, and the number concentration ranging from 4×10^1 to 2×10^2 cm^{-3}. Ice particles may have a vast variety of shapes from pristine plates and columns to irregular-shaped aggregates and rimed particles

(Bailey and Hallett, 2009; Kneifel et al., 2015). Size of cloud ice also varies in a wide range from 20 μm to a few cm. The number concentration of ice particles observed in the atmosphere ranges from 10^{-8} to 1 cm^{-3} (Kanji et al., 2017), which is several order of magnitudes lower than for liquid droplets.

Particles in a cloud have a variety of sizes, which is characterized by a particle size distribution (PSD) $N(D)$, where D is the particle's size. Typically, a PSD is parameterized by an analytical function, such as generalized Gamma distribution or log-normal distribution, which depend on few parameters. PSD is used to calculate bulk physical properties of cloud particles, e.g. effective radius r_{eff}, and liquid and ice water contents (LWC and IWC):

$$r_{\text{eff}} = \frac{\int_0^\infty r^3 N(D)dD}{\int_0^\infty r^2 N(D)dD}, \tag{1.5}$$

$$\text{IWC} = \rho_i \int_0^\infty V(D)N_i(D)dD, \tag{1.6}$$

$$\text{LWC} = \rho_l \int_0^\infty V(D)N_l(D)dD, \tag{1.7}$$

where ρ is the density, r is the radius of a sphere with equal surface area, V is the volume of water in a particle, indexes i and l stand for ice and liquid water, respectively.

A total amount of condensed water in a cloud layer (also known as cloud water path, CWP) can be obtained by integration of vertical profiles of IWC and LWC within the cloud boundaries. For a single mixed-phase cloud layer shown in Fig. 1.4 CWP is defined as follows:

$$\text{CWP} = \int_{h_{i1}}^{h_{i2}} \text{IWC}(h)dh + \int_{h_{l1}}^{h_{l2}} \text{LWC}(h)dh. \tag{1.8}$$

In Eq. 1.8 h denotes an altitude with indexes i and l indicating ice and liquid containing parts of a cloud, and indexes 1 and 2 denote the lower and upper boundaries of a corresponding part of the cloud.

The phase partitioning of a cloud is characterized by liquid water fraction (LWF), which is the ratio of total mass of water in the cloud over CWP:

$$\text{LWF} = \frac{\int_{h_{l1}}^{h_{l2}} \text{LWC}(h)dh}{\text{CWP}}. \tag{1.9}$$

In general, an atmospheric profile can have more than one cloud layer. Therefore, often total amounts of ice and liquid water in a vertical profile are characterized by liquid and ice water path (LWP and IWP), respectively:

$$\text{LWP} = \int_0^\infty \text{LWC}(h)dh, \tag{1.10}$$

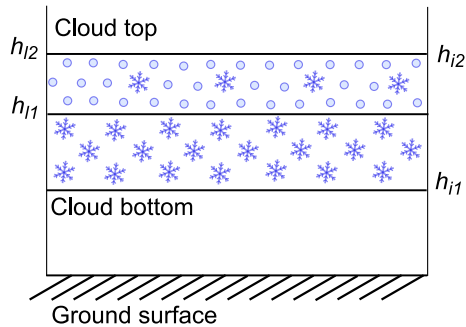$$\text{IWP} = \int_0^\infty \text{IWC}(h)dh. \tag{1.11}$$

Figure 1.4: Schematic diagram of a typical thin single-layer mixed-phase cloud containing a liquid layer close to the cloud top and ice virga below.

Shupe and Intrieri (2004) estimated how different cloud and environment properties influence CRE. The authors considered the atmosphere divided into three layers: the above-cloud atmosphere, the cloud layer, and the below-cloud atmosphere. In this section these layers are denoted by indexes a, c, and bl, respectively. The cloud fraction was assumed to be 1. With this model the authors obtained the following first-order approximation of SW CRE:

$$\text{CRE}_{SW} \approx \underbrace{t_{bs}S_0\cos(\text{z})(1-\alpha_s)t_{cs}}_{\text{cloudy sky}} - \underbrace{t_{bs}S_0\cos(\text{z})(1-\alpha_s)}_{\text{clear sky}} = S_0\cos(\text{z})t_{bs}(1-\alpha_s)(t_{cs}-1),$$

(1.12)

where z is the solar zenith angle, α_s is the broadband surface albedo, t_{bs} and t_{cs} are broadband SW atmospheric and cloud transmittances, respectively. The transmittances t_{bs} and t_{cs} in Eq. 1.12 include direct and diffuse components. The direct component is a fraction of the incident radiation passing through the atmosphere without being scattered or absorbed. The diffuse component is a part of the incident radiation that is scattered at least once before reaching the surface (in the case of t_{bs}) or cloud bottom (in the case of t_{cs}). t_{bs} is defined by properties of atmospheric gases and aerosols, while t_{cs} is defined by cloud macro and microphysical properties.

The differences between cloud liquid and ice discussed in Sec. 1.4 result in a diversity in CRE between liquid, ice, and mixed-phase clouds. Yoshida and Asano (2005) analyzed how LWF influences the radiative properties of clouds in visible and near-infrared parts of the radiation spectrum. The authors showed that for a constant optical cloud thickness LWF does not have a strong effect at visible wavelengths. At near-infrared wavelengths the influence of LWF is more pronounced. A decrease/increase in LWF lead to lower/higher reflectance and higher/lower absorptance. Therefore, the total SW transmittance t_{cs} becomes larger at higher LWF. According to Eq. 1.12 this leads to more negative CRE_{SW} produced by ice clouds with respect to liquid clouds with the same optical thickness. Nevertheless, many liquid particles often have larger surface area per unit volume than relatively few ice particles and, therefore, liquid clouds tend to have higher optical thickness and, consequently, lower transmittance than ice clouds (Shupe and Intrieri, 2004).

Sun and Shine (1994) reported that radiative properties of clouds also depend on how liquid and ice phases are mixed within the cloud boundaries. The simulations performed by the authors showed that the uniform mixing assumption of liquid and

ice within a cloud may lead to about 20% overestimation of the cloud single scattering albedo in comparison to cloud with layered and columnar phase arrangement.

The importance of the vertical profiles of liquid and ice for radiative properties of clouds was also shown by Yoshida and Asano (2005). The authors analyzed the sensitivity of cloud SW radiative properties to a change of liquid layer position inside a mixed-phase cloud with fixed liquid and ice water paths. At visible wavelengths there was no dependence on the position. But reflectance and absorptance of mixed-phase cloud at near-infrared wavelengths are strongly depended on the vertical profile of the phase.

Equation 1.12 shows that beside the cloud microphysical properties, CRE_{SW} also depends on the surface albedo and SZA. Typically, CRE_{SW} becomes more negative with decreasing α_s, since there is more contrast between less reflecting surface and highly-reflecting clouds. Based on measurements from the Arctic Summer Cloud Ocean Study (ASCOS) Sedlar et al. (2011) found that the decrease in α_s by 0.01 leads to an increase in the CRE_{SW} magnitude by ± 1.8 W m^{-2}. Shupe and Intrieri (2004) showed that for typical late-spring Arctic conditions the decrease in α_s by 0.1 changes CRE_{SW} to more negative values by about 40 W m^{-2}. SZA, which is the angle between the zenith and the sun, affects the solar flux reaching the top of the atmosphere. Therefore, when the sun is high in the sky (low SZA), the shading effect of the clouds becomes stronger (Shupe and Intrieri, 2004), i.e. CRE_{SW} becomes more negative.

According to Shupe and Intrieri (2004), LW CRE can be approximated as:

$$
\begin{aligned}
\mathrm{CRE}_{LW} \approx & \underbrace{t_{bl}(1-\epsilon_{cl})\sigma T_a{}^4 + t_{bl}\epsilon_{cl}\sigma T_c^4 + \sigma T_{bl}{}^4 - \epsilon_s\sigma T_s{}^4}_{\text{cloudy sky}} \\
& - \left(\underbrace{t_{bl}\sigma T_a{}^4 + \sigma T_{bl}{}^4 - \epsilon_s\sigma T_s{}^4}_{\text{clear sky}} \right) \\
= & \ t_{bl}\epsilon_{cl}\sigma(T_c{}^4 - T_a{}^4),
\end{aligned}
\tag{1.13}
$$

where t_{bl} is the broadband LW transmittance of the below-cloud atmosphere; T_a and T_c are effective temperatures of the above-cloud atmosphere and the cloud, respectively; σ is the Stefan–Boltzmann constant, ϵ_{cl} and ϵ_s are the broadband emissivities of cloud and surface, respectively.

Equation 1.13 shows that one of the key parameters defining radiative properties of a cloud in the infrared is the cloud emissivity ϵ_{cl}. Smith et al. (1993) showed that the contribution of the cloud emissivity to the downwelling LW radiation is an order of magnitude larger than the contribution from the cloud reflectance, and, therefore, ϵ_{cl} can be related to the cloud LW transmittance t_{cl}, which is proportional to CWP (Iacono et al., 2000):

$$
\epsilon_{cl} \approx 1 - t_{cl} = 1 - e^{-\beta_{diff}\kappa_{abs}\mathrm{CWP}},
\tag{1.14}
$$

where β_{diff} is the diffusivity factor typically assumed to be 1.66 (Ebert and Curry, 1992; Garrett et al., 2002) and κ_{abs} is the combined liquid and ice phase LW cloud absorption coefficient.

The cloud absorption coefficient κ_{abs} is a sum of the liquid water κ_l and ice absorption κ_i coefficients weighted by the fraction of liquid and ice phase, respectively:

$$\kappa_{abs} = \kappa_l \text{LWF} + \kappa_i(1 - \text{LWF}), \tag{1.15}$$

According to Garrett et al. (2002) κ_l does not depend on microphysical properties of droplets when their sizes are mostly below 10 μm. For larger droplets κ_l is inversely proportional to the effective radius r_{eff}. The mass absorption coefficient for ice κ_i can be defined as follows (Ebert and Curry, 1992):

$$\kappa_i = \frac{\sigma_i}{\text{IWC}}, \tag{1.16}$$

σ_i here is the volume absorption coefficient (Ebert and Curry, 1992):

$$\sigma_i = \int_0^\infty \frac{A(D)}{4} Q_i(D) N_i(D) dD, \tag{1.17}$$

where A is the surface area of an ice particle, Q_i is the absorption efficiency of an ice particle.

Shupe and Intrieri (2004) showed that values of LW CRE range from 0 to 85 W m^{-2} and depend on the amount of liquid in a column, which is characterized by LWP. The upper limit of CRE$_{LW}$ corresponds to clouds with LWP exceeding, depending on a site, 30–50 g m^{-2} (Stephens, 1978; Shupe and Intrieri, 2004; Miller et al., 2015; Ebell et al., 2020). Liquid-containing clouds with LWP exceeding the threshold act as a black body, i.e. $\epsilon_{cl} = 1$, and a further increase of LWP does not change their LW radiative properties.

Since the amount of liquid water is typically related to the atmospheric temperature, Sedlar et al. (2011) investigated how LW CRE is related to the cloud top temperature. The authors reported that for cloud base temperatures below –10 °C the observed LWP is primarily below 25 g m^{-2} and CRE$_{LW}$ ranges from 10–30 W m^{-2}. For the temperatures above –10 °C LWP mostly exceeds 25 g m^{-2} and CRE$_{LW}$ varies from 50 to 85 W m^{-2}.

Ebell et al. (2020) found that the limit in CRE$_{LW}$ can be caused by clouds with IWP exceeding 150 g m^{-2} based on observations at Ny-Ålesund. This is consistent with Feofilov et al. (2015), who showed that the ice cloud emissivity does not strongly depend on IWP for clouds with IWP $> 100 - 150$ g m^{-2}.

1.5 Estimation of CRE from observations

According to Eqs. 1.2 and 1.3 an estimation of CRE requires a knowledge on all-sky SW and LW fluxes (Q_{SW} and Q_{LW}) and those if the sky were cloud-free (Q_{SWclr} and Q_{LWclr}). All sky fluxes can be continuously measured by radiation sensors. In contrast, Q_{SWclr} and Q_{LWclr} cannot be directly measured under cloudy conditions and have to be estimated. Several approaches exist to define the clear sky fluxes.

One approach is to substitute Q_{SWclr} and Q_{LWclr} by the net SW and LW fluxes approximated from radiation measurements during clear sky conditions. Long and

Ackerman (2000) developed a technique to identify clear sky scenes based on surface-based observations of total and diffuse SW fluxes. The authors used the identified cases to fit the clear sky flux functions using linear regressions. Regression coefficients are estimated for each day with more than 120 one-minute clear sky samples. A span in the solar zenith angle should be at least 0.4 around the maximum local Sun position. For cloudy days the regression coefficients are linearly interpolated.

Long and Turner (2008) proposed a method for continuous estimation of clear sky downwelling LW. The authors identify clear sky cases based on the observed surface downwelling LW flux, air temperature, and relative humidity. $F_{\downarrow clr,LW}$ is parameterized as follows:

$$F_{\downarrow LWclr} \approx C(e_w/T_{amb})^{1/7}\sigma T_{amb}^4, \tag{1.18}$$

where T_{amb} is the ambient air temperature, e_w is the water vapor pressure, and C is the effective temperature/humidity lapse rate coefficient. The coefficient C is calculated as:

$$C = k + a(RH)^b, \tag{1.19}$$

where coefficients k, a, and b are empirically determined from the identified clear cases.

The methods based on the interpolation of clear sky fluxes to cloudy scenes are straightforward and easy to implement. Since these methods use empirically derived coefficients the results partly include long-term variability in atmospheric gases and aerosols, which have an impact on the atmospheric radiative properties. On the other hand, intra day variability in atmospheric components may introduce additional uncertainties in the coefficient estimations. Furthermore, the methods use only surface observations and are subjects to uncertainties related to variability in vertical profiles of, for instance, water vapor. A major disadvantage of the described methods is the requirement for a sufficient number of clear sky samples, and, for SW, a proper range of zenith angles. For the Arctic region with a high cloud occurrence and polar nights these requirements are often not satisfied.

Another approach of the CRE estimation is based on broadband radiative transfer calculations. Such a method directly accounts for cloud properties as well as influence of any other atmospheric component included in the model. One of the widely used models for the calculation of atmospheric radiative properties is the rapid radiative transfer model (RRTMG, Mlawer et al., 1997; Barker et al., 2003). This model requires information on aerosols, surface albedo, temperature and humidity profiles, and cloud microphysics. The model outputs vertical profiles of SW and LW fluxes. In order to estimate the contribution by clouds, the model is run twice with and without clouds for the same other inputs. RRTMG determines the radiative properties of clouds under the plane-parallel assumption, i.e. atmospheric parameters are assumed to be homogeneous in horizontal dimensions and vary only in the vertical direction. RRTMG does not take into account three-dimensional radiative effects due to inhomogeneities of surface and broken clouds, multi-scattering effects and atmospheric polarization.

1.6 Observations of cloud properties in the Arctic

For an accurate estimation of CRE with a radiative transfer model, profiles of atmospheric components are required. Typically, retrieved profiles from ground-based or/and space-borne measurements are used. Satellites with passive and active instrumentation on-board provide estimation of cloud and aerosol properties, and radiative fluxes in a large-scale perspective (Cesana et al., 2012; Kay et al., 2016; Sedlar and Tjernström, 2017; Wild et al., 2019).

A number of cloud studies is based on passive observations from the MODerate-resolution Imaging Spectroradiometer (MODIS). Two instruments of this type are carried by the Terra and Aqua satellites launched in December 1999 and May 2002, respectively. MODIS has 36 spectral bands from 0.41 to 14.2 μm. King et al. (2013) analyzed a decade of MODIS observations and showed that in the Arctic region the average cloud occurrence is about 70%. The authors found 20% more clouds over the Arctic ocean with respect to the land. Based on the algorithm by King et al. (2010), King et al. (2013) analyzed properties of liquid and ice clouds. The authors found a seasonal variability in occurrence of liquid and ice clouds. Over the land liquid clouds were present in 20–30% of profiles during summer months while almost no liquid clouds were detected in winter months. An opposite relation was found for ice clouds with the maximum occurrence of 40% in winter and minimum of 15% in summer. Over the ocean the authors found about a factor of 2 more liquid clouds. The occurrence of ice clouds over the ocean was nearly equivalent in comparison to profiles over the land. Effective sizes of liquid and ice particles were found to be 11–15 and 16–28 μm, respectively.

The detection of clouds over the Arctic region using passive space-born instruments is challenging especially over snow covered surfaces and sea ice due to the low contrast in visible and thermal infrared bands between clouds and underlying surfaces (Liu et al., 2010). For instance, Trepte et al. (2019) analyzed the cloud mask from the Clouds and Earth's Radiant Energy System (CERES), which is based on a cloud detection algorithm from MODIS. The authors compared the CERES cloud mask with the vertical feature mask from active space-borne observations. The results of the comparison reveal an agreement in cloud cover in 90–99% of cases over snow-free areas for day and night conditions. Over snow-covered areas the detection of clouds agrees in 89–94% and 77–84% of cases during day and night time, respectively (Trepte et al., 2019). It was found that a large part of clouds missed in CERES are clouds with relatively low cloud optical depth (less than 1). In addition, the cloud detection by visible and infrared space-borne instruments exhibits large uncertainties during night time conditions due to a low thermal contrast between surface and clouds (Frey et al., 2008; Trepte et al., 2019). Moreover, passive satellite sensors can provide only a limited information on the cloud vertical structure (Zhang et al., 2004) and have difficulties in providing accurate temperature and humidity profiles for the lower atmosphere, which is particularly important for an estimation of the LW downward flux (Wang and Liang, 2009).

Active space-borne instruments can improve the cloud detection and reduce the limitations of satellite-based passive instruments. For instance, the Cloud-Aerosol Lidar with Orthogonal Polarization (CALIOP) and the 94 GHz cloud radar installed on the CALIPSO and CloudSat satellites, respectively, are widely used for cloud in-

vestigations. Measurements from CALIOP and the CloudSat radar are not affected
by the snow-covered surfaces and the lack of the sunlight during the polar night
Mioche et al. (2015). The CloudSat radar can profile almost all non-precipitating
clouds. But the CloudSat radar is often not sensitive to thin cirrus clouds, which
typically contain relatively small particles. CALIOP is more sensitive to optically
thin clouds. Thus, both instruments are typically used in synergy to provide more
reliable detection of clouds. Matus and L'Ecuyer (2017) analyzed the cloud fraction
on the global scale (gridded with the 2.5° x 2.5° spatial resolution) utilizing observa-
tions from CALIOP and the CloudSat radar for the period from 2007 to 2010. The
authors classified cloud profiles to liquid, ice, mixed and multi-layer. The results
showed that in the Arctic region the occurrence of clouds is about 75% with 28, 21,
13, and 13% of ice, multi layer, liquid, and mixed-phase clouds, respectively. The
authors found that at high latitudes, mixed-phase clouds are less common during
winter months as colder temperatures limit the presence of supercooled liquid water.

Mioche et al. (2015) analyzed the total cloud occurrence over the entire Arctic
region and Svalbard region for the period from 2007 to 2010 and compared the
results obtained from different satellite products and ground-based observations.
The authors obtained cloud types and properties using the DARDAR algorithm
(Delanoe and Hogan, 2010), which is based on combined observations from CALIOP
and the CloudSat radar. The results showed that the total cloud occurrence over
the Svalbard region is about 5–10% higher than the average over the entire Arctic.
In winter and spring this difference reaches 20%. Mioche et al. (2015) also reported
that mixed-phase clouds occur in 30% of winter and early spring profiles and 50%
during the other seasons. The authors found 10–15% higher occurrence of mixed-
phase clouds in the Svalbard region.

Cesana et al. (2012) analyzed ice- and liquid-containing clouds in the Arctic region
for the period from 2006 to 2011 using passive and active observations from the
CALIPSO satellite. The authors reported that ice-containing clouds were mostly
observed at altitudes above 4 km and in the temperature range from -30 to -60 °C.
Liquid-containing clouds were mostly found in the lowest 3 km at temperatures from
-25 to 0 °C. The authors found a spacial variability of the cloud fraction in the Arctic
region for different seasons. Liquid-containing clouds have the highest occurrence
of 0.65 in summer over the Barents and Greenland seas. In winter and spring the
fraction of liquid clouds is about 0.2 over the whole Arctic domain but it may exceed
0.5 in regions affected by the Aleutian and Icelandic Lows.

The detection of low-level clouds from the active space-borne observations has lim-
itations (Zygmuntowska et al., 2012; Mioche et al., 2015). The authors compared
the retrieved cloud occurrence from CALIOP and the CloudSat radar with ground-
based observations and found an underestimation in cloud detection by space-borne
instruments of 20% for altitudes between 0.5 and 2 km and 25% below 0.5 km. (Liu
et al., 2017) found 25–40% fewer clouds below 0.5 km from the same space-borne in-
struments in comparison to ground based instruments. Particularly, fewer ice clouds
and mixed-phase clouds were observed from space-borne observations between the
surface and 1 km height compared to ground-based observations. Blanchard et al.
(2014) showed that this limitation is related to the ground clutter contamination
and the strong attenuation of the lidar signal, especially by liquid and mixed-phase
clouds. In addition, availability of satellite observations for a certain location ranges

from a few times per day to once in several weeks (Winker et al., 2009). Thus, continuous observations are often not available. In addition, satellite instruments have relatively large footprints and coarse spacial resolution. Therefore, inhomogeneities in atmospheric and surface properties are averaged out, which makes it difficult to compare the retrievals based on space and ground-based observations.

Ground-based remote-sensing instruments provide continuous profiling of atmosphere with high temporal and spacial resolution. Microwave radiometers allow for temperature and humidity profiling as well as the estimation of total amounts of water vapor and liquid water in a column (Loehnert, 2002; Rose et al., 2005). Active ground-base measurements can be used for the discrimination between liquid, ice, and mixed-phase clouds (Shupe, 2007; Illingworth et al., 2007), estimation of IWC Hogan et al. (2006), LWC Frisch et al. (1998), and size of cloud particles (Donovan and van Lammeren, 2001; Frisch et al., 2002; Delanoe and Hogan, 2008). Thus, observations from a cloud radar, lidar, microwave radiometer are widely used to get detailed macro and microphysical properties of clouds (Shupe et al., 2015), which can be used as an input for a radiative transfer model (Shupe and Intrieri, 2004; Dong et al., 2010; Ebell et al., 2011; Turner et al., 2018). The ground-based observations are particularly valuable for the Arctic region, where a large part of the variability in the surface radiation is defined by low-level liquid-containing clouds (Turner et al., 2007), which, as mentioned above, cannot be reliably detected from space. Ground-based radiation sensors are often collocated with a set of atmospheric profilers and, therefore, provide a continuous dataset that can be used to evaluate the results of the used radiative transfer model (Ebell et al., 2011).

Many studies utilized ground-based remote sensing measurements in order to provide statistics on cloud phase, cloud macrophysical and microphysical properties for several Arctic sites (Intrieri et al., 2002; Shupe et al., 2011; Shupe, 2011). A number of cloud studies involved ship- and air-borne sets of instrumentation during intensive observation campaigns such as SHEBA program (Uttal et al., 2002) focused on the Beaufort sea region, Mixed-Phase Arctic Cloud Experiment (M-PACE) on the North Slope of Alaska (Verlinde et al., 2007), ASCOS in the central Arctic (Tjernström et al., 2014), and the recent ACLOUD/PASCAL campaign in the Svalbard region (Wendisch et al., 2019).

Shupe et al. (2011) analyzed cloud properties at five observatories in the Arctic, namely Atqasuk, Barrow, Eureka, Summit and Ny-Ålesund. The authors showed that in general the total annual cloud occurrence among all these stations varies from 58-83 %. The highest occurrence of clouds was observed in autumn and ranged from 80 to almost 100%, while the lowest cloud occurrence of ∼60% was typically observed in winter and spring. Shupe et al. (2011) found an unique shift in the cloud annual cycle at Eureka due to distinct meteorological patterns. At Eureka there are less low-level summer clouds and more low- and mid-level winter clouds.

Shupe (2011) analyzed cloud phase at Barrow, Eureka, and for the SHEBA campaign. The authors reported that ice clouds were the predominant type of clouds with the occurrence up to 60–70% at all sites. Liquid phase was observed 56% of the time at Barrow and during the SHEBA campaign but much less frequent at Eureka (30%). It was also shown that the water saturation conditions were reached less frequently at the Eureka station, which lead to lower occurrence of liquid-containing clouds at this site in comparison to the other Arctic sites. Shupe et al. (2015) found

that the monthly mean LWP ranged from 20–110 g m^{-2} at Barrow and was higher than the monthly mean values of IWP varying from 5 to 70 g m^{-2} for all seasons. The highest LWP was observed at Barrow in late summer and early autumn while the largest IWP was observed in early autumn and middle of spring. For the Barrow dataset Shupe et al. (2015) found that the monthly median effective radius of ice particles is about 35 μm throughout a year. The median effective size of liquid particles was typically from 7 to 10 μm.

Shupe and Intrieri (2004) investigated the influence of cloud phase on SW and LW radiation analyzing the data from the SHEBA field camp based on an ice-breaking ship for the period from 1997 to 1998. The authors used the microphysical profiles retrieved from ground-based observations and applied the Santa Barbara Discrete Ordinate Radiative Transfer (DISORT) Atmospheric Radiative Transfer (SBDART) algorithm (Ricchiazzi et al., 1998). The results showed that annually averaged CRE$_{LW}$ and CRE$_{SW}$ for liquid-containing clouds were 52 and –21 W m^{-2}, respectively. For pure ice clouds CRE$_{LW}$ and CRE$_{SW}$ were found to be 16 and –3 W m^{-2}, respectively, indicating that liquid containing clouds are more radiatively effective than ice clouds for the dataset analyzed by Shupe and Intrieri (2004).

Dong et al. (2010) analyzed 10-years of cloud observations at Barrow and found that on average the net CRE at Barrow is 3.5 W m^{-2}. The authors reported that for regions located more to the south from the Barrow station the annual Net CRE is negative (e.g. –17.9 W m^{-2}, Alaska 60°N) while to the north it becomes more positive (e.g. 26.9 W m^{-2} during the SHEBA experiment). Such a latitudinal dependence of CRE may result from the combined effect of SZA and the surface albedo. For the Summit station Miller et al. (2015) found the annually averaged CRE of 33 W m^{-2}. CRE is positive during a year and shows a low seasonal variability, which is opposite to other Arctic sites where CRE is negative in summer.

Until summer 2016 the AWIPEW station at Ny-Ålesund was equipped only with one profiling instrument – ceilometer. Based on observations from the ceilometer Shupe et al. (2011) analyzed macrophysical properties of clouds at Ny-Ålesund, such as cloud occurrence, persistence, and cloud base height. An analysis of microphysical and radiative properties of clouds, similar to the one conducted for the Barrow and Summit stations, was not possible because there was no measurements available from a cloud radar.

1.7   Focus and scientific questions of the thesis

Clouds are one of the major components of the Arctic climate and their accurate representation in climate models is crucial for analysis of the radiation budget. Understanding of clouds is especially important for the Arctic regions experiencing the fastest temperature increase over the last decades. The Svalbard island is currently the only place with continuous active and passive atmospheric profiling located in such a region. Even though, the Ny-Ålesund station is well equipped with instruments continuously monitoring the atmosphere during several decades, the literature review given in this chapter shows a lack of detailed cloud characterization at Ny-Ålesund.

The atmosphere in Svalbard and clouds in particular are strongly affected by the long-distance air transport. Even though there is a general evidence how the air transport influences clouds in the Svalbard area, more information is required in order to link the cold and warm air intrusions with clouds and their radiative effect. This link is one of the missing parts towards a complete surface energy budget similar to those recently carried out by Persson et al. (2017) for the SHEBA campaign. Profiling of cloud microphysical properties at Ny-Ålesund was not possible because only one profiling instrument (ceilometer) was used until summer 2016, when a cloud radar was installed within the $(AC)^3$ project in order to close the gap in cloud observations.

The aim of the current study is to answer the following questions:

- What characteristics do clouds have at Ny-Ålesund?

- How good can a numerical weather prediction model represent cloud properties at Ny-Ålesund?

- How do moist and dry conditions influence cloud properties including occurrence, cloud types, IWP, and LWP at Ny-Ålesund?

- How do changes in cloud properties due to moist and dry conditions influence CRE at Ny-Ålesund?

- Do long-term observations of the atmospheric state at Ny-Ålesund show significant trends in the occurrence of moist and dry conditions over the last decades?

- If there are trends in the occurrence of moist and dry conditions at Ny-Ålesund, what is their impact on LW CRE?

In order to answer these questions, continuous atmospheric observations taken from June 2016 to October 2018 at Ny-Ålesund within the $(AC)^3$ project were used to analyze cloud properties, surface radiation, fluxes, and atmospheric states. A state-of-the-art set of passive, active, and in situ instruments utilized in this study is described in Chapter 2. The widely used processing algorithm Cloudnet was applied by the Finnish Meteorological Institute to the observations. Based on the cloud categorization from Cloudnet, a cloud classification and microhysical retrievals were used to estimate properties of ice and liquid cloud particles. Chapter 3 shows general statistics of cloud properties and gives a comparison of the observations and a numerical weather prediction model. Profiles of the retrieved cloud properties as well as thermodynamic properties of the atmosphere were used by Ebell et al. (2020) as an input for RRTMG simulations. In Chapter 4 cloud properties and CRE from RRTMG are related to moist, dry, and normal conditions at Ny-Ålesund. Long-term trends in occurrence of moist and dry conditions are analyzed in Sec. 4.5.

Since RRTMG requires profiles of cloud properties, the estimated CRE is only available from June 2016 onwards. Nyeki et al. (2019) showed that effects of cloud on the surface radiation can be deducted from LW flux observations and cloud fraction, which, as was shown by Long and Ackerman (2000); Long and Turner (2008), can also be approximated from the surface flux measurements. In order to relate

the long-term trends in atmospheric water vapor to changes in CRE, an algorithm
estimating CRE from available long-term observations is developed. The algorithm
is based on neural networks and uses different combinations of inputs, such as sur-
face LW fluxes, cloud base detection from a ceilometer, brightness temperatures
from a microwave radiometer, surface temperature and humidity. Chen et al. (2006)
have already shown that neural networks are capable of the LW CRE estimation.
The authors used cloud fraction, cloud base height, and cloud base temperature
retrieved from the lidar/radar synergy. In this study, the radar was not available
before June 2016. A long-term lidar dataset is available for Ny-Ålesund (Maturilli
and Ebell, 2018) but the dataset is not homogeneous because lidars of different types
were used (Sec. 2.3). Therefore, even though the developed algorithm is similar to
the approach by Chen et al. (2006), different input parameters were used. The de-
veloped method and its results are presented in Chapter 5. Finally, in Chapter 6 a
summary and an outlook for the future research are presented.

Parts of this thesis have been published:

- Nomokonova T., Ebell K., Löhnert U., Maturilli M., Ritter C., and O'Connor
  E. (2019), Statistics on clouds and their relation to thermodynamic conditions
  at Ny-Ålesund using ground-based sensor synergy. *Atmospheric Chemistry
  and Physics*, vol. 19, no.6, pages 4105-4126, doi: 10.5194/acp-19-4105-2019.
  Parts of this publication are mainly used in Chapters 2 and 3.

- Nomokonova T., Ebell K., Löhnert U., Maturilli M., and Ritter C. (2019), The
  influence of anomalous atmospheric conditions at Ny-Ålesund on clouds and
  their radiative effect. *Atmospheric Chemistry and Physics Discussions*, 1-34,
  doi: 10.5194/acp-2019-985. This publication is mainly used in Chapters 2 and
  4.

Datasets used for the analysis in this thesis have been published:

- Nomokonova T., and Ebell, K. (2019), Cloud microphysical properties re-
  trieved from ground-based remote sensing at Ny-Ålesund (10 June 2016 –
  8 October 2018). University of Cologne, PANGAEA, `https://doi.pangaea.`
  `de/10.1594/PANGAEA.898556`.

- Nomokonova, T., Ritter, C., Ebell, K. (2019), HATPRO microwave radiometer
  measurements at AWIPEV, Ny-Ålesund (2016 – 2018). PANGAEA, `https:`
  `//doi.org/10.1594/PANGAEA.902183`.

Chapter 2

Instrumentation and data products

In this study a set of passive, active, and in situ instrumentation continuously running at the AWIPEV observatory was used. An overview of the measurement site is shown in Fig. 2.1. A cloud radar and a microwave radiometer are installed at the roof on the AWIPEW observatory building, while a ceilometer and radiation sensors are mounted on the ground about 100 m away from the building. In addition, a number of data products derived from the measurements or models are utilized. In this chapter, a review of the instruments, data products, and models as well as a short description of the measurement principles and retrieval methods are given. Information for this chapter is partly taken from Nomokonova et al. (2019b) and Nomokonova et al. (2019a).

2.1 Cloud radar

In this thesis two 94 GHz cloud radars, JOYRAD-94 and MIRAC-A (Fig.2.2), of the University of Cologne are used. Both radars are of the same type and were manufactured by Radiometer Physics GmbH (RPG). JOYRAD-94 and MIRAC-A are vertically pointing radars and utilize frequency-modulated continuous wave (FMCW) signals. Küchler et al. (2017) showed the details on the operational principle and signal processing for JOYRAD-94. JOYRAD-94 was installed at the AWIPEV station on 10th of June 2016 where it was operated until its replacement by MIRAC-A in July 2017. In this study radar data until 8 October 2018 are used. Main hardware parameters and operational settings of the radars are shown in Table 2.1.

The used cloud radars are active instruments which emit radiation in form of periodical frequency-modulated signals (also known as chirps) to the atmosphere and receive a signal returned by atmospheric scatters. Ranging in FMCW radars is performed by measuring frequency differences between the transmitted and received signals, which are proportional to the distance at which the scatters are located. The returned power P_r measured by the radars is defined by properties of scatters and by radar specifications. In order to get a quantity independent on the radar characteristics, P_r is usually converted to so called equivalent radar reflectivity factor (Z, radar reflectivity hereafter):
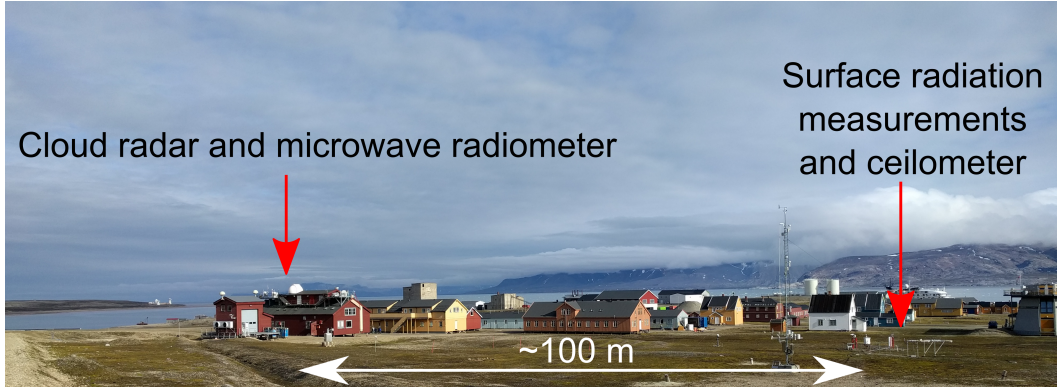
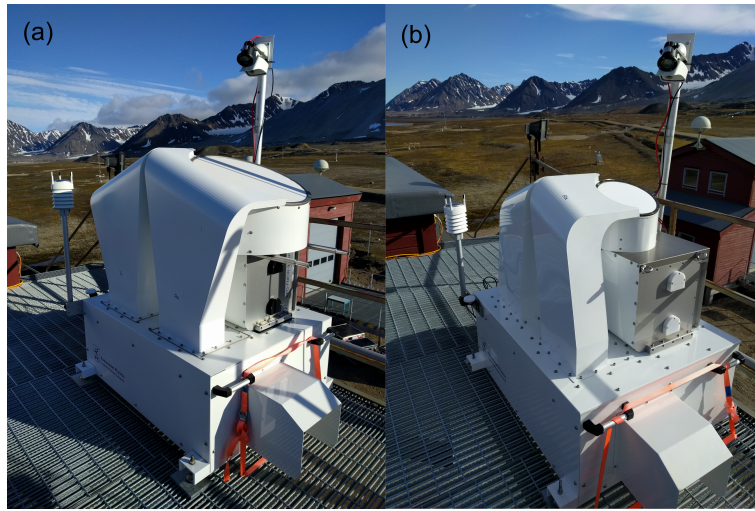Figure 2.1: Overview of the AWIPEV measurement site at Ny-Ålesund.

Figure 2.2: The 94 GHz cloud radars JOYRAD (a) and MIRAC-A (b) mounted on the roof of the AWIPEV station at Ny-Ålesund.

$$Z = |K_w|^{-2} C_a P_r r^2, \tag{2.1}$$

where $|K_w|$ is the dielectric factor of liquid water, C_a is the radar constant, which takes into account the radar specifications, and r is range from the radar to the scatters. Z has units of $\text{mm}^6\ \text{m}^{-3}$ but often logarithmic units $\text{dBZ} = 10\log_{10}(\text{mm}^6\ \text{m}^{-3})$ are used.

For spherical cloud particles with sizes much smaller than the wavelength, Z is proportional to the sixth raw moment of the size distribution:

$$Z \sim \int_0^\infty D^6 N(D) dD. \tag{2.2}$$

Here D is the size of a scatter and $N(D)dD$ is a number of particles in a unit volume with sizes ranging from D to $D + dD$. Equation 2.2 shows that in the case of Rayleigh scattering the radar reflectivity is mostly dominated by a presence of larger particles (Hogan et al., 2006).

Table 2.1: Specifications of the used radars.

Parameter	JOYRAD-94	MIRAC-A
Transmitted power [W]	1.5	1.2
Antenna gain [dBi]	50.1	46.5
Beam width [°]	0.56	0.95
Polarisation	Vertical	
System noise figure [dB]	4–5	
Sampling period [s]	2.5	2
Vertical resolution	4 m (100-400 m), 5.3 m (400-1200 m), 6.7 m (1.2-3 km), 17 m (3-10 km)	3.2 m (100-400 m), 7.5 m (400-1200 m), 9.7 m (1.2-3 km), 23.8 m (3-10 km)
Sensitivity at 5 km [dBZ]	–40	–34

Sensitivities of JOYRAD-94 and MIRAC-A at 5 km distance for the settings given in Table 2.1 are about –40 and –34 dBZ. The total radar reflectivity uncertainty consists of the calibration bias which is within ±0.5 dB (Küchler et al., 2017), the random error, and the gas/liquid attenuation uncertainty. The random error depends on a number of independent measurements, which is for the 30 s sampling varies from 60 to 120 for the used settings for both radars (see Table 2.1). Taking into account the non-coherent averaging of the independent measurements (Bringi and Chandrasekar, 2001, Eq. 5.193) the standard deviation of the random error is in the order of 0.5 dB.

The used cloud radars have Doppler capabilities, i.e. they can track phase changes between chirps caused by motions of atmospheric particles. From a sequence of received signals cloud radars estimate Doppler spectra, which represent a velocity distribution of the radar reflectivity. The radars calculate moments of Doppler spectra, such as mean Doppler velocity, and spectrum width.

Profiles of the radar reflectivity factor and the mean Doppler velocity were used in the Cloudnet algorithm (Sec. 2.6) for cloud detection, characterization, and microphysical retrievals. In this study, the analysis of the first year of radar observations at Ny-Ålesund when JOYRAD-94 was operating is presented in Chapter 3. The whole period of radar observations is investigated in Chapters 4 and 5.

2.2   Microwave radiometer HATPRO

The microwave radiometer (MWR) HATPRO (humidity and temperature profiler; Rose et al., 2005) is a passive instrument that measures atmospheric brightness temperatures (TB) with fourteen channels. Six K-band channels (from 22 GHz to 28 GHz) are located on the right slope of the water vapor absorption line near 22 GHz. A 31.4 GHz channel is located in the atmospheric window and, thus, is more sensitive to presence of atmospheric liquid water. TBs measured at K-band are used for retrievals of integrated water vapor (IWV), LWP, and humidity profiles. Seven V-band channels (from 51 GHz to 58 GHz) are located along the oxygen absorption complex near 60 GHz and are used for vertical temperature profiling.

Figure 2.3: MWR HATPRO mounted on the roof of the AWIPEV station at Ny-Ålesund.

MWR has been measuring at AWIPEV station, Ny-Ålesund, since 24 March 2011 (Fig. 2.3). This instrument operates continuously but cannot provide reliable information under rain conditions, when the instrument radome is wet. In these cases TB data are flagged and excluded from an analysis.

In order to derive LWP and IWV as well as temperature and humidity profiles a multivariate linear regression algorithm developed at the University of Cologne (Löhnert and Crewell, 2003) was used. The regression coefficients are obtained from TBs simulated from a long-term radiosonde dataset. Since the algorithm relies on climatological data for a certain location, the retrievals were adapted for an operation at Ny-Ålesund (Nomokonova et al., 2019b). The site specific regression coefficients were obtained from TBs simulated using a radiative transfer model (RTM). The model was applied to a dataset of almost 3800 Ny-Ålesund radiosondes (from 2006 to 2016, Sec. 2.4). In addition to routinely applied GRUAN processing (Sec. 2.4) for the RTM model the radiosonde data were quality controlled according to Nörenberg (2008). Radiosondes that did not reach the 30 km height were extended with climatological profiles.

Initially, the retrievals are directly applied to TBs measured by the MWR. Nevertheless, the measured TBs are subject to offsets due to long-term drifts in the receiver gains. Therefore, the radiometer measurements have been corrected for TB offsets according to Löhnert and Maier (2012). The assessment of the TB offsets allows reducing systematic errors in TBs originated from instrumental effects as well as from radiative transfer simulations. The offsets were determined as an average difference between simulated and measured TB under conditions with no liquid water in the atmosphere. The differences were averaged for each period between two absolute calibrations of the instrument. In order to identify radiosonde profiles with no liquid water, 2 min standard deviations of LWP estimated by MWR were checked within 20 minutes before and after a radiosonde launch. If all standard deviation values of the LWP within the 40 minutes did not exceed 1.2 g m^{-2} the profile is considered to be free of liquid-water. After the measured TBs have been corrected
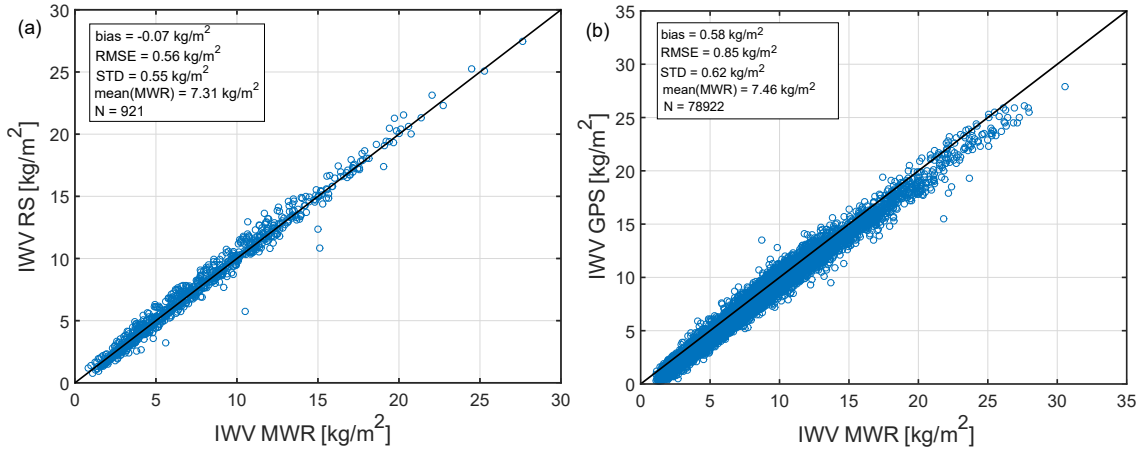
Figure 2.4: IWV comparison between MWR and radiosonde (only around 11 UTC radiosondes included) for the period from 2011 to 2017 (a) and MWR and GPS (1131 days) for the period from 2013 to 2016 (b).
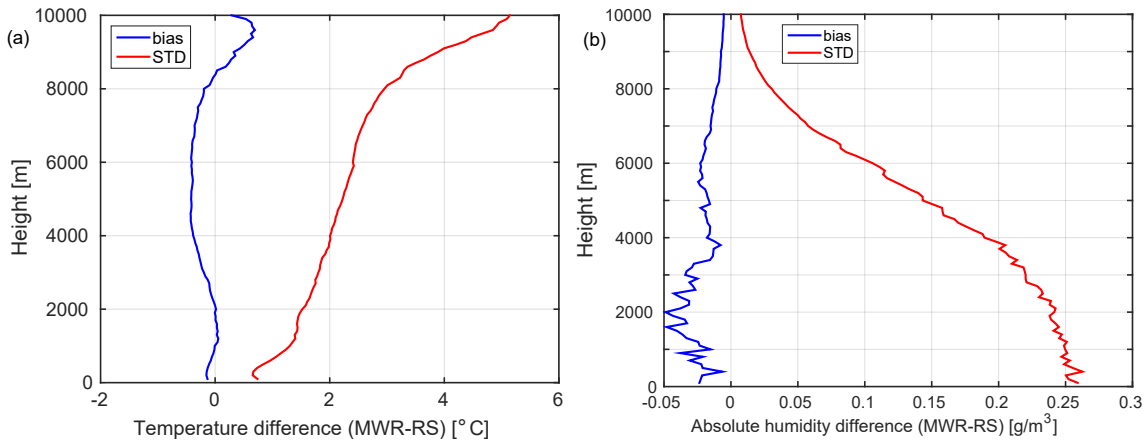

Figure 2.5: Difference in temperature (a) and relative humidity (b) between MWR and radiosonde data for the period from 2011 to 2017. Blue and red lines show the bias and the standard deviation, respectively.

for the corresponding offsets, the retrievals were applied to the corrected values of the TBs.

In order to assess uncertainties, the variables retrieved from MWR were evaluated using estimates from other sources. Figure 2.4a shows a comparison of the IWV from MWR and radiosondes. The values are in a good agreement with root mean squared error (RMSE) of 0.56 kg m^{-2}. Another source of IWV is Global Positioning System (GPS). The GeoForschungsZentrum Potsdam runs the EPOS software (Ge et al., 2006) that provides IWV estimates with a temporal resolution of 15 min and an accuracy of 1–2 kg m^{-2} (Dick et al., 2001; Gendt et al., 2004). For the comparison IWV from MWR was averaged over 15 min intervals taken after GPS time samples. The comparison between MWR and GPS IWV for the period from 2013 to 2016 (Figure 2.4b) shows a good agreement with RMSE of 0.85 kg m^{-2}. These results are consistent with Steinke et al. (2015), who compared IWV from MWR and GPS for mid-latitudes and reported RMSE of 0.91 kg m^{-2}.

Figure 2.5 shows differences between temperature and absolute humidity retrieved

from MWR and measured by radiosondes. The bias in temperature is slightly height dependent and is within ± 0.5°C. The standard deviation of the temperature difference increases from about 1 °C near the surface to 5 °C at 10 km height. The bias in absolute humidity ranges from -0.01 to -0.05 g m^{-3} up to 10 km. The standard deviation of the absolute humidity difference ranges from 0.01 to 0.25 g m^{-3}. Uncertainty in LWP retrieved from MWR is typically 20-25 g m^{-2} (Rose et al., 2005).

In this thesis LWP retrieved from MWR observations is used to quantify the total amount of liquid in cloudy profiles. LWP is also utilized as an input for Cloudnet (Sec. 2.6). Temperature profiles and IWV retrieved from MWR are used to characterize atmospheric states at Ny-Ålesund in Chapter 4.

2.3   Ceilometer

Ceilometer is an active instrument which emits laser pulses into the atmosphere and measures the return signal scattered by atmospheric particles. Since ceilometer is sensitive to a high concentration of liquid particles and aerosols (Hogan et al., 2006), it is suitable for detection of liquid layers and cloud base heights. However, the near-infrared signal is strongly attenuated by liquid layers (optical depth more than 3) and therefore, ceilometer can often miss the liquid particles above the lowest optically thick liquid layer. Ceilometers are also used for detection of high level ice cloud (Protat et al., 2006) but, as was shown by Bühl et al. (2013), the detection of clouds with IWC less than 10^{-6} g/m^3 is challenging.

Since 1992 ceilometers have been operated at the AWIPEV station in Ny-Ålesund (Maturilli and Ebell, 2018). During this period three types of ceilometers were used to provide cloud base height observations. The period of measurements and technical characteristics of each ceilometer type are shown in Table 2.2. Due to technical issues the ceilometer data was missing in February 1993, from February to May 1997, from December 1999 to March 2000, and in March 2000 (Maturilli and Ebell, 2018).

The maximum cloud reporting range for LD-WHX05 was up to 3650 m, which is much lower in comparison to other two ceilometers (13 km). This might have led to underestimation of cloud occurrence from 1992 to 1998. Maturilli and Ebell (2018) noticed that in summer the cloud occurrence estimated from LD-WHX05 was consistent with the other two ceilometers, while in other seasons and especially in winter LD-WHX05 showed unrealistically low cloud occurrence. Therefore, for this study only the data from ceilometers LD-40 and CL51 were used in the analysis of cloud occurrence.

For the Cloudnet algorithm (Sec. 2.6) attenuated backscatter profiles from the ceilometer CL51 are utilized. The calibration technique applied to the measured attenuated backscatter coefficient described in O'Connor et al. (2004) has uncertainties of 10%.

Table 2.2: Specification of ceilometers.

Type (wavelength)	Operation period	Sampling [s]	Range resolution [m]	Maximum range [km]
LD-WHX05	1 August 1992 to 13 July 1998	300	10 (below 300 m), 20 (above 320 m)	3.7
LD-40 (855 nm)	14 July 1998 to 24 August 2011	15	7.5	13
CL51 (905 nm)	25 August 2011 to 8 October 2018	12-20	10	13

Table 2.3: Radiosondes used for this study.

Type	Period	Temporal and vertical resolution
RS80-A	1993 to July 2002	1 s, 50 m (<10 km), 100 m (<30 km)
RS90	23 July 2002 to 20 May 2006	1 s, 50 m (<10 km), 100 m (<30 km)
RS92	21 May 2006 to May 2017	1 s, 5-7 m
RS41	May 2017 to October 2018	1 s, 5-7 m

2.4 Radiosondes

Radiosondes have been launched at AWIPEV at least once per day at around 11 UTC for more than two decades (Maturilli and Kayser, 2016). The radiosondes provide vertical profiles of temperature, humidity, pressure, wind speed, and wind direction.

From 21 of May 2006 to 2 May 2017 all radiosondes were of the type Vaisala RS92 and have been processed using the GRUAN version 2 data processing algorithm (Sommer et al., 2012; Maturilli and Kayser, 2016). The processing corrects for errors temperature due to the heating effect by solar radiation and for humidity errors due to a radiation dry bias (Dirksen et al., 2014). Dirksen et al. (2014) reported that for altitudes below 10 km the remaining uncertainties in temperature are up to 0.25°C and 0.15°C for day and night time, respectively, and 4% for relative humidity. Since 2 May 2017 the radiosonde type was changed to Vaisala RS41. The accuracy of the RS41 radiosonde type reported by manufacturer is 0.1°C for temperature and <2% for relative humidity. In the present work the radiosonde data were utilized to characterize the thermodynamic state at Ny-Ålesund for the period from 1993 to 2018.

2.5 Baseline surface radiation network BSRN

The surface radiation measurements have been performed at the Ny-Ålesund AW-IPEV station as a part of the Baseline Surface Radiation Network (BSRN) since

Table 2.4: BSRN instruments and data used for this study.

Type	Period of measurements	Measured quantities
Precision Infared Radiometer (Pyrgeometer), (3500-50000 nm)	August 1992 to October 2018	longwave downwelling radiation
Precision Infared Radiometer (Pyrgeometer), (3500-50000 nm)	August 1992 to October 2018	longwave upwelling radiation
Hair Hygrometer	August 1993 to 28 July 2002	2 m relative humidity
Humidity and Temperature Transmitter HMP233 (HUMICAP)	25 October 1999 to October 2018	2 m relative humidity
Termometer sensor PT100	28 July 2002 to October 2018	2 m temperature

August 1992. An overview of BSRN instruments used in this study is given in Table 2.4.

Longwave radiation is measured with two precision infrared radiometers (PIR) manufactured by The Eppley Laboratory, Inc. PIR has a thermopile detector which is installed under a protective hemispheric interference filter transparent to the longwave radiation between 3.5 and 50 μm. One PIR measures upwelling radiation and, therefore, is pointed to the ground. Another PIR measured downwelling radiation. This instrument is shaded from the direct solar radiation in order to avoid temperature drifts by incoming solar radiation. Both PIRs are ventilated. The uncertainty of the measured longwave fluxes reported by the manufacturer is 5 W m^{-2} with a zero offset of 2 W m^{-2}. Similarly, Lanconelli et al. (2011) repoted that the uncertainty for the longwave downward radiation does not exceed $\pm$10 W m^{-2}.

The measured down- and upwelling longwave radiation for the period from 1992 to 2013 was obtained from the dataset described by Driemel et al. (2018). The period from 2013 to 2018 is available at the PANGAEA repository.

Collocated meteorological observations started at Ny-Ålesund AWIPEV station in August 1993 (Maturilli et al., 2013). 2-m temperature is measured by the PT-100 thermometer manufactured by the Thies Clima company. The thermometer is protected by a weather and thermal radiation shield and has a ventilator inside. The temperature range is from -30° to +80°C. The accuracy of temperature reported by the manufacturer is $\pm$0.1°C. In the period from 1993 to 1999 relative humidity was measured by a hair hygrometer from Thies Clima. This instrument was protected by a weather and thermal radiation shield. The manufacturer reported the accu-

Table 2.5: Cloudnet characteristics for Ny-Ålesund.

Property	Value
Input parameters (Instrument/model)	LWP (MWR), reflectivity factor and Doppler velocity (94 GHz radar), attenuated backscatter coefficient (ceilometer CL51), hourly model analysis and forecasts (GDAS1 or NWP ICON model)
Temporal resolution	30 s
Vertical resolution (range)	20 m
Retrieved parameters	Target classification, IWC

racy in relative humidity of 2% in the range 10 to 100% and ambient temperature from -35° to +70°C. In October 1999 the Thies Clima hygrometer was exchanged by the Vaisala HUMICAP sensor. The reported accuracy of the HUMICAP sensor at temperatures from -40° to +80°C is $\pm 1\%$ for the measurement range from 0 to 90% and $\pm 2\%$ for the range from 90 to 100%. The long-term 2 m temperature and relative humidity observations from 1993 to 2011 were obtained from the homogenized dataset presented by (Maturilli et al., 2013).

2.6 Cloudnet data products

The Cloudnet algorithm suite (Illingworth et al., 2007) combines observations from a synergy of ground-based instruments. Cloudnet output includes several products such as a cloud target classification and microphysical properties (e.g. IWC, liquid water content (LWC)). In order to provide the full vertical information on clouds, Cloudnet requires measurements of a Doppler cloud radar, a ceilometer/lidar, a microwave radiometer, and thermodynamic profiles of a numerical weather prediction (NWP) model. Table 2.5 gives an overview on the Cloudnet products used for the cloud analysis and provides input parameters and model data for the Cloudnet algorithm. For Ny-Ålesund, measurements are taken from the 94 GHz FMCW cloud radars JOYRAD-94 and MIRAC-A (Sec. 2.1), the ceilometer CL51 (Sec. 2.3), and the HATPRO MWR (Sec. 2.2) for the period from June 2016 to 8 October 2018.

Within Cloudnet, the measurements from different instruments are scaled to a common temporal and vertical grid of 30 s and 20 m, respectively. For the target classification the lidar backscatter and Doppler radar parameters are analyzed in combination with thermodynamic profiles of a model (Hogan and O'Connor, 2004). The Cloudnet algorithm corrects the radar reflectivity for the attenuation by atmospheric gases and liquid water. Temperature, humidity, and pressure profiles from a model are used by the Cloudnet for the corrections. The two-way uncertainty of the gas-attenuation estimated by Hogan and O'Connor (2004) is about 10%. The uncertainty of 25 g m^{-2} in LWP from MWR causes about ± 0.2 dB uncertainty in the two-way attenuation at the W-band (Matrosov, 2009).

As an example, measurements from the radar and the ceilometer, and the Cloudnet target classification on 29 September 2016 are shown in Fig.2.6. The target
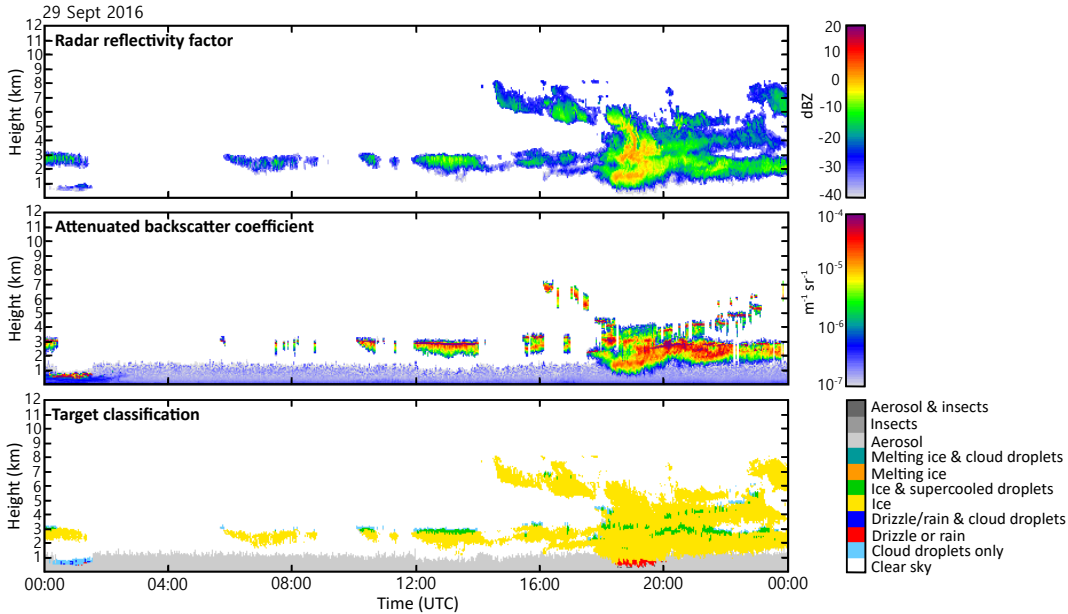
Figure 2.6: Radar reflectivity factor (top), lidar backscatter coefficient (middle) and Cloudnet target classification on 29 September 2016, AWIPEW observatory at Ny-Ålesund (published in Nomokonova et al. (2019b)). The quicklooks are taken from the official Cloudnet website (`http://devcloudnet.fmi.fi/`).

classification consists of the categories such as aerosols, insects, melting ice, cloud droplets, ice and supercooled droplets, drizzle/rain, and clear sky. In this study, the Cloudnet target categorization is used to differentiate cloud phase (liquid, ice and mixed-phase) and to identify different cloud types. For the classification the Cloudnet algorithm also needs temperature profiles from model data. Model data are taken from GDAS1 (Global Data Assimilation System) or NWP ICON.

The Global Data Assimilation System (GDAS; Kanamitsu, 1989) operated by the US National Weather Service's National Centers for Environmental Prediction (NCEP) was used in the Cloudnet algorithm to provide thermodynamic information for the period from 10 June 2016 to 31 January 2017. This system analyzes different type of observations and maps the results on a grid used for model initializations. The GDAS1 dataset (see `https://www.ready.noaa.gov/gdas1.php` for detailed information) has 1° by 1° latitude-longitude grid and is initialised every 6 hours and outputs an analysis timestep followed by forecasts with a temporal resolution of 3 hours on 23 pressure levels. The vertical resolution varies from 173 m near the ground to 500 m at the height 2 km and to ∼2.5 km at the height of 15 km. The uncertainties of the temperature and relative humidity profiles of GDAS1 are shown in Fig. 2.7. The maximum errors in temperature and relative humidity do not exceed -1+/-1.5 °C and -15+/-24%, respectively.

The ICON column output for Ny-Ålesund taken from the operational global ICON model run is available since 1 February 2017 and has been used as an input for the Cloudnet algorithm since then. The ICOsahedral Non-hydrostatic (Zängl et al., 2015) modeling framework for global NWP and climate modeling is developed by the German Weather Service and the Max Planck Institute for Meteorology. The grid structure of ICON is based on an icosahedral (triangular) grid with an average
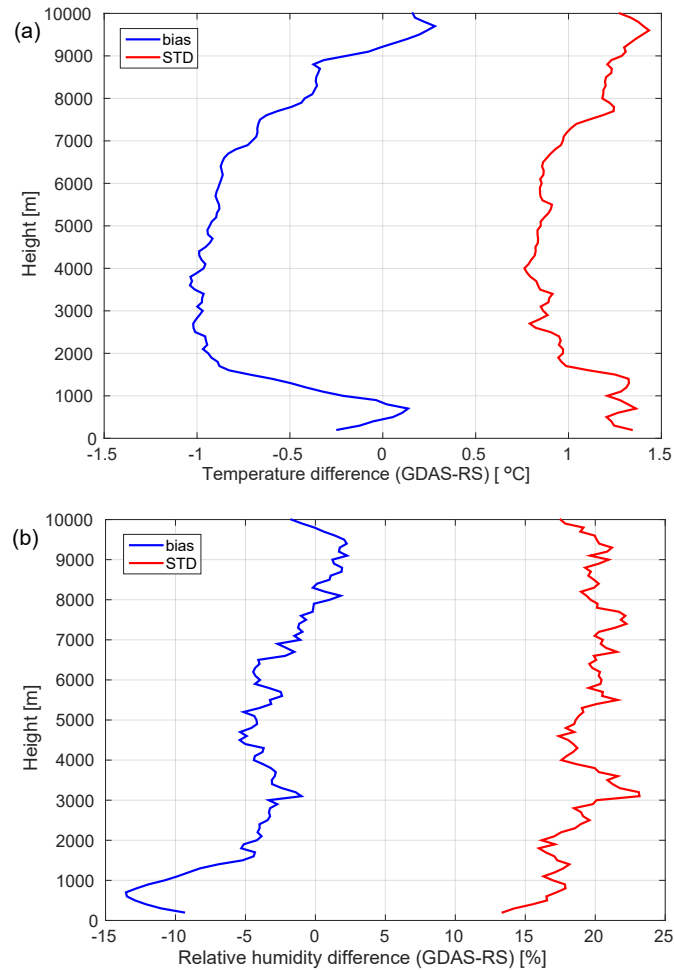
Figure 2.7: Difference in temperature (a) and relative humidity (b) between GDAS1 and radiosonde data. Radiosondes for the period from February 2017 to July 2017 at Ny-Ålesund are used. Blue and red lines show the bias and the standard deviation, respectively. (published in Nomokonova et al. (2019b))

resolution of 13 km. The averaged area of the triangular grid cells is 173 km^2. In the vertical dimension, the model has 90 atmospheric levels up to the maximum height of 75 km. The vertical resolution ranges from 30 m at the lowest heights to about 500 m at about 15 km height. The vertical resolution at the 2 km height is about 260 m. In addition, for this study a column output for Ny-Ålesund taken from the operational global ICON model run was also used to exemplarily show how such an observational dataset of clouds can be used for a model evaluation. In particular, vertical profiles of environment temperature and humidity, specific cloud water content, specific cloud ice content, rain mixing ratio and snow mixing ratio were used. The occurrence of different types of clouds in the ICON model is related to temperature and humidity and the results are compared to the observational statistics. ICON model runs over Ny-Ålesund column are performed twice a day at 00 UTC and 12 UTC with a forecast for 7.5 days (180 hours) and hourly output intervals. The data only from the first 12 hours after the initialization of the model run were used in our analysis. The uncertainties of the temperature and relative
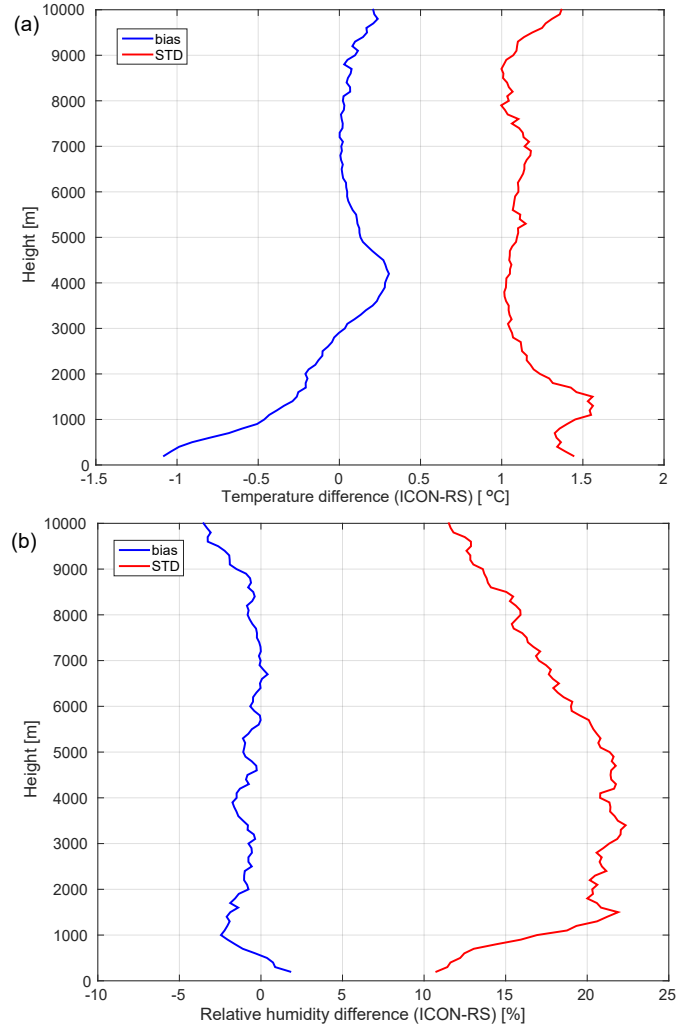
Figure 2.8: Difference in temperature (a) and relative humidity (b) between the ICON column output over Ny-Ålesund and radiosonde data for the period from February 2017 to October 2018. Blue and red lines show the bias and the standard deviation, respectively. (published in Nomokonova et al. (2019b))

humidity profiles of the ICON model are shown in Fig. 2.8. The maximum errors in temperature and relative humidity at the altitude up to 10 km are -1.5+/-1.5 °C and -5+/-20%, respectively.

For the target classification, the Cloudnet algorithm identifies the 0°C isotherm using the wet-bulb temperature calculated from the model data. Therefore, the model uncertainties (Figs. 2.7 and 2.8) may lead to the liquid-ice misclassification at temperatures close to 0°C. In the case of precipitating clouds uncertainties of the model are mitigated by the Cloudnet algorithm using radar Doppler observations. The algorithm identifies the 0°C isotherm by a significant gradient in the particles vertical velocity.

For the analyzed period (10 June 2016 - 8 October 2018), the Cloudnet availability is more than 90% availability for most of the months (Fig.2.9). Exceptions are June-July 2016 due to installation and testing of the radar, February 2017 (software update), October and December 2017 (due to technical issues), and October
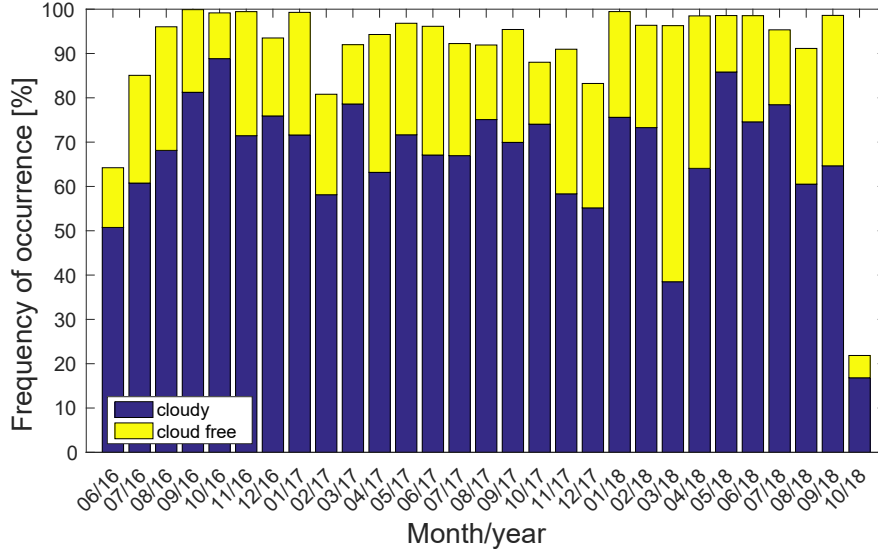
Figure 2.9: Cloudnet data availability for Ny-Ålesund for 10 June 2016 to 8 October 2018. Yellow bars correspond to clear sky profiles, dark blue bars to cloudy profiles, white space means no Cloudnet data availability. (adapted from Nomokonova et al. (2019b))

2018 (deinstallation of the MIRAC-A radar on 8th October). The total number of available Cloudnet profiles is 2,313,647 that include 609,047 clear sky profiles and 1,704,600 cloudy profiles.

Based on the target classification, various cloud microphysical retrievals are applied within Cloudnet. The Cloudnet IWC product, which is used in this study, is based on a Z-IWC-T relation for 94 GHz (Hogan et al., 2006; Heymsfield et al., 2008):

$$\log_{10}(\text{IWC}) = 5.8 \times 10^{-4} ZT + 9.23 \times 10^{-2} Z - 7.06 \times 10^{-3} T - 0.992, \qquad (2.3)$$

where Z is in dBZ and T is air temperature in °C. The Cloudnet IWC has a bias error and typical random error of 0.923 dB and 1.76 dB, respectively. Hogan et al. (2006) found that uncertainties of the IWC retrieval differ for different temperature ranges and are estimated to be from –50% to +100% for temperatures below –40°C and ranging from –33% to 50% for temperatures above –20°C. The numbers here are root mean squared errors given with respect to the reference IWC. Evaluating the method of Hogan et al. (2006), Heymsfield et al. (2008) found similar uncertainties, except that there was a positive bias of about 50% for temperatures above –30°C. The authors estimated the uncertainties from 0% to +100% and from –50% to +100% at temperatures above and below –30°C, respectively. The uncertainty in the radar reflectivity also influences the IWC retrieval. The total uncertainty of 2 dB corresponds to about +40/–30% uncertainty in IWC. Part of this uncertainty is to be included into the uncertainty of the Z-IWC-T relation from Hogan et al. (2006) because the relation was found empirically using radar observations. More detailed information on the Cloudnet products can be found in Illingworth et al. (2007).

2.7   Cloud microphysical dataset

Using the target characterization, cloud areas with ice and liquid particles were identified. For ice particles the effective radius $r_{\text{eff,ice}}$ was calculated following the method by Delanoë et al. (2007, Eq. 10):

$$r_{\text{eff,ice}} = \frac{3 \cdot \text{IWC} \cdot 10^6}{2\rho_i \cdot \alpha_{ext}}, \tag{2.4}$$

where $r_{\text{eff,ice}}$ is in μm, ρ_i is a density of solid ice (0.917 g cm^{-3}), IWC is derived using Eq. 2.3 and α_{ext} is a visible extinction coefficient derived according to Hogan et al. (2006):

$$\log_{10}(\alpha_{ext}) = 8.76 \times 10^{-4}ZT + 9.28 \times 10^{-2}Z - 5.13 \times 10^{-3}T - 2.49. \tag{2.5}$$

In Eq. 2.5 α_{ext} is in m^{-1}, Z is the radar reflectivity at 94 GHz in dBZ, and T is in °C. The retrieval algorithm for IWC and $r_{eff,ice}$ was applied to range bins where particles have been detected regardless of presence of liquid particles, since in the case of coexisting ice and liquid particles Z is mostly dominated by the ice phase Shupe and Intrieri (2004).

The uncertainties of the α_{ext} retrieval at 94 GHz estimated by Hogan et al. (2006) vary for different temperature ranges. At temperatures above –20°C the uncertainties are similar to the uncertainties in IWC. For temperatures below –40°C the uncertainties in α_{ext} range from –62 to 160 %. However, Hogan et al. (2006) reported that the larger error might be expected for α_{ext}, because Z is mostly defined by larger particles while α_{ext}, which is proportional to the second moment of particle size distribution, depends more on smaller ice particles. Hogan et al. (2006) estimated relative uncertainty for $r_{\text{eff,ice}}$ associated to the mass-size relationship to not exceed 30 %. de Boer et al. (2009) reported that the assumed shape of ice particles might result to 200 μm of uncertainties in the effective diameter estimated using cloud radar and lidar techniques.

Retrievals of LWC and effective radius of cloud droplets $r_{\text{eff,liq}}$ were applied to range bins with a presence of cloud droplets according Cloudnet categorization product. LWC and $r_{\text{eff,liq}}$ for single-layer liquid clouds were derived following the methods by Frisch et al. (1998) and Frisch et al. (2002), respectively. LWC is calculated as follows:

$$\text{LWC} = \frac{\text{LWP} \cdot Z^{0.5}}{\sum_{i=1}^{M} Z^{0.5} \cdot \Delta z}, \tag{2.6}$$

where LWP is the liquid water path measured by MWR in kg m^{-2}, Z is in mm^6 m^{-3}, M is the number of range bins within the cloud, and Δz is the range resolution of Cloudnet (20 m). For the retrieval of $r_{\text{eff,liq}}$ for single-layer liquid clouds it is assumed that cloud droplets are lognormally distributed:

$$r_{\text{eff,liq}} = \frac{Z^{1/6}}{2\text{LWP}^{1/3}} \left(\frac{\pi\rho_w}{6}\right)^{1/3} \left(\sum_{i=1}^{M} Z_i^{0.5}\Delta z\right)^{1/3} e^{-2\sigma_x^2} \tag{2.7}$$

where Z is in $mm^6\,m^{-3}$, ρ_w is the water density ($1000\,kg\,m^{-3}$), σ_x is the logarithmic spread of the distribution. σ_x is assumed to be constant with height and according to Miles et al. (2000) is equal to 0.3 for typical marine clouds. The uncertainty of $r_{\text{eff,liq}}$ estimated by Frisch et al. (2002) is about 20%.

Equations 2.6 and 2.7 are only applicable to single-layer liquid clouds. In presence of rain or drizzle few large droplets, which have relatively low contribution to LWC, dominate the radar signal and, therefore, the assumed relations between Z, LWC, and $r_{eff,liq}$ are not valid. In addition, as has been mentioned in Sec. 2.2, measurements from MWR in rain have larger uncertainties due to the wet radome. Thus, the retrievals of LWC and $r_{\text{eff,liq}}$ are not applied to profiles with rain and drizzle.

For mixed-phase clouds, in which ice and liquid particles may be present in the same volumes, partitioning of the radar reflectivity associated with liquid and ice particles is challenging and, therefore, methods by Frisch et al. (1998) and Frisch et al. (2002) can not be directly applied. In these cases the approach by Shupe et al. (2015) is followed. LWC profiles are calculated using the adiabatic assumption and scaled by LWP from MWR. The same scaled-adiabatic assumption was used for profiles with multi-layer liquid and mixed-phase clouds. For these cases the effective radius of $5\ \mu m$ is assumed. This value corresponds to the median value of all $r_{\text{eff,liq}}$ derived at Ny-Ålesund using Eq. 2.7.

The dataset of the retrieved microphysical properties is published by Nomokonova and Ebell (2019) and available online (`https://doi.pangaea.de/10.1594/PANGAEA.898556`). The retrieved cloud microphysical properties are essential for evaluation of profiles in NWP models and for cloud-radiation interaction studies. The derived profiles of clouds and their microphysical properties, and the output of radiative transfer model RRTMG described in Sec. 2.8.1 are used to calculate the cloud radiative effect (denoted as CRE throughout the study) at Ny-Ålesund.

2.8 Model data products

2.8.1 Broadband radiative transfer model RRTMG

The rapid radiative transfer model RRTMG (Clough et al., 2005) performs broadband radiative transfer calculations of vertically resolved shortwave (SW) and longwave (LW) up- and downward fluxes and heating rates. Ebell et al. (2020) adapted RRTMG for Ny-Ålesund and derived SW and LW up- and downward fluxes and CRE. In this study the surface CRE, which is an output of the RRTMG model, is analyzed with respect to periods with increased/decreased moisture and temperature and normal conditions at Ny-Ålesund. The analysis of the CRE during the above-mentioned periods is presented in Chapter 4.

Ebell et al. (2020) estimated the uncertainties in CRE using 10-min averaged fluxes observed by BSRN. The uncertainties in CRE depend on averaging time. For time periods ranging from days to month, which are analyzed in this study, the uncertainties are estimated to be smaller than 6.4, 2.0, and 6.7 W m^{-2} for SW, LW, and net CRE, respectively. More detailed information on RRTMG and input parameters used for calculations can be found in Ebell et al. (2020).

2.8.2 Backward trajectories FLEXTRA

In order to analyze air transportation patterns and relate them to different atmospheric conditions at Ny-Ålesund, the output of the 3-dimensional FLEXTRA trajectory model version 3.0 (Stohl et al., 1995; Stohl and Seibert, 1998; Stohl, 1998) was used. The calculations of the trajectories are based on data of the European Centre for Medium range Weather Forecast (EMCWF) with the initialized analyses every 6 hours and horizontal resolution of 1.125°. The temporal resolution of the backward trajectories is 3 hours. The precalculated FLEXTRA files for the Zeppelin station (78.9°N 11.88°E) are available on the website, (see https://projects.nilu.no//ccc/trajectories/evdc/ for detailed information). For this thesis trajectories going 6 days back and having the arrival height of 1500 m were used. Since Ny-Ålesund is surrounded by up to 1000-m high mountains, the arrival height of 1500 m altitude was chosen in order to avoid orographic effects in the large scale air transport.

Chapter 3

Classification of hydrometeors and clouds at Ny-Ålesund, Svalbard

This chapter presents statistics of thermodynamic conditions and cloud properties at Ny-Ålesund. For the first time, cloud properties at AWIPEV site were retrieved using a synergy of a cloud radar, a ceilometer, and a microwave radiometer. The characterization of clouds is based on outputs of the Cloudnet algorithm and includes classification of hydrometeors and clouds, and estimation of ice and liquid water paths. In Secs. 3.2 and 3.3 vertical hydrometeor distributions and occurrence of different cloud types at Ny-Ålesund are analyzed. LWP and IWP of single-layer clouds are shown in Sec. 3.4. In addition Sec. 3.4 shows how the cloud occurrence is related to in-cloud temperature and relative humidity, since these parameters strongly affect formation and development of cloud particles. These results are compared to an output of the ICON model for Ny-Ålesund in Sec. 3.5. The content of this chapter is as it is published in Nomokonova et al. (2019b), where the period from June 2016 to July 2017 was analyzed. Nevertheless, cloud classification algorithm described in this chapter is further applied to the whole period of observations until October 2018. The results of this classification are used in the following chapters.

3.1 Thermodynamic conditions

It is well known that environmental temperature and humidity strongly influence cloud formation and development. Therefore, the analysis was started with an insight into the thermodynamic conditions during the period from June 2016 to July 2017. In this section the representative of this time period was checked in terms of thermodynamic conditions in comparison to the long-term mean.

Figure 3.1a shows the monthly mean atmospheric temperature based on the radiosonde data for the period from June 2016 to July 2017. The atmospheric temperature follows an annual cycle typical for the Northern hemisphere with higher temperatures during summer and autumn and lower temperatures in winter and spring. The lowest values of the monthly mean temperature in the lowest 50 m were observed in March and January 2017 (-11° and -10°C, respectively). The highest observed monthly mean temperature was +7°C in July 2016. Looking at the monthly mean temperature at 5 km height, the minimum and the maximum values
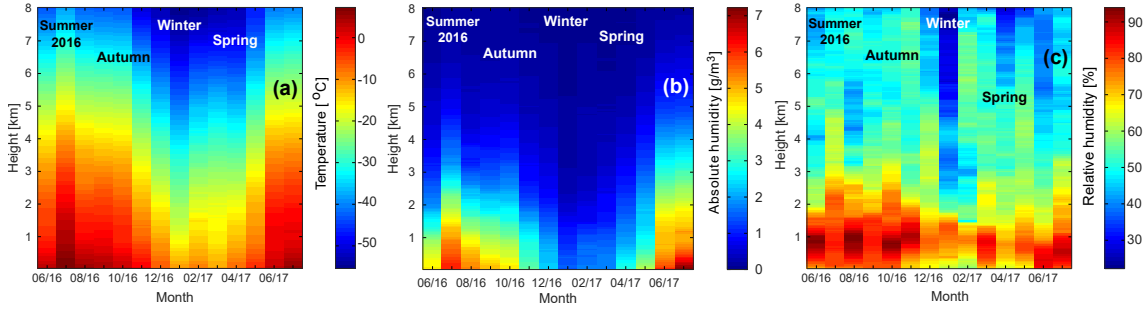
Figure 3.1: Vertical profiles of monthly mean atmospheric temperature (a), absolute (b) and relative humidity (c) from radiosonde observations at Ny-Ålesund from June 2016 to July 2017. (published in Nomokonova et al. (2019b))

of -41° and -17°C were found in January and July, respectively. Despite the fact that Ny-Ålesund is located at the coastline where the climate is supposed to be less variable due to the impact of the ocean, the monthly mean temperature changes by 19° and 24°C in the lowest 50 m and 5 km height, respectively. This large amplitude of the temperature change at Ny-Ålesund can be explained by the regular occurrence of polar day and polar night. When a polar night begins in the beginning of October, atmospheric temperature dramatically decreases and it starts to increase again in late March (Fig.3.1a). Moreover, the smaller temperature variance at lower altitudes might be related to processes between the surface and the atmosphere and the conserved energy near the ground.

Figure 3.1b provides information on monthly mean absolute humidity from June 2016 to July 2017. In summer the water vapor is mostly concentrated in the lowest 1.5 km with the highest monthly mean values of up to 6 g m^{-3} in July 2016 and July 2017. The water vapor in this altitude range is thus the main contributor to the integrated water vapor (IWV). In winter, the monthly mean absolute humidity is much lower with a minimum value of ~1.5 g m^{-3} (January) in the lowest 1.5 km.

In terms of relative humidity with respect to water (RH$_w$, Fig.3.1c), it can be seen that the monthly mean RH$_w$ is highest in the lowest 2 km of the atmosphere. This is in agreement with Maturilli and Kayser (2016). There is no strong seasonal variability of the monthly mean RH$_w$ at altitudes higher than 4 km. In the lower troposphere, the monthly mean RH$_w$, following the temperature cycle, is higher in summer and autumn (ranging from 60 to 94% in the lowest 2 km) and lower in winter and spring (ranging from 52 to 81% in the lowest 2 km), except for March 2017. In March 2017, the coldest month in the period of this study, the monthly mean absolute humidity was relatively low (1.7 g m^{-3}) in the lowest 1.5 km while monthly mean RH$_w$ was up to 85% (Fig.3.1c). In summer and autumn months high values of monthly mean RH$_w$ occur from the surface to 1.7 km. In winter and spring, the atmospheric layer near the surface is drier and high values of RH$_w$ appear from 0.3 to 1.5 km.

In order to determine if and in which way the thermodynamic properties were special for the study period monthly mean tropospheric temperature anomalies are presented in Fig. 3.2a. These anomalies have been calculated with respect to the previous 23 years (1993-2015). Figure 3.2a shows that, compared to the long-term
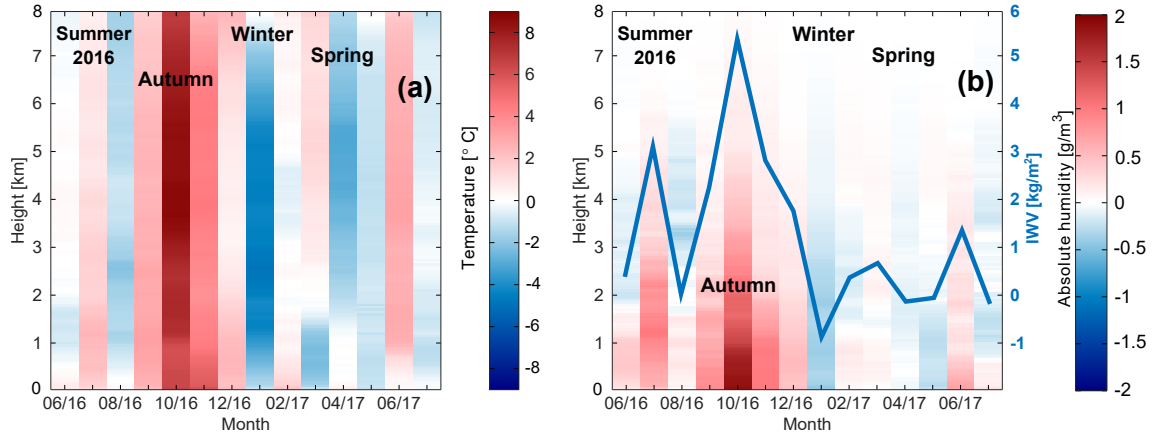
Figure 3.2: Anomalies of monthly mean atmospheric temperature (a) and absolute humidity (b) from radiosonde observations at Ny-Ålesund from June 2016 to July 2017. Anomalies are calculated with respect to the monthly mean values of the previous 23 years (1993-2015). The blue line corresponds to the IWV anomaly for the same time period. (published in Nomokonova et al. (2019b))

mean, temperatures are higher for some particular summer months. For example, July 2016 and June 2017 were warmer throughout the whole troposphere with maximum temperature anomalies of up to 2° and 4°C, respectively. Winter months were slightly warmer, too: the difference in atmospheric temperature was up to 2°C in December 2016 and February 2017. January 2017 was much colder with a temperature difference of down to -5°C. In comparison to the previous 23 years, atmospheric temperatures in March 2017 were higher in the upper troposphere (up to 2°C) and lower (-2°C) in the lowest 1.5 km. The largest positive temperature difference was found for autumn 2016, especially for October 2016 with maximum temperature differences of up to +8°C. Johansson et al. (2017) have already shown that moisture intrusions from the North Atlantic can cause significant local warming in some regions of the Arctic that can reach up to 8 °C. In addition, Overland et al. (2017) analyzed the variability of the near-surface air temperature (at 925 mb level) in the Arctic for the period from October 2016 to September 2017. The authors reported that there was an extreme temperature anomaly exceeding 5°C in the autumn 2016 that is in agreement with the results of the present study. Moreover, the authors showed that this extremely high temperature anomaly was associated with a persistent and unusual pattern in the geopotential height field that separated the polar vortex in the central Arctic into two parts. This situation lead to southerly winds which transported warm air into the Arctic from the mid-latitude Pacific and Atlantic oceans (Overland et al., 2017).

The observed anomalies in the monthly mean absolute humidity and IWV (Fig. 3.2b) in principle follow the sign of the discussed temperature anomalies. Fig.3.2b shows a correlation between the temperature and IWV increase. For instance, months that have a positive temperature difference also have an increase in the absolute humidity and IWV. Negative temperature differences correspond to decreases in the absolute humidity. For example, January 2017 was particularly colder and drier with anomalies in absolute humidity and IWV of $\sim$-0.5 g m^{-3} and $\sim$-0.8 kg m^{-2},
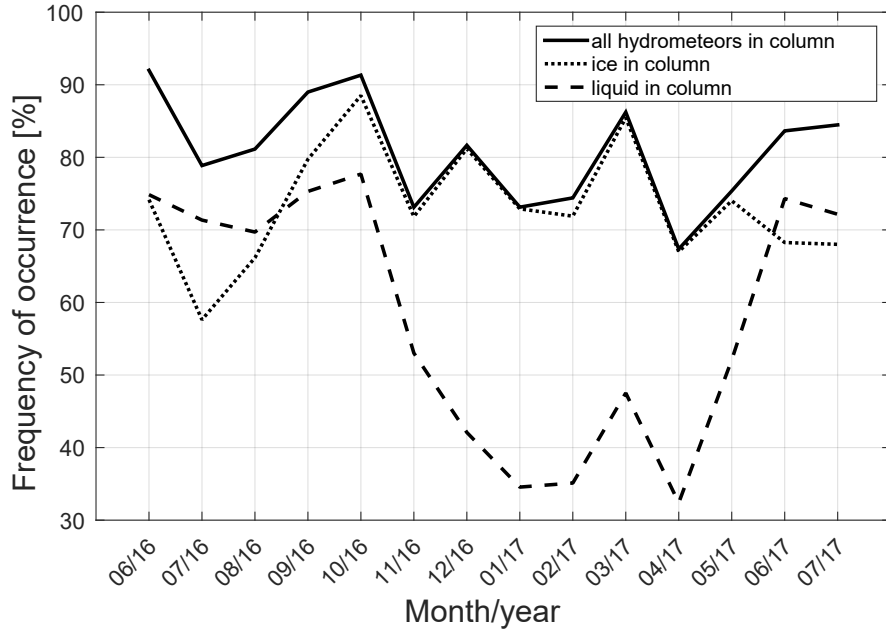
Figure 3.3: Frequency of occurrence of profiles with ice, liquid and any kind of hydrometeors. The frequency is given in % and normalized to the total number of Cloudnet profiles for each month. (published in Nomokonova et al. (2019b))

respectively.

Higher IWV values in comparison with the previous years were observed in June 2016, autumn 2016, December 2016 and July 2017. The differences in IWV varied from 1 to 5 kg m^{-2} with largest contributions from the lowest 3 km. In October 2016, the absolute humidity anomaly was highest ($\sim$2 g m^{-3}) in the lowest 3 km. This led to a positive change in IWV of more than 5 kg m^{-2} in comparison with previous years.

Thus, it turns out that the period from June 2016 to July 2017 had specific features especially for some months. Maturilli and Kayser (2016) have shown that in general a significant warming of the atmospheric column at Ny-Ålesund is observed in January and February. The authors reported that this warming in winter is related to the higher frequency of large-scale flow from south-southeast and less from the north. However, in present study January 2017 was much colder in comparison to the previous years. In January 2017, and also in the other winter months, the wind direction occurred more frequently from south-southwest (not shown) in comparison with the earlier period from 1993 to 2014 with wind direction dominated from southeast. However, it is not clear yet what exactly caused the relatively cold January 2017.

3.2   Hydrometeor occurrence

From June 2016 to July 2017, cloudy profiles occur around 80% of the time (Fig.3.3). The frequency of cloud occurrence is largest in October 2016 and June 2016 ($\sim$92%) and lowest in April 2017 (68%). In order to have a closer look on which types of

hydrometeors occur in the atmospheric column, Fig. 3.3 also gives an overview of the frequency of occurrence of liquid and ice hydrometeors, separately.

For this statistics all the range bins in Cloudnet profiles for hydrometeor types were checked. If a Cloudnet bin contains cloud droplets, rain or drizzle, then it is counted as liquid. If ice particles have been detected in a range bin, then it was defined as ice. Note that Cloudnet does not distinguish between snow and cloud ice. Mixed-phase range bins are considered as both liquid and ice. Then profiles that contain at least one "liquid" ("ice") bin are counted as liquid (ice) containing. Profiles containing liquid and ice phases are counted in both classes.

Liquid hydrometeors (dashed black line in Fig.3.3) have the highest frequency of occurrence during summer and autumn (70-80%) and the lowest in winter ($\sim$36%). A pronounced seasonal variability is thus visible. Ice (densely dashed black line in Fig.3.3) occurs more often in autumn, winter and early spring with the frequency of occurrence varying from 72 to 88%. In summer ice occurs typically around 58-78% of the time. The frequency of ice occurrence does not show a clear seasonal variability as the liquid phase.

Figure 3.4 shows vertical distributions of hydrometeors. For these statistics the above-mentioned bin classification was used. The frequency of occurrence at a certain altitude was normalized to the total number of Cloudnet profiles in a corresponding month. The highest frequency of occurrence was 60 and 70% in March 2017 and October 2016, respectively (Fig.3.4a, left panel). The lowest frequency of occurrence was in July 2016 (<30%) while for the other months in summer 2016 the frequency of occurrence of all hydrometeors was around 60%. In January 2017 the occurrence of clouds above 3 km was less than 10% which correlates with low RH_w (Fig. 3.1c) at these altitudes and the lowest value of IWV (Fig. 3.2b).

The total vertical distribution (Fig. 3.4, right panel, solid black line) shows that hydrometeors occur predominantly in the lowest 2 km with the maximum frequency of occurrence of $\sim$53% at the height of 660 m. Above 2 km, the frequency of occurrence is less than 30% and monotonically decreases with height. In terms of seasons, the vertical frequency of occurrence of all hydrometeors reveals variations of the maximum within $\pm$10% with highest values of frequency of occurrence in autumn 2016 of more than 60% ($\sim$1 km height). In summer 2016, the hydrometeor frequency of occurrence is in general higher than in summer 2017 indicating a pronounced year-to-year variability which will be analyzed in future when multi-year datasets will be available.

Liquid hydrometeors (Fig. 3.4b) occur most of the time in the lowest 2 km. Above 2 km, the frequency of occurrence of liquid is less than 5% and above 3 km almost no liquid particles are observed. The frequency of occurrence of liquid has a maximum at around 0.7-0.9 km height. Largest values of liquid phase occurrence vary from 40% to 50% in summer and autumn 2016. The maximum frequency of occurrence in the winter months does not exceed 15%. A strong seasonal variability of liquid, with high values in summer (32%) and lowest values in winter (12%) can be seen.
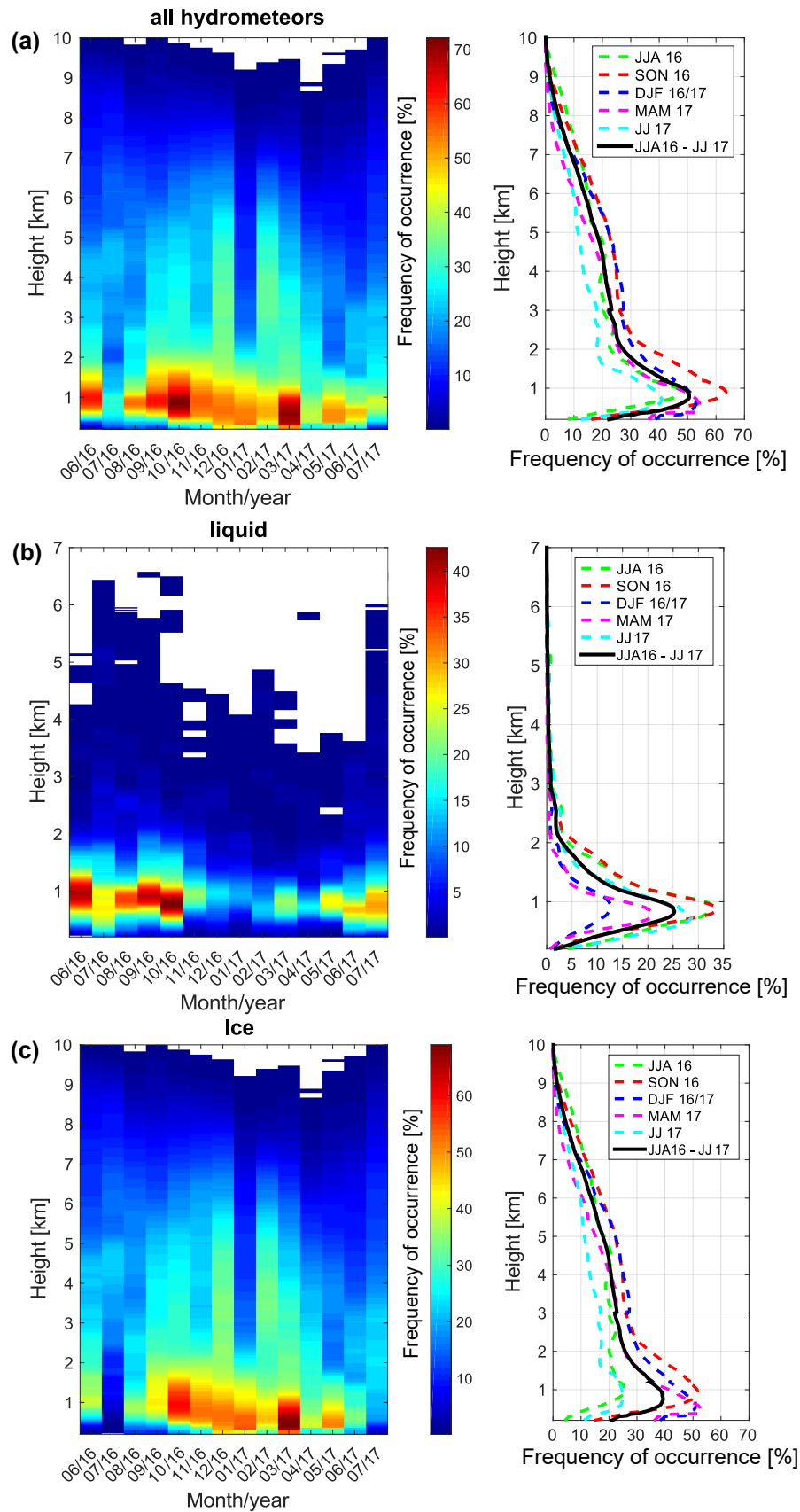
Figure 3.4: Monthly, seasonal and total (for the whole time period) frequency of occurrence of all hydrometeors (a), liquid (b) and ice (c) as a function of height for the period from June 2016 to August 2017. Frequency of occurrence is given in % and normalized to the total number of Cloudnet profiles for each month. (published in Nomokonova et al. (2019b))

The vertical occurrence of ice hydrometeors is shown in Fig.3.4c. Ice is mostly present at altitudes below 2 km. On average the frequency of occurrence peaks at around 700 m with values of 40%. In contrast to the ice occurrence anywhere in a column (Fig. 3.3), which is not showing a strong seasonal variability, the vertical distribution of ice phase shows a pronounced seasonal cycle, in particular in the lowest 2 km. For higher altitudes, the seasonal variability is less pronounced. Above 2 km, the frequency of occurrence of ice decreases from ∼30% to less than 10% at 8 km.

Similar to liquid hydrometeors, the frequency of occurrence of ice is highest in the lowest 2 km with values of 60 and 70% in October 2016 and March 2017, respectively (Fig.3.4c, left panel). The lowest ice frequency of occurrence is found for the summer months. In July 2016, which is the warmest month during the observation period, the freezing level often reached altitudes up to 2 km and therefore almost no ice was observed below this height. In January 2017 ice rarely occurred at heights larger than 4 km, which was probably caused by presence of dry air. In the right panel of Fig.3.4c it can be seen that the highest frequency of occurrence of ice phase is in the lowest 2 km and around 52% in autumn, winter and spring.

3.3   Statistics on different types of clouds

In addition to the occurrence of hydrometeor types, a classification of clouds into single-layer and multi-layer was also made. Single-layer clouds were furthermore separated into liquid, ice and mixed-phase.

For the classification every Cloudnet profile was checked from the top to the bottom for cloud layers. A cloud is defined here as a layer of at least three consecutive cloudy height bins. Based on a number of identified cloud layers single-layer and multi-layer clouds were classified. Cases were considered as multi-layer if two or more cloud layers were separated by one or more clear-sky height bins. Figure 3.5 gives an overview of the cloud type occurrence at Ny-Ålesund for the whole period of this study. The total occurrence for the whole period (right-most bar) shows 44.8% (506,253 profiles) of multi-layer and 36% (406,810 profiles) of single-layer clouds. Among single-layer clouds the most frequent type was mixed-phase, followed by ice and liquid single-layer clouds with the cloud occurrence of 20.6, 9.0 and 6.4%, respectively. Note that clouds were considered as mixed-phase if ice and liquid phases were both present in the same cloud boundaries regardless whether liquid and ice were in the same range bin or not. This implies that mixed-phase clouds include not only cases with liquid cloud top and ice below but also cases when both phases (ice and liquid) are present anywhere within the detected cloud layer.

Figure 3.5 also shows the monthly occurrence of different cloud types. The monthly cloud occurrence, i.e. the sum of all different cloud types, corresponds to the frequency of occurrence of all hydrometeors shown by a solid black line in Fig. 3.3. As seen for liquid and ice hydrometeors (Fig. 3.3), the occurrence of single-layer liquid and ice clouds also has a seasonal and monthly variability. About 15% of single-layer liquid clouds were detected in summer but less than 2% in other seasons. The occurrence of single-layer ice clouds was 15-20% in winter and spring and less than 5% in other months. Single-layer mixed-phase clouds and multilayer-clouds were
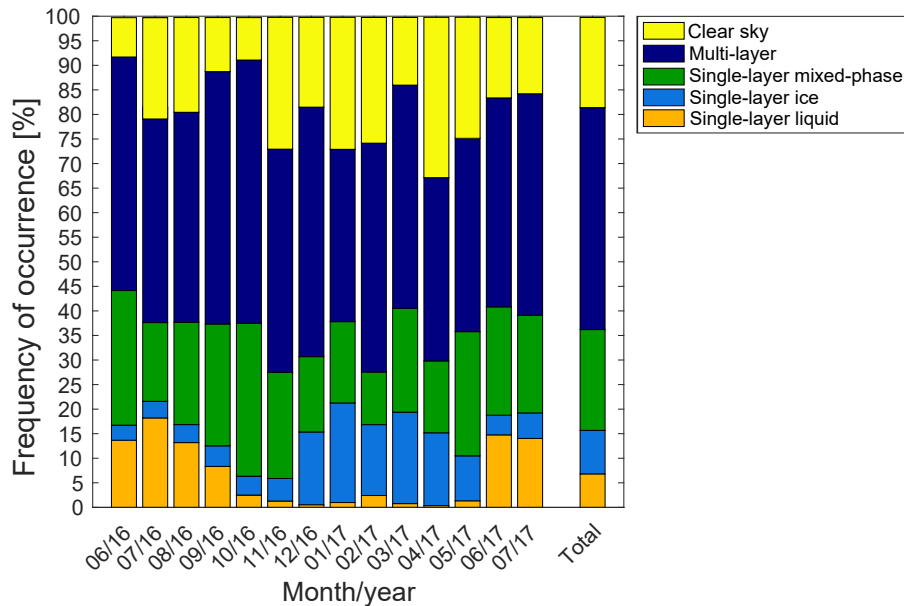
Figure 3.5: Monthly frequency of occurrence of different types of single-layer clouds (liquid, ice and mixed-phase), multi-layer clouds and clear sky profiles for the period from June 2016 to July 2017. Last right column showing the total frequency of occurrence. (published in Nomokonova et al. (2019b))

present most of the time with typical values of frequency of occurrence of around 20% and 45%, respectively. Thus, during most of the time, cloud systems had a complicated structure and/or consisted of both phases, liquid and ice, indicating that they are related to complex microphysical processes. In turn, the observational capabilities of these types of clouds are limited. In situations with multiple liquid layers, whether warm or mixed-phase, partitioning the observed LWP from HATPRO among these different layers is particularly challenging and results in larger uncertainties (Shupe et al., 2015). A multi-layer cloud classification requires a reliable profiling of liquid layers, which is limited by significant attenuation of lidar signals in the first liquid layer. Radar signals have better propagation through the whole vertical cloud structure in comparison with a lidar. However, the radar reflectivity is often dominated by the scattering from relatively large particles which mask the presence of small particles, like liquid droplets, being present in the same volume. In the case of multi-layer mixed-phase clouds, liquid phase can thus not be reliably detected based on radar reflectivity alone.

3.4 Single-layer clouds and their relation to thermodynamic conditions

Taking into account the above-mentioned limitations of multi-layer cloud observations the further analysis is concentrated only on single-layer cases. For the following analysis of single-layer clouds LWP from HATPRO and the Cloudnet IWC product was also used. Cases when this information was not available were excluded. In
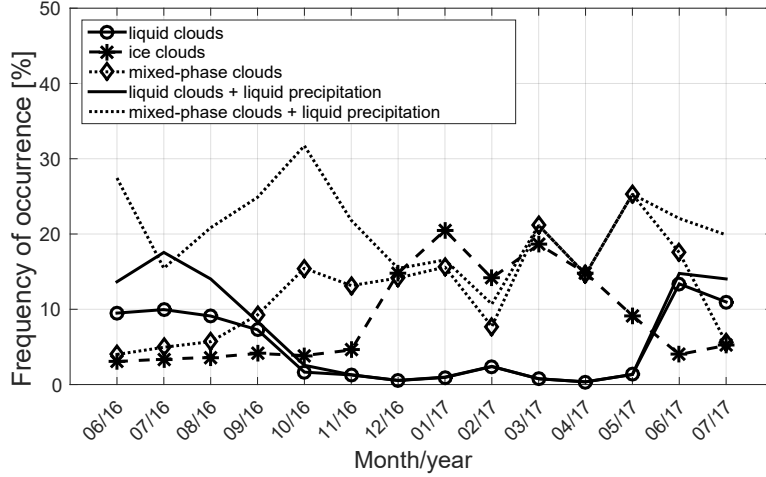
Figure 3.6: Frequency of occurrence of ice-only, liquid-only, mixed-phase single-layer clouds based on Cloudnet categorization data (for lines with circles, diamonds and stars profiles with liquid precipitation are not included). The frequency is given in % and normalized to the total number of Cloudnet profiles in each month. (published in Nomokonova et al. (2019b))

particular, profiles with the presence of liquid precipitation and flagged data due to wet HATPRO radome were removed. The resulting dataset (Fig. 3.6, lines with circles, stars and diamonds) was thus reduced to 149,960 profiles (37% of all single-layer profiles) with 65,299 profiles (16%) for single-layer mixed-phase clouds, 59,364 profiles (15%) for single-layer ice clouds and 25,297 profiles (6%) for single-layer liquid clouds only. Thus, all results are relevant for single-layer clouds without liquid precipitation. Nevertheless, with this subset of single-layer clouds the monthly variability can be still captured and thus the assumption is made that it is still representative for all single-layer cloud cases.

Comparison of Fig. 3.6 and Fig. 3.5 shows that the occurrence variability of liquid and ice single-layer clouds is similar. Occurrence of mixed-phase clouds differs because of the exclusion of liquid precipitation clouds which often contain ice phase and melting layer and thus considered as mixed-phase. This is in agreement with Mülmenstädt et al. (2015) who reported that most of the liquid precipitation is formed including the ice phase. The maximum and minimum occurrence of single-layer mixed-phase clouds of 25% and 4% were observed in May 2017 and June 2016 respectively. The annual-averaged top-height of single-layer mixed-phase clouds was 2 km (not shown). The findings of the present study are in a good agreement with space-borne radar-lidar observations of clouds in the Svalbard region in the period from 2007 to 2010 (Mioche et al., 2015). The authors showed that single-layer mixed-phase clouds in the Svalbard region mostly occur in May.

The geometrical thickness of the single-layer clouds is shown in Fig.3.7a. The geometrical thickness of a cloud is calculated as the distance between the upper border of the uppermost cloud range bin and the lower border of the lowermost cloud range bin. The thickness of single-layer liquid clouds varies between 60 to 2200 m with mean and median values of 280 and 240 m, respectively. Less than 1% of observed single-layer liquid clouds have a thickness larger than 800 m.
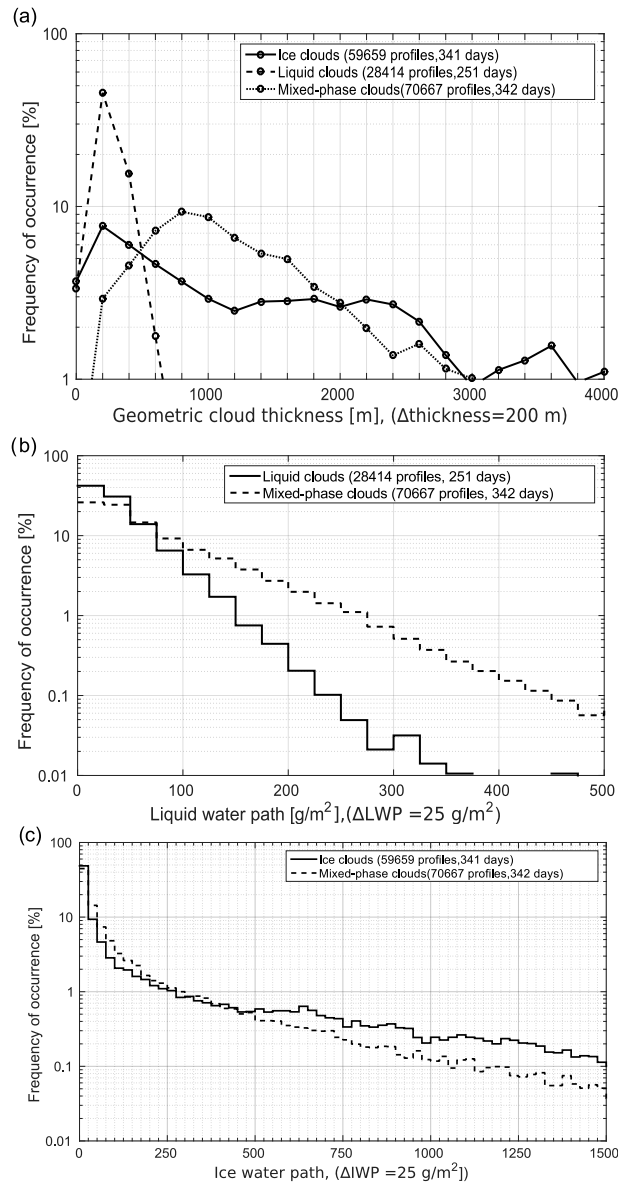
Figure 3.7: Frequency of occurrence of cloud thickness for single-layer clouds (a), of LWP for single-layer liquid and mixed-phase clouds (b) and of IWP for single-layer ice and mixed-phase clouds (c) for the period from June 2016 to July 2017. The y-axis is shown in logarithmic scale. In the x-axes Δ shows the bin width. The frequency of occurrence is normalized by the total number of corresponding cloud type. (published in Nomokonova et al. (2019b))

In contrast, single-layer mixed-phase clouds typically have a larger geometrical cloud thickness which varies from 100 to 8500 m with the median and mean values of 1100 and 1500 m, respectively. In comparison with mixed-phase single-layer clouds, the geometrical cloud thickness distribution for single-layer ice clouds is broader ranging from 60 to 9500 m. The median and mean values of the geometrical cloud thickness for single-layer ice clouds are 1500 and 2100 m, respectively. The mode of the thickness distribution of single-layer ice clouds correspond to 800 m. Less than 1% of single-layer mixed-phase and ice clouds have a geometrical cloud thickness larger than 3 and 4.2 km, respectively.

The frequency of LWP occurrence for liquid and mixed-phase clouds is shown in Fig. 3.7b. Both types of clouds are characterized by relatively low values of LWP. The median values of LWP for single-layer liquid and mixed-phase clouds are 17 and 37 g m^{-2}, and mean values are 30 and 66 g m^{-2}, respectively. More than 90% of single-layer liquid and mixed-phase clouds have LWP values lower than 100 and 200 g m^{-2}, respectively. It has to be noted that in particular in these LWP ranges, the relative uncertainty in the retrieved LWP is quite large (see Sec. 2.2). Larger LWP values in mixed-phase clouds might be related to their larger geometrical thickness (Fig. 3.7a).

Median values of IWP for single-layer ice and mixed-phase clouds are 14.6 and 21.4 g m^{-2}, and mean values are 273 and 164 g m^{-2}, respectively (Fig. 3.7c). IWP values exceeding 400 g m^{-2} are more frequent in single-layer ice clouds than in single-layer mixed-phase clouds. However, for both cloud types the occurrence of IWP values higher than 125 g m^{-2} is less than 3%.

A number of studies comparing observed and modeled LWP and IWP values for Arctic regions have revealed the challenge for NWP models to accurately simulate LWP and IWP. Tjernström et al. (2008) evaluated 6 regional models which were set to a common domain over the western Arctic and found that one half of the models showed nearly 0 bias in LWP while another half underestimated LWP by ~20 g m^{-2}. The authors reported that some of the models showed -30 to 30 g m^{-2} biases in IWP. In addition a low correlation between the observations and modeled IWP and LWP was found. Most of the models showed too low variability of IWP. Karlsson and Svensson (2011) compared 9 global climate models in the Arctic region. The authors showed that mean and standard deviations of modeled IWP and LWP can vary by a factor of 2. Forbes and Ahlgrimm (2014) concluded that such discrepancies may be related to an insufficient representation of microphysical processes. Authors note that one of the major challenges are phase partitioning and a parameterization of cloud particle's formation and development.

Klein et al. (2009) compared 26 models with air-borne and ground-based observations over the north Alaska (Barrow and Oliktok Point). The authors found that although many models showed an LWP exceeding IWP (as observed), simulated LWP values were significantly underestimated. Since climate and NWP models typically parameterize cloud phase as a function of temperature, relations between temperature and the phase partitioning for mixed-phase clouds at Ny-Ålesund were analyzed. Figure 3.8 shows the probability of liquid fraction, i.e. (LWP/(LWP+IWP)), in mixed-phase clouds for different cloud top temperature ranges based on the Ny-Ålesund radiosonde observations. In general, the liquid fraction increases with cloud top temperature. Thus, high liquid fraction values in single-layer mixed-phase clouds are found at cloud top temperatures ranging from -15° to 0°C. The occurrence of the liquid fraction of 0.4-0.6, implying that both phases are roughly equally present, is relatively high for cloud temperature ranges between -25° and -15°C but is rare for cloud top temperatures below -25°C. Almost no liquid was observed at the cloud top temperatures below -40°C. Non-zero liquid fraction below -40°C is mostly associated with thick clouds having a high cloud tops with a liquid layers detected at lower altitudes.

In-cloud atmospheric temperature and humidity are important for NWP models as these parameters determine the cloud particle's formation and development. For
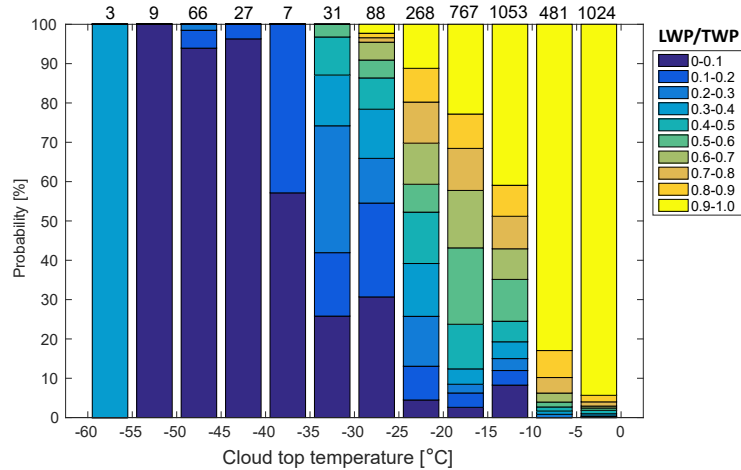
Figure 3.8: The relative probabilities of different ranges of the liquid fraction LWP/TWP given at various cloud top temperatures of single-layer mixed-phase clouds. The probability is normalized by the total number of profiles for each cloud top temperature range. Numbers at the top of plot show the number of cases included in the temperature range. The total number of all profiles is 3824. (published in Nomokonova et al. (2019b))

instance, laboratory studies show that shapes of ice crystals are defined by the environment temperature and humidity (Fukuta and Takahashi, 1999; Bailey and Hallett, 2009). There is also some evidence that similar effects happen in the real atmosphere (Hogan et al., 2002, 2003; Myagkov et al., 2016). Aggregation efficiency and deposition growth rate are also temperature and humidity dependent (Hosler and Hallgren, 1960; Bailey and Hallett, 2004; Connolly et al., 2012). Therefore, in this study different cloud types were also related to environmental conditions under which they occur. The frequency of occurrence of the different hydrometeors in single-layer clouds as a function of in-cloud temperature and relative humidity observed at Ny-Ålesund is shown in Fig.3.9 (a-d). Here, temperature and relative humidity were determined for each cloud bin between cloud boundaries. For this analysis only single-layer-cloud profiles observed one hour before and after a radiosonde launch were included. The atmospheric conditions were assumed not change too much within this time period. For temperatures lower than 0°C the relative humidity with respect to ice (RHi) was used. Values of RHw were used at temperatures exceeding 0°C. For the cloud classification the method specified in Sec. 3.3 was used.

All single-layer clouds were observed in the temperature range from -60° to +10°C (Fig. 3.9a). In some cases single-layer clouds appeared at low RHi and RHw (Fig. 3.9 a-d) that might be associated with hydrometeors falling from saturated to subsaturated atmospheric layers. Another reason could be that the radiosondes, which drift, do not provide representative information for the sampling volume of the zenith-pointing ground-based instruments. However, cases with very low relative humidity values occurred in less than 1% of the analyzed observations. According to Mc-Grath et al. (2006) the uncertainties in temperature due to the radiosonde drifts in the northern hemisphere do not exceed 0.4°C up to 10 km altitude. Uncertainties in relative humidity are about 3%.
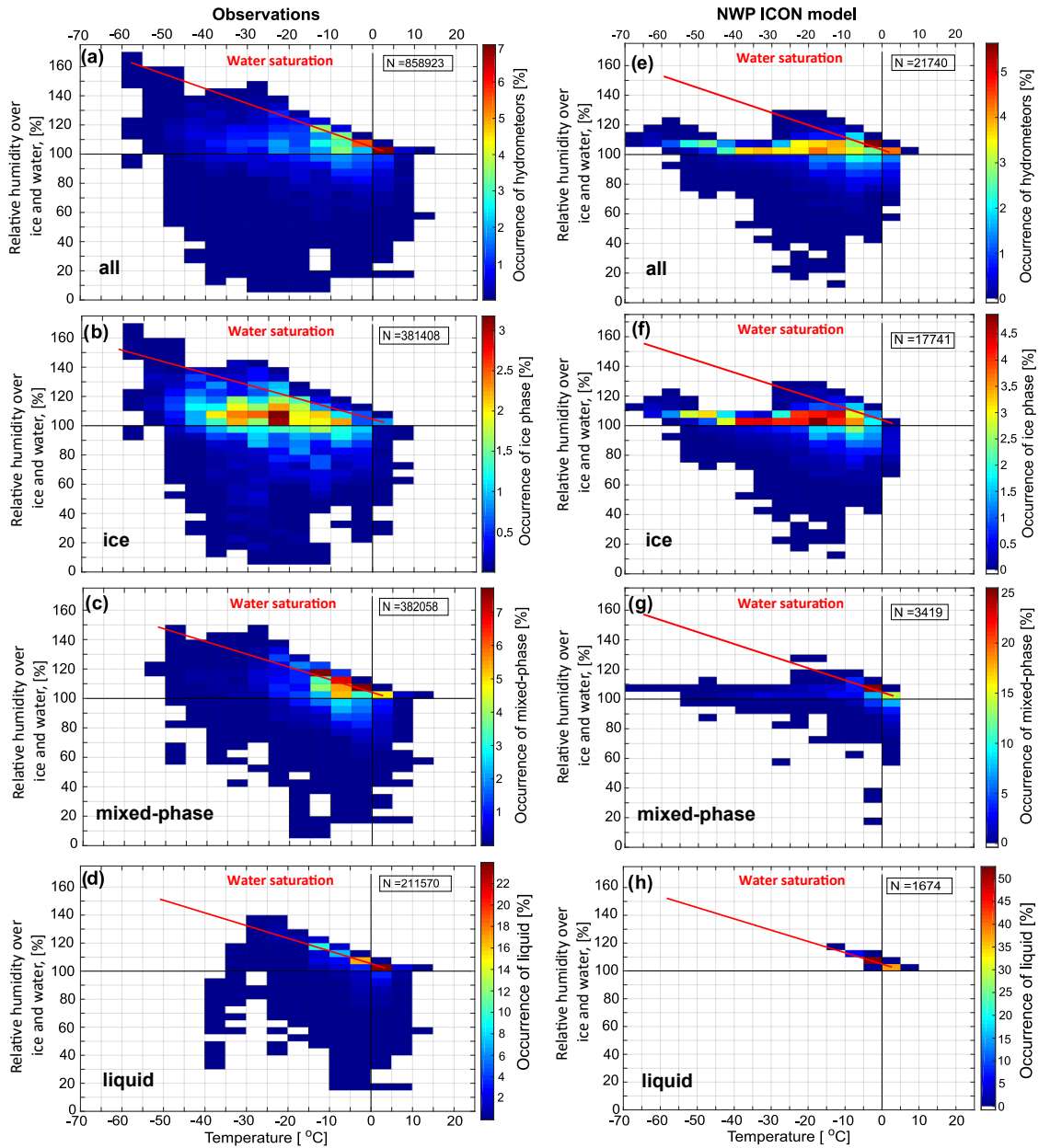
Figure 3.9: Two-dimensional histograms of in-cloud atmospheric temperature and relative humidity for all clouds (a,e), ice clouds (b,f), mixed-phase clouds (c,g). For a, c, e and g ice and/or liquid phases are present. For b and f only ice phase is present. Liquid phase of liquid-containing clouds is shown in d and h. Only cases of single-layer clouds are included and shown for observations (left) and for column output of NWP model ICON over Ny-Ålesund (right). Frequency of occurrence is normalized by the total number of bins of the correspondent single-layer clouds detected between the period of one hour before and after radiosonde launch. (published in Nomokonova et al. (2019b))

Figure 3.9b shows that ice clouds mostly occur in the temperature range from -45° to -5°C including the temperature range (<-38 °C) of homogeneous nucleation. The highest occurrence of ice was observed in the temperature range from -25° to -20°C and under conditions that are subsaturated with respect to water but saturated with

respect to ice (Fig.3.9b). Observed ice particles mostly occur at RHis between 100 and 125%. Presence of ice at positive temperatures might be related to cases of cloud type misclassification, for example, when a cloud was identified as ice instead of mixed-phase. These cases might be also associated to uncertainties in the model temperature profile used in the classification algorithm.

Mixed-phase clouds were observed at supersaturation with respect to ice (Fig.3.9c). Most of the cases were located at the water saturation line. Frequently, mixed phase occurs at temperatures from -25° to +5°C with two maxima in the range of -15° to 0°C. The temperatures of -15° and -5°C correspond to the highest efficiency of deposition growth of ice crystals at water saturation levels (Fukuta and Takahashi, 1999).

Liquid phase mostly occurs near water saturation at temperatures from -15° to +5 °C (Fig.3.9d). Supercooled liquid was observed at temperatures down to -40°C. The lowest temperature limit for liquid clouds only was -30°C (not shown).

3.5   Application for model evaluation

This observational cloud data set can provide useful information for a model evaluation. As an example, this section presents a comparison of the NWP model ICON with the observations at Ny-Ålesund. Note that the intention here is not to perform a thorough model evaluation but to show the potential of such a dataset to test, for example, if the dependence of the occurrence of clouds on the thermodynamic conditions can be represented by the model.

The statistics on different types of clouds, their phases and the relation to atmospheric conditions provide a useful dataset for a comparison with similar statistics based on the model output. The identification of clouds in the model was based on a 10^{-7} kg kg^{-1} threshold in specific cloud water content, specific cloud ice content, rain mixing ratio and snow mixing ratio. And the classification of clouds were performed using the same procedure as for the observations (see Sec. 3.3). The value of the threshold in the hydrometeor contents was found empirically: the usage of a lower threshold leads to the higher occurrence of ice clouds in the ICON model which were not identified in observations. For a higher threshold less ice clouds were present in the ICON model than in observations. According to the Z-IWC-T relation from Hogan et al. (2006), the chosen threshold in the ice mixing ratio corresponds to the radar reflectivity factor ranging from -55 to -32 dBZ at temperatures from -60° to -5°C. In general, these values are close to the radar sensitivity, although at high altitudes the radar sensitivity is about -40 dBZ (Küchler et al., 2017). Nevertheless, most of the observed hydrometeors are located within 2 km from the surface (see Sec. 3.2) and, therefore, the lack of sensitivity at high altitudes does not significantly affect the results. For more detailed analysis of the uncertainties due to differences between the instrument and the model sensitivity can be done using observation simulators (e.g. Haynes et al., 2007). Such the analysis is out of the scope of the current study and thus not investigated in the present study.

Right panels in Fig. 3.9 show the frequency of occurrence of different hydrometeors in single-layer clouds as a function of in-cloud temperature and RHw based on the

ICON model data. Figure 3.9e shows that modeled single-layer clouds occur within the temperature range similar to the temperatures observed in clouds at Ny-Ålesund (Fig. 3.9a). Figure 3.9f indicates that ice clouds in the ICON model typically exist at temperatures from -65° to -5°C. Both, the ICON model and observations, reveal that ice particles typically occur at relative humidities higher than the saturation over ice but lower than the saturation over water. The high occurrence of ice phase in ICON is found at RHi up to 110%, while for the observations reveal RHi of up to 125% (Fig. 3.9b). The presence of ice particles at lower supersaturation over ice in the ICON model in comparison with observations may be associated with ice nuclei (IN) parameterization in the ICON model, which is known to be still a challenge (Fu and Xue, 2017). It might be associated with a higher concentration of IN and, thus ice particles, leads to faster deposition of water vapor onto the ice particle's surface. Therefore, a more efficient vapor-to-ice transition in the model could lead to lower relative humidity. Similarly, the parameterization of deposition growth rate and secondary ice processes may also have an impact on the in-cloud relative humidity.

Mixed-phase clouds in the ICON model appear near the water saturation (Fig. 3.9g) that is consistent with the observations (Fig. 3.9c). The model mostly produces mixed-phase clouds within the temperatures range from -10° to +5°C, that is narrower in comparison to the observations.

Modelled liquid phase occurs near water saturation at temperatures from -15° to +5°C (Fig.3.9h), which is in a good agreement with observations. In the ICON model the occurrence of liquid phase at temperatures below -5°C is only 6%, while in the observations this occurrence is more than 30%.

Figure 3.10 summarizes temperature dependencies of hydrometeor occurrences in the ICON model and in observations. The temperature distributions of single-layer liquid clouds (solid red lines, Fig. 3.10) are narrow (-10° to +5°C) for both, model and observations, although, the observed distribution has larger values of occurrence. The total distributions of the liquid phase (dashed red lines, Fig. 3.10) are different. The observed distribution has larger and occupies a wider temperature range (-25° to +10°C). In the model, most of the liquid phase is concentrated in the temperature range from -10° to +5°C. This difference leads to a divergence between mixed-phase cloud occurrences (solid green lines, Fig. 3.10): the observed frequency distribution for mixed-phase clouds shows a broader temperature range than the model. Sandvik et al. (2007); Cesana et al. (2012) showed a similar difference between observed and modelled single-layer mixed-phase clouds. For the modelling the polar version of the nonhydrostatic mesoscale model from the National Center for Atmospheric Research was used by Sandvik et al. (2007). The authors found that for temperatures below -18° the liquid fraction in single-layer mixed-clouds was completely absent in simulations.

Ice cloud observations (solid blue line in Fig. 3.10a) show a broad temperature range from -60° to +5°C. In comparison to the observations, the model (solid blue line in Fig. 3.10b) shows a broader temperature range for single-layer ice clouds (-70° to +5°C). Due to the low occurrence of the liquid phase at temperatures below -5°C by the model most of the clouds at lower temperatures are classified as pure ice. Therefore, the model shows significantly larger occurrence of ice clouds at temperatures warmer than -20°C. Also this explains similarities between modelled ice phase in pure ice and ice-containing clouds (dashed blue line). In addition, the occurrence
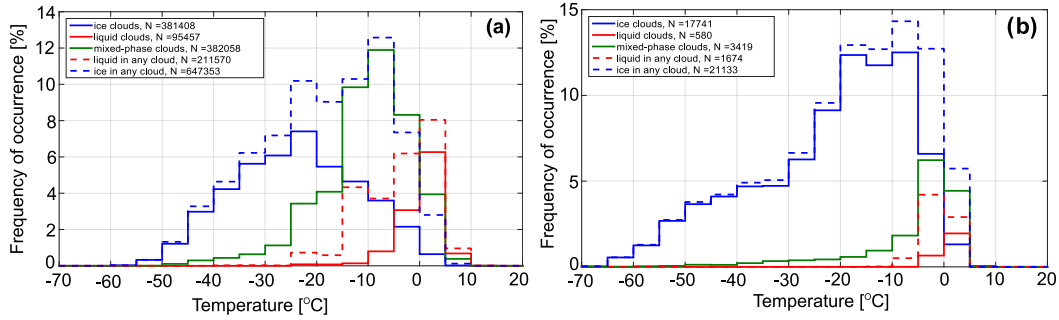
Figure 3.10: Distribution of in-cloud atmospheric temperature for different types of single-layer clouds, liquid and ice phase for observations (a) and NWP ICON model over Ny-Ålesund (b). (published in Nomokonova et al. (2019b))

of simulated ice clouds is higher at temperatures below -40°, which corresponds to the homogeneous ice nucleation regime. Similar results were obtained by Cesana et al. (2012), who compared the hydrometeor classification product from CALIPSO observations and the climate model LMDZ5B (Hourdin et al., 2013) and found that the model tends to overestimate occurrence of ice phase in the temperature range from –50 to –10°C.

3.6   Summary and conclusions

For the first time, clouds at Ny-Ålesund, Svalbard were statistically analyzed and related to the thermodynamic conditions under which they occur. An almost 14-month long measurement period at Ny-Ålesund was analyzed and have been presented statistics on vertically resolved cloud properties, hydrometeors and thermodynamic conditions. The Cloudnet classification scheme, based on observations from a set of ground-based remote-sensing instruments (active and passive), was applied in order to provide vertical profiles of clouds, their macrophysical, microphysical properties and phase. In total 1,130,030 Cloudnet profiles (216,860 clear sky profiles and 913,170 cloudy profiles) are available for the period from June 2016 to July 2017.

The statistics on cloud properties and atmospheric thermodynamic conditions is essential for a better understanding of cloud processes and can also be used for model evaluation. In this study, the relation between cloud properties and thermodynamic conditions from observations was compared to results from the NWP ICON model.

The thermodynamic conditions were derived from radiosonde data for the period from June 2016 to July 2017 and were compared with previous 23 years. This comparison revealed that the analyzed period presented in this chapter differs from the previous years. January 2017 was significantly colder with temperature differences down to -5°C while October 2016 was extremely warm with temperature anomalies of more than +5°C. Also, in comparison to the previous 23 years, IWV was lower in January 2017 by 1 kg m^{-2} and more than 5 kg m^{-2} higher in October 2016.

The total occurrence of clouds is ∼81%. The highest frequency of occurrence is in October 2016 (92%). Similar results of high cloud occurrence in summer and

autumn at Ny-Ålesund based on micro-pulse lidar measurements were previously found by Shupe et al. (2011). Nevertheless, the observed total occurrence of clouds at Ny-Ålesund for the investigated period is higher than the one from Shupe et al. (2011). The authors showed that the total annual cloud fraction at Ny-Ålesund for the period from March 2002 to May 2009 was 61%. On the one hand, a different time period was analyzed in this study. On the other hand, the occurrence of clouds in Shupe et al. (2011) might be underestimated when only a lidar is used (Bühl et al., 2013). However, our results are in a good agreement with a previous study by Mioche et al. (2015). The authors used space-borne observations over the Svalbard region for the period from 2007 to 2010. They applied the DARDAR algorithm (Delanoe and Hogan, 2008, 2010) that utilizes measurements from CALIPSO and CLOUDSAT. They showed that the cloud occurrence over the Svalbard region was in the range from 70% to 90% having peaks in spring and autumn. Mioche et al. (2015) found the lowest cloud occurrence in July, while the statistics in the present study reveal the high cloud occurrence (∼80%) in this month. Also here, this difference might be related to the different periods investigated. Another reason might be that the observed clouds in July are predominantly located at heights below 1.5 km. These low-level clouds are difficult to capture by CloudSat due to its "blind zone" in the lowest 1.2 km (Marchand et al., 2008; Maahn et al., 2014). Mioche et al. (2015), for example, showed that the Ny-Ålesund ground-based measurements revealed the highest cloud occurrence in summer (between 60% and 80%), while satellite observations showed the minimum in that season. The lowest cloud occurrence in the study by Shupe et al. (2011) is around 50% in March. In present study, the lowest cloud occurrence (∼65%) was also observed in spring. This might be associated with a relatively low atmospheric temperature and less moisture being available in the atmosphere. The increase of cloudiness in summer and autumn is probably due to higher values of relative humidity at the site in comparison with other seasons. Also sea-ice coverage might impact the cloud occurrence. As during summer and autumn sea ice coverage is the lowest, areas of open water are larger and therefore, that can lead to enhanced evaporation and latent heat exchange with the Arctic atmosphere.

The most predominant type of clouds is multi-layer clouds with the frequency of occurrence of 44.8%. Single-layer clouds occur 36% of the time. The most common type of single-layer clouds is mixed-phase with a frequency of occurrence of 20.6%. The total occurrences of single-layer ice and liquid clouds are 9% and 6.4%, respectively. The cloud occurrence of single-layer liquid and ice clouds has a pronounced month-to-month and seasonal variability.

The analysis of 149,960 Cloudnet profiles with single-layer clouds only showed that single-layer liquid and mixed-phase clouds typically have very low values of LWP with median values of 17 and 37 g m^{-2} and mean values of 30 and 66 g m^{-2}, respectively. It has to be noted that these low values of LWP may significantly affect shortwave and longwave radiation (Turner et al., 2007). These clouds with LWP values between 30 and 60 g m^{-2} have the largest radiative contribution to the surface energy budget Bennartz et al. (2013). The LWP of single-layer mixed-phase clouds is larger than for single-layer liquid clouds. This result is in an agreement with a study by Shupe et al. (2006). The authors reported that the LWP for mixed-phase single-layer clouds is larger than for pure liquid clouds due to thicker liquid layers in mixed-phase clouds.

Turner et al. (2018) showed that in Barrow the occurrence of single-layer mixed-phase clouds is lower than the one of single-layer liquid only cloud at LWP values exceeding 120 g m^{-2}. At LWP values below 120 g m^{-2} liquid only clouds become dominant over mixed-phase clouds. The similar behavior was found for Ny-Ålesund and shown in this chapter but with the transition at 50 g m^{-2}.

The IWP statistics shows that in general single-layer ice clouds contain more ice than single-layer mixed phase clouds with corresponding mean values of 273 and 164 g m^{-2}, respectively. The median values of IWP for single-layer ice and mixed-phase clouds are 14.6 and 21.4 g m^{-2}, respectively. This difference might be related to the cloud geometrical thickness. On average single-layer ice clouds are thicker than mixed-phase clouds. Single-layer mixed-phase clouds have higher occurrence than ice clouds for IWP values ranging from 25 to 400 g m^{-2}. For IWP values exceeding 400 g m^{-2} ice clouds were more frequent than mixed-phase.

The statistics on LWP and IWP for single-layer clouds, provided in this chapter, show that most of the time single-layer clouds at Ny-Ålesund have very low LWP which is within the uncertainty range ($<$30 g m^{-2}). The retrievals of LWP can be improved by using the infrared and higher frequencies of the MWR (Löhnert and Crewell, 2003; Turner et al., 2007; Marke et al., 2016) in future studies. The information from the 89 GHz passive channel of the FMCW radar and 183, 233 and 340 GHz frequencies of LHUMPRO (low humidity profiler) of the University of Cologne can be used for reducing the uncertainty of LWP. In the present study, the vertical profiles of clouds were analyzed and their horizontal distribution was not taken into account. For the investigation of the spacial variability of the LWP at the Ny-Ålesund and the influence of ocean and orographic effect, the azimuth and elevation scans of HATPRO might be used in the future studies to extend the analysis.

The analysis of cloud phase shows that liquid is mostly present in the lowest 2 km with the highest occurrence in summer and autumn (especially, in October 2016) and lowest in winter. However, in winter the occurrence of liquid hydrometeors is still significant and reaches 12% at a height of 1 km. The occurrence of ice phase within the first 2 km is lowest in summer (22%) and highest in October 2016 and March 2017 with 60% and 70%, respectively. The largest frequency of occurrence of ice and liquid in October 2016 ($>$ 50%) is related to strong temperature and humidity anomalies in this month. According to Overland et al. (2017), the anomalies were associated with warm air transported into the Arctic from mid-latitudes, the Pacific and Atlantic oceans.

Since phase partitioning in NWP models depends on atmospheric conditions, relations between cloud top temperature and liquid fraction are analyzed for mixed-phase clouds. It was found that liquid is present at temperatures down to -40°C. The highest occurrence of liquid phase is at cloud top temperatures ranging from -15° to 0°C.

The occurrence of different cloud types at Ny-Ålesund was analyzed as a function of environment conditions. In addition to observations the ICON model output was used for these analyses. The results show that the temperature distribution of single-layer liquid clouds is narrow with temperatures typically ranging from -10° to +5°C. Similar results are also found for the ICON model. However, the distribution of the liquid phase for mixed-phase clouds is one of the major differences

between the model and observations. The observed distribution ranges from -25° to +10°C while in the ICON model liquid phase is concentrated in the temperature range from -10° to +5°C. This difference results in a significant divergence between observed and modelled single-layer ice and mixed-phase clouds. The observed single-layer mixed-phase clouds occur in a much wider temperature range (from -25° to +5°C) than in the ICON model (from -15° to +0°C). Such differences have been previously reported by Sandvik et al. (2007). The authors showed that models can completely miss single-layer mixed-phase clouds below -18°. Observed ice clouds occur at temperatures from -60° to +5°C while the model simulate ice clouds down to -70°C. The occurrence of modeled ice clouds is significantly larger than observed at temperatures warmer than -20°. Due to the lower occurrence of liquid phase in the model at temperatures below -5° modeled clouds are often classified as pure ice. Also the model shows the higher occurrence of ice clouds at temperatures below -40° where homogeneous ice nucleation takes place.

The results from the first year of observations presented in this chapter show the potential of the dataset which provides vertically resolved cloud information. The derived dataset of cloud classification and cloud microphysical properties can be used to test the representation of clouds and their dependency on temperature and humidity in models and therefore, for an evaluation of high-resolution models. The analyzed dataset is also useful for satellite validation and the cloud radiation interactions studies. In order to have, more robust statistics and also to account for year-to-year variability long-term observations at Ny-Ålesund are needed. Therefore, the measurements of cloud and thermodynamic profiles are still ongoing at Ny-Ålesund within the (AC)³ project.

Chapter 4

The influence of anomalous atmospheric conditions on clouds and cloud radiative effect at Ny-Ålesund

The previous chapter already showed that atmospheric conditions at Ny-Ålesund are highly variable. For example, increased and decreased values of atmospheric temperature and humidity were observed in October 2016 and January 2017, respectively. It was shown that these conditions were related to enhanced and suppressed cloud occurrence, respectively. One of the factor that influences thermodynamic conditions and defined their changes is the large scale circulation and air masses transport. Many studies relate the advection of moist and warm air from the mid-latitudes with Arctic climate change (Woods and Caballero, 2016; Graversen and Burtu, 2016; Johansson et al., 2017), while only a few are focused on cold intrusions (Kanno et al., 2019). However, extreme cold events exhibit a stronger change in occurrence than extreme warm events (Sillmann et al., 2013; Collins et al., 2013). Kanno et al. (2019) reported that the occurrence of extremely cold air masses in the Arctic have been reduced by about 80% over the past 60 years. The authors mention that even though the main driver of this reduction is radiative forcing associated with green house gases, the relations of the extreme cold air masses with other components of the Arctic climate, such as humidity and cloudiness, have to be explored. Most of the studies on the Arctic climate are focused on winter. Nevertheless, Mortin et al. (2016) and Hegyi and Taylor (2018) pointed out the importance of the representation of the atmospheric variability during the transition periods. Significant anomalies in temperature,water vapor, and cloud properties initiate the surface melt in spring, while in autumn these factors affect ice freeze-up. Maturilli et al. (2015) showed that at Ny-Ålesund the trend in the net radiation budget is highest in summer. Even though this trend does not directly translate into the surface temperature increase, the additional radiation income may affect some other feedback mechanisms in the Arctic. This chapter shows how thermodynamic conditions associated with the large scale circulation influence cloud appearance at Ny-Ålesund and what impact these phenomena have on the cloud radiative properties. The focus of this chapter is not only on moist periods in winter season, but covers moist, dry, warm, and cold anomalies in all seasons. Periods of decreased and increased IWV and temperature are related to cloud occurrence, their liquid and ice water paths, and SW,

LW, and net CRE. The definition of warm/cold and moist/dry anomalous periods further used in this thesis is introduced in Sec. 4.1. Sections 4.2–4.4 show how cloud properties change under anomalous conditions with respect to normal situations. In Sec. 4.5 a long-term radiosonde dataset is used in order to check the occurrence of moist and dry periods for trends over the last 25 years. The content of this chapter was published in Nomokonova et al. (2019a).

4.1 Identification of anomalous periods

In this study 6-hour periods with distinct values of temperature and IWV were analyzed. Throughout the study periods with decreased and increased values are denoted by "-" and "+" signs prior to a variable symbol, respectively (e.g. "+T" corresponds to periods with increased temperature), while typical values are indicated just by a variable symbol (e.g. "T").

In order to decide whether a period is associated with a particularly high (low) value of water vapor and temperature, a dataset of 6-hourly mean values of IWV and temperature at 1450 m from HATPRO for the period from 2011 to 2018 (this period is used as reference throughout the study) was used. The 1450 m HATPRO range bin was chosen to account for the large scale transport rather than local effects which are related to the orography around Ny-Ålesund (Maturilli and Kayser, 2016). This altitude is also the closest to the arrival height of the FLEXTRA backward trajectories. Since the atmospheric conditions vary throughout a year, the 10th and 90th percentiles of the temperature and IWV were calculated for each month using the reference dataset (Fig. 4.1). The percentiles of IWV and 1450 m temperature are used as thresholds for the event classification. If a 6h-period has a mean IWV value below the 10th or above the 90th percentile it is considered as dry ("-IWV") or moist ("+IWV"), respectively. Otherwise it is assumed that the value of water vapor of this period is normal ("IWV"). Similarly, "-T" and "+T" correspond to a period with an average 1450 m temperature below the 10th or above the 90th percentile, respectively. As many studies consider water vapor as a driver of changes in radiative properties of the Arctic atmosphere, IWV was used as an indicator of anomalous periods. Typical periods corresponding to the "IWV" class are further denoted as normal. An anomalous period is one with "-IWV" (dry anomaly) or "+IWV" (moist anomaly), regardless which temperature class the period has. In addition periods when the water vapor anomalies are supported by temperature anomalies, i.e. classes "-T -IWV" and "+T +IWV" were also analyzed.

Since the anomalies in temperature and IWV are often driven by certain weather patterns which are related to the transport of air masses coming from lower or higher latitudes (Maturilli and Kayser, 2016; Dahlke and Maturilli, 2017; Mewes and Jacobi, 2019; Wu, 2017), back trajectories were analyzed for all dry and moist anomalies. All 6-hourly periods were identified with an anomaly class within the analyzed period and related to the FLEXTRA back trajectory files with corresponding reaching time.

Figure 4.2 shows 6-day-trajectories with the end point in Ny-Ålesund for "-IWV" and "+IWV" anomalies in different seasons. 6-day trajectories are sufficient to capture the air transportation to the Arctic. Graversen (2006) found a correlation between intensity of the atmospheric northward energy transport across 60°N and
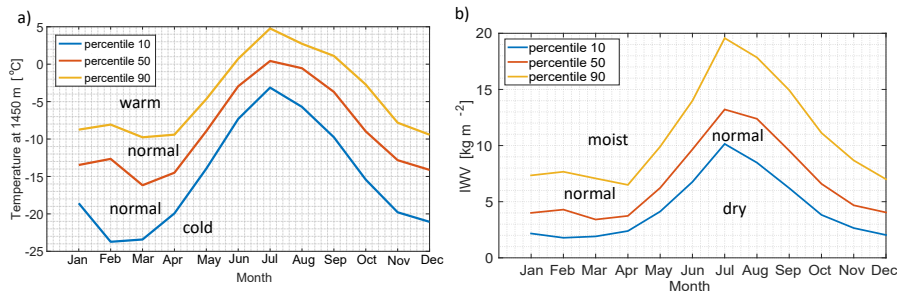
Figure 4.1: Monthly percentiles of 6-hourly (a) mean temperature at 1450 m and (b) IWV from microwave radiometer at Ny-Ålesund from 2011 to 2018 used as criteria for determination of periods of decreased (below 10th percentile, blue line) and increased (above 90th percentile, yellow line) T and IWV. Red line corresponds to the 50th percentile. (published in Nomokonova et al. (2019a))

the Arctic warming/cooling with the time lag of about 5 days. As expected, the occurrence of moist anomalies ("+IWV", red lines in Fig. 4.2) is associated with the air transport from the south, while the dry anomalies ("-IWV", blue lines in Fig. 4.2) related to the air coming from the north. There is a slight difference between the seasons. In winter and spring, dry air typically circulates counterclockwise, from North of Russia over the North Pole region and northern Greenland. Mewes and Jacobi (2019) have shown that this kind of circulation happens when air from the North Pacific flows into the Arctic. In summer, dry anomalies are mostly associated with air coming from northern Canada and Greenland. In autumn, there are two distinct pathways, from south-east and west, although the "-T -IWV" anomalies are related to air coming predominantly from the west (not shown). Wet anomalies are mostly driven by the air advected from the North Atlantic. In autumn and summer, a significant part of moist events originates in the Scandinavian region and Barents sea. The transport pathways for "-T -IWV" and "+T +IWV" events (not shown) are in general similar to those of "-IWV" and "+IWV", respectively, which is in agreement with the results found by Mewes and Jacobi (2019), who showed that the air transport from the North Atlantic sector is typically associated with the positive temperature anomaly, while the transport from Siberia and the North Pacific is connected to a negative temperature anomaly in the Arctic.

Table 4.1 summarizes the occurrence of different types of periods for the analyzed period from June 2016 to October 2018. The occurrence of moist anomalies in winter and summer for the analyzed period is nearly the same as for the reference period, when, according to the definition in the present study, the occurrence of moist and dry anomalies was 10%. In spring and autumn the occurrence is 8 and 14.2%, respectively. The increase in occurrence of moist anomalies during the polar-night season of 2016-2017 was recently reported by (Hegyi and Taylor, 2018). The authors analyzed the whole Arctic region and related the increase to more frequent moisture intrusions from the Atlantic and Pacific regions. Results of the present study show that the occurrence of dry anomalies is about 8% for winter and autumn. In spring and summer dry anomalies were observed about 13% of time. Periods with "+T +IWV" anomaly take a major part (about 67%) of all moist anomalous cases. In contrast, occurrence of "-T -IWV" periods is only about 35% of all dry anomalies
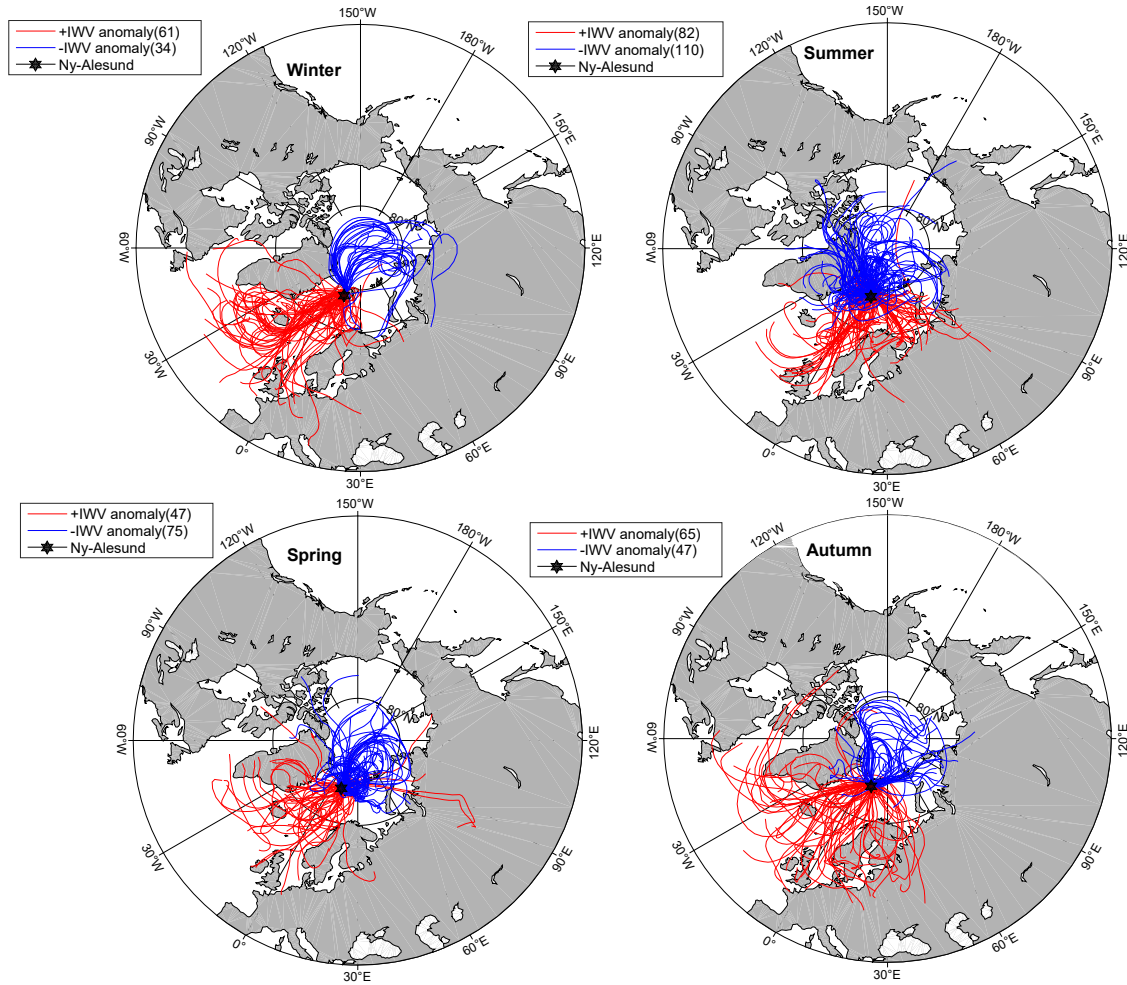
Figure 4.2: Backward trajectories (6 days) for the periods of +IWV and -IWV anomalies arriving at Ny-Ålesund at 1500 m from June 2016 to October 2018. The black star shows the location of Ny-Ålesund. Numbers in brackets show the number of back trajectories available for the corresponding anomaly class. Note that the numbers might be different from those provided in Table 4.1 due to the lower availability of the back trajectories pathways. (published in Nomokonova et al. (2019a))

in all seasons except winter, when the occurrence is almost 90%. Thus, the dry anomalies are not regularly accompanied by a negative anomaly in temperature, while the opposite is valid for moist anomalies.

4.2 Impact on cloud occurrence and cloud phase

In this chapter the results on how the anomalous conditions are related to cloud macro- and microphysical parameters such as occurrence, type, phase partitioning, and LWP and IWP and cloud radiative properties are presented. For the characterization of clouds the cloud detection and classification method based on Cloudnet described in Sec. 4.2.1 were applied. Note, that the method is applied on Cloudnet profiles with no liquid precipitation.

Table 4.1: Number of 6-hourly long periods with increased ("+IWV") and decreased ("-IWV") IWV for the whole period of cloud observations from 2016 to 2018 and for different seasons. Cases with both, increased and decreased T and IWV ("+T +IWV" and "-T -IWV") are also shown. "IWV" corresponds to periods with normal IWV values, regardless which T class the period has. The % values are with respect to all 6-hourly long periods included in the study. (from Nomokonova et al. (2019a))

Type of period	Winter, n cases (%)	Spring, n cases (%)	Summer, n cases (%)	Autumn, n cases (%)	all seasons, n cases (%)
+T +IWV	45 (8.0)	32 (5.4)	53 (6.5)	66 (9.2)	196 (7.3)
+IWV	61 (10.9)	47 (8.0)	82 (10.0)	102 (14.2)	292 (10.9)
IWV	456 (81.1)	465 (78.9)	623 (76.1)	563 (76)	2107 (78.4)
-IWV	45 (8.0)	77 (13.1)	114 (13.9)	53 (7.4)	289 (10.7)
-T -IWV	40 (7.1)	28 (4.8)	37 (4.5)	18 (2.5)	123 (4.6)

4.2.1   Cloud occurrence

Figure 4.3 shows the frequency of occurrence (FOC) of different cloud types during anomalous and normal conditions. Clouds are present in 70–80% of cases with normal values of IWV. Among them about a half are multi-layer clouds.

In dry anomalous events, the FOC of clouds is in general lower and ranges from 26% in spring to 70% in summer. The decrease in FOC of clouds is mostly caused by less frequent multi-layer clouds (MC), whose occurrence in "-IWV" conditions drops by a factor of 2 to 4. During spring and autumn clouds are about a factor of two more frequent during "-T -IWV" events than in "-IWV" cases. The enhanced FOC of clouds may be due to a higher probability of cloud particle formation at lower temperatures for a given amount of water vapor. Nevertheless, during winter and summer there is less difference in cloud occurrence between "-IWV" and "-T -IWV" events.

Unexpectedly high occurrence of clouds ($\sim$92%) was found during "-T -IWV" episodes in autumn. All "-T -IWV" events in autumn occurred from 26 to 30 September 2018. Such a short time period would probably not be representative for autumn "-T -IWV" cases if a longer dataset were analyzed. According to the FLEXTRA backward trajectories for this time period, air was primarily transported from the northern Greenland area. As it will be shown below, the "-T -IWV" episodes in autumn were also characterized by LWP and IWP values exceeding those under normal conditions. A deeper understanding of this phenomenon requires further investigations, which are out of the scope of this study and might be considered as the topics for the future studies.

Higher availability of water vapor ("+IWV") leads to an increase in FOC of clouds up to 90–99%. The increase is mostly caused by changes in MC, while the FOC of single-layer clouds (SC) is not much affected. As it was mentioned in Sec. 4.1, moist anomalies are often accompanied by positive temperature anomalies. Therefore, differences in cloud occurrence between "+IWV" and "+T +IWV" events are small. The findings of this work are in agreement with the study by Gallagher et al. (2018)
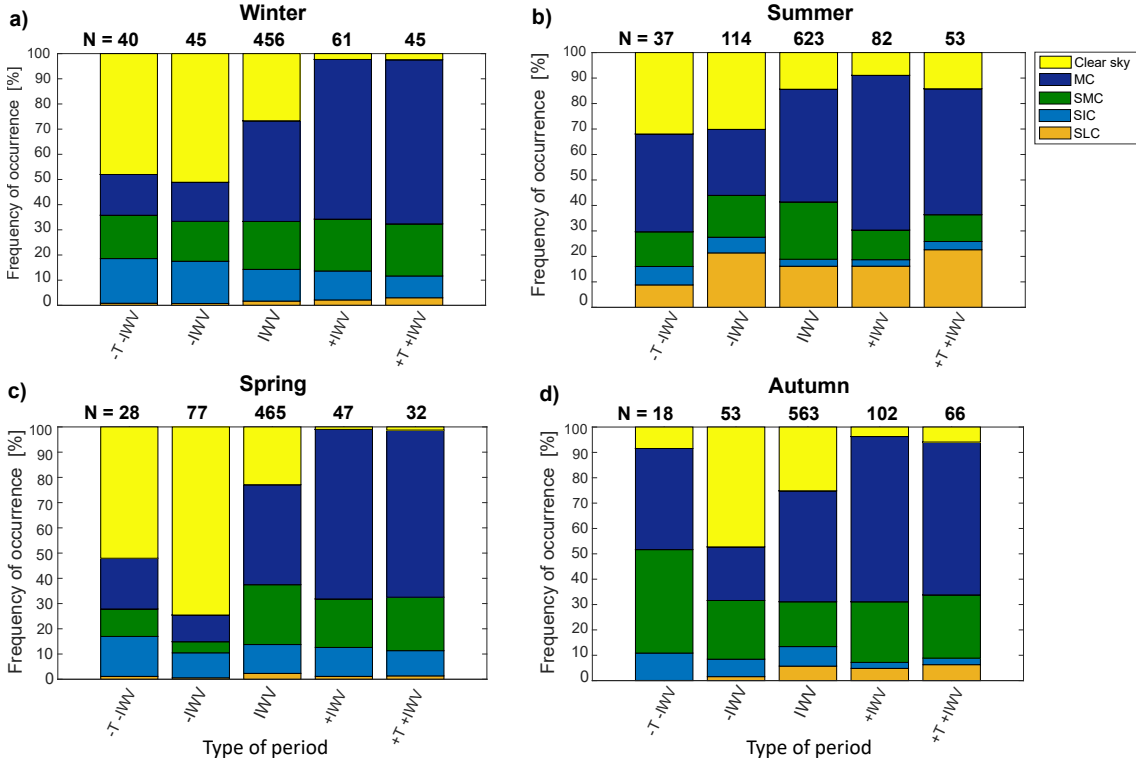
Figure 4.3: Frequency of occurrence of different cloud types for different anomaly periods for winter(a), summer(b), spring(c), and autumn (d). The frequency is normalized to the total number of cases of each anomaly type period. Numbers at the top of bars for each anomaly type show the number of periods included in the corresponding anomaly type based on 6-hourly mean IWV and 1450 m temperature. MC denotes multi-layer clouds, SMC, SIC and SLC stand for single-layer mixed-phase, ice, and liquid clouds, respectively. (published in Nomokonova et al. (2019a))

for Greenland. They showed that during atmospheric circulations associated with increased (decreased) moisture, the number of clear sky scenes reduces (increases).

In winter, the FOC of SC is about 30% and does not strongly depend on the available water vapor. Dry anomalies are characterized by nearly equal occurrence of single-layer ice and mixed-phase clouds (denoted further as SIC and SMC, respectively), while SMC occur a factor of 2 more frequent than SIC during moist anomalies (Fig. 4.3a). This might indicate that SMC, which require a continuous water vapor supply (Korolev and Mazin, 2003), are more persistent in moist conditions, while in dry cases SMC glaciate faster (Korolev and Mazin, 2003).

During summer time a major part of SC are single-layer liquid clouds (SLC) and SMC, with no clear correlation to IWV. During "+IWV" periods the formation of drizzle and rain is expected to be more efficient. Liquid precipitation on the surface often hampers MWR observations and, therefore, according to the Sec. 3.4 is excluded from the analysis. Thus, a part of liquid clouds may be eliminated. In contrast, the high occurrence of SLC of 21% corresponding to "-IWV" event might be caused by less efficient growth of liquid droplets, which results in less likelihood of liquid precipitation.

In contrast to other seasons, in spring dry conditions reduce the occurrence of SC

by about factor of 2. This may result from low availability of IWV, since March and April are the two driest months at Ny-Ålesund (see Fig. 4.1). Nevertheless, during "-T -IWV" events in spring, the FOC of SC is nearly the same as for normal conditions. Since in spring the majority of SC contains ice, the enhanced FOC may result from a higher efficiency of ice nucleation, which, as shown in a number of studies (DeMott et al., 2010; Murray et al., 2012; Hoose and Möhler, 2012; Ladino Moreno et al., 2013; DeMott et al., 2015), in general increases with decreasing temperature.

Autumn is also characterized by a high FOC of SC during "-T -IWV" periods. For instance, SMC occur about 41% of the time, which is 3 times larger than for normal conditions. However, all "-T -IWV" autumn events correspond to a single continuous 5-day episode that was observed from 26 to 30 September 2018. According to the FLEXTRA backward trajectories air was primarily transported from the northern Greenland area during this episode.

4.2.2 Cloud phase

Cloud ice and liquid have distinct microphysical properties. For instance, the size of ice particles is in general larger than for liquid droplets while the latter have a higher number concentration (Korolev et al., 2003). Ice particles can have a large variety of shapes (Bailey and Hallett, 2009). In addition, liquid water and ice have different dielectric properties (Ray, 1972). Thus, the phase composition of clouds affects SW and LW radiative properties of clouds (Ebell et al., 2020). Therefore, the occurrence of different types of hydrometeors in the atmospheric column (Fig. 4.4) was also analyzed.

In general, profiles with liquid phase (sum of green and orange columns in Fig. 4.4) occur more often during moist periods and less often during dry periods. The FOC of liquid containing profiles during "+IWV" and "-IWV" was characterized by the change of more than +30 and -30% relative to normal conditions. Only in summer the increase in FOC of liquid containing profiles between moist and normal periods is 8%. The increase in FOC of clouds in "+IWV" events was mostly related to higher occurrence of MC. FOC of liquid containing clouds during "+IWV +T" and "-IWV -T" anomalies do not differ much from the corresponding water vapor anomalies in all seasons except autumn, when all events corresponded to the single continuous 5-day episode with air masses transported from northern Greenland mentioned in Sec. 4.2.1.

Ice containing profiles (sum of blue and green columns in Fig. 4.4) occur more often under "+IWV" and "+IWV +T" conditions and less during "-IWV" and "-IWV -T". The change in ice containing profiles is mostly defined by the change in profiles with both liquid and ice (green columns in Fig. 4.4), since FOC of pure ice phase (blue columns in Fig. 4.4) varies only slightly with change in IWV. Gallagher et al. (2018), who investigated the influence of atmospheric circulations on cloud composition in Greenland, similarly showed that moist/dry conditions lead to increase/decrease in occurrence of mixed-phase clouds, which are the dominant type of liquid containing clouds in the Arctic (Shupe et al., 2006). Gallagher et al. (2018) also noted that ice clouds are not constrained by circulation types to the same degree as mixed-phase clouds.
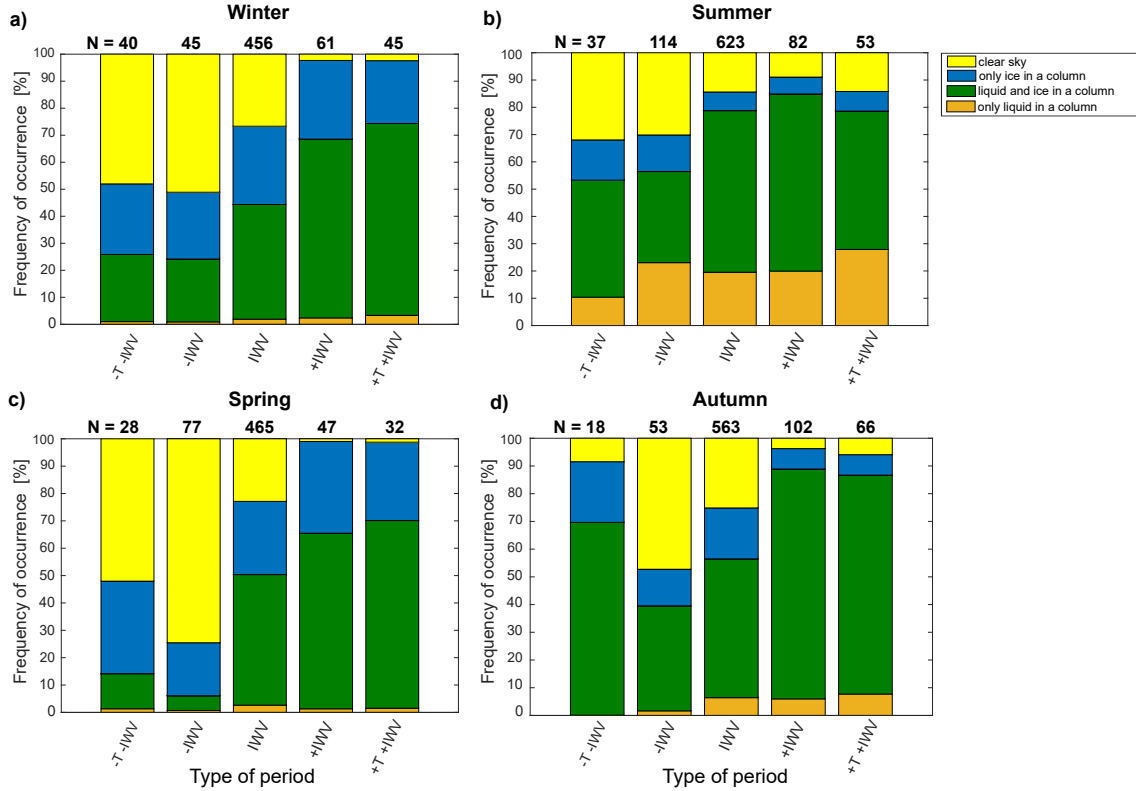
Figure 4.4: Frequency of occurrence of different types of hydrometeors during different anomaly periods for winter(a), summer(b), spring(c), and autumn (d). Numbers at the top of bars for each anomaly type show the number of periods included in the corresponding anomaly type based on 6-hourly mean IWV and 1450 m temperature. (published in Nomokonova et al. (2019a))

4.3   Impact on LWP and IWP

Moist and dry anomalies influence not only the cloud occurrence and composition but also water content. Thus, LWP and IWP were linked to the different types of anomalies (Fig. 4.5). Note, that LWP and IWP were only calculated for liquid-containing and ice-containing profiles, respectively. Clear-sky cases were not added for calculations of the statistics of LWP and IWP.

Following the changes in occurrence of liquid- and ice-containing clouds, LWP and IWP increase under moist conditions and decrease under dry conditions. "+IWV" anomalies cause an increase in mean LWP by a factor of 1.5–2.0 relative to normal conditions and also increase the variability in LWP. During dry anomalies, LWP is significantly lowered and does not exceed 12 and 94 g m^{-2} in winter/spring and summer/autumn periods, respectively. Gallagher et al. (2018) recently showed that atmospheric circulation types associated with enhanced water vapor in Greenland often lead to increased LWP. The authors also showed that opposite is valid for dry conditions, when decreased values of LWP are more likely. Note, that the unexpected two-fold LWP increase during the "-T -IWV" periods in autumn correspond to the 5-day episode with air mass transported from northern Greenland mentioned in Sec. 4.2.1. Moist anomalies correspond to an increase in mean IWP by a factor 3
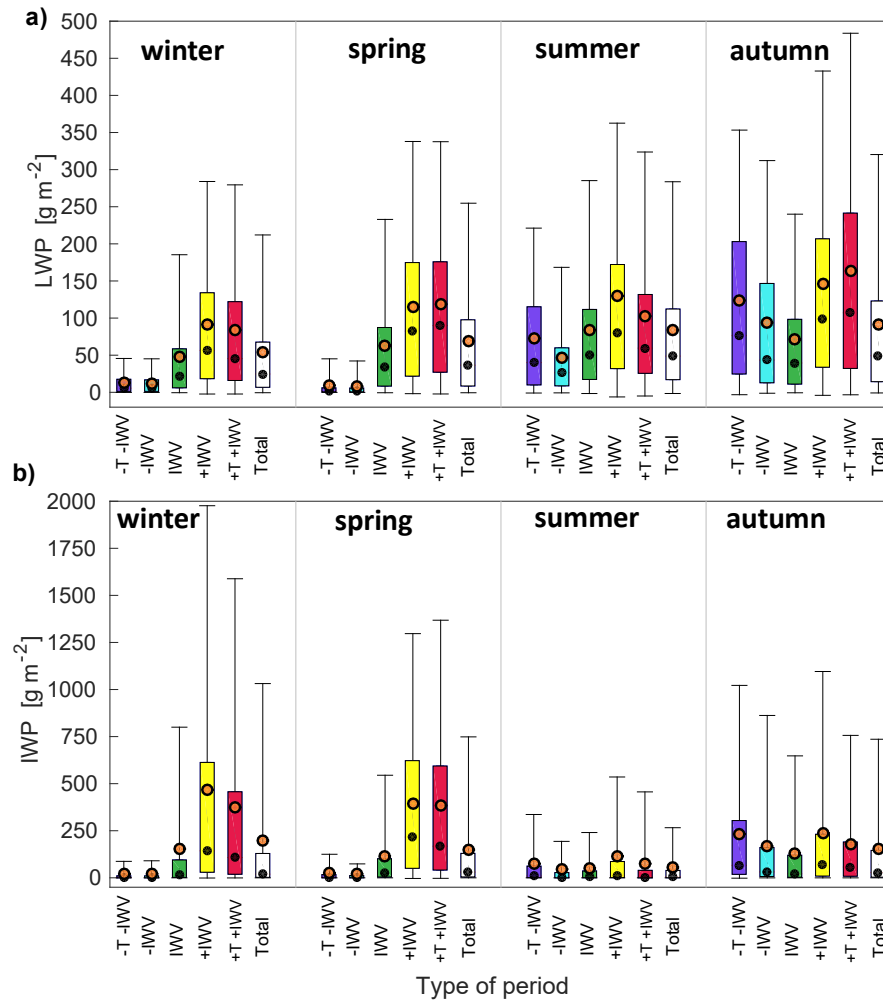
Figure 4.5: LWP (a) and IWP (b) for different anomaly periods and different seasons. Boxes indicate the 25th and 75th percentiles. Upper and lower whiskers show the 95th and 5th percentiles. The white boxes include all cases within a season. Mean (median) values are shown by the orange in black (black) circle marker. (published in Nomokonova et al. (2019a))

relative to normal conditions in winter and spring, and by a factor of 2 in summer and autumn. In winter and spring, dry conditions decrease mean IWP values by an order of magnitude, which may be related to a strong reduction in occurrence of ice containing clouds and less efficient ice particle growth during "-IWV" events. In contrast, during summer and autumn, mean IWP is reduced by a factor of 1.3.

Thus, the results reveal a strong impact of the anomalous periods on LWP and IWP and, in particular in winter and spring. Even though mean IWP values during normal conditions are nearly the same in winter and autumn, relative changes in IWP caused by dry and moist anomalies differ drastically among the two seasons. In winter, wet and dry conditions lead to a 3-fold increase and 10-fold decrease, respectively. In contrast, the increase in autumn is a factor of 2 and there is almost no decrease. Since the anomaly type cannot fully explain this effect, it is probably also related to other factors. One of such factors could be aerosols. Weinbruch et al. (2012); Lange et al. (2018); Jung et al. (2018); Wex et al. (2019) have shown that concentration and chemical composition of cloud condensation (CCN) and ice nuclei

(IN) also have a seasonal variability in the Arctic region. DallOsto et al. (2018) and Lange et al. (2018) found that accumulated aerosol mode is dominant in winter season, while in summer ultrafine aerosol population becomes more abundant. Jung et al. (2018) showed that the seasonal change in the aerosol type affects the activation ability of CCN in the Svalbard region and found the highest activation efficiency in winter and lowest in summer, with intermediate values in spring and autumn. Wex et al. (2019) investigated the annual cycle of IN particles in different Arctic regions. The authors found that IN concentration is often an order of magnitude higher in summer and autumn than in winter and spring. Note, that within this study aerosols are not analyzed.

4.4   Impact on surface cloud radiative effect

In the previous sections, the changes of cloudiness and amount of liquid and ice in a column under various atmospheric states were presented. Liquid-containing and pure ice clouds have a different impact on the radiation budget at Ny-Ålesund (Ebell et al., 2020) and occurrence of these types of clouds varies for dry and moist conditions. Therefore, the surface CRE was also estimated under different atmospheric conditions. Figure 4.6 summarizes the surface SW, LW, and net CRE for different anomaly periods.

During moist anomalies the mean LW CRE increased to 60–70 W m^{-2} in winter, spring, and autumn. Thus, the mean LW CRE, enhanced under moist anomalies in winter, spring, and autumn, can exceed the typical mean LW CRE in summer (Fig. 4.6b, white box). This increase in mean LW CRE is associated with high cloud occurrence, which mostly exceeds 90% under moist conditions. In addition "+IWV" cases typically characterized by high mean LWP and IWP exceeding 90 and 200 g m^{-2}, respectively. In summer the mean LW CRE during moist anomalies becomes lower than under normal conditions. This effect may be caused by influence of water vapor in presence of optically thick clouds as was previously described by Cox et al. (2015). The authors found that for higher relative humidity LW CRE is typically lower. Ebell et al. (2020) identified a similar effect at Ny-Ålesund, where the decrease in LW CRE at the surface for higher IWV corresponds to clouds with LWP exceeding 300 g m^{-2}. In general, relative humidity at Ny-Ålesund is high in summer (Maturilli and Kayser, 2016; Nomokonova et al., 2019b). Moreover, in "+IWV" cases even higher values of relative humidity would be expected, since on average there are no positive temperature anomalies relative to normal conditions.

Dry anomalies correspond to a reduction of the mean LW CRE to 29–32 W m^{-2} in winter and spring and to 5–11 W m^{-2} in summer and autumn. Hence, the dependence of the mean LW CRE on IWV is more pronounced in winter and spring than in autumn and especially in summer. Such behavior though is not directly related to changes in IWV itself but rather to coupling of the changes in IWV to cloud properties. As it was previously shown, dry anomalies are associated with reduced cloud occurrence, amount of liquid-containing clouds, LWP, and IWP, while increased values of these parameters are related to moist periods. In summer the cloud properties do not show as strong change during dry anomalies with respect to normal conditions as in other seasons, which may reflect into the smaller corresponding change in LW CRE.
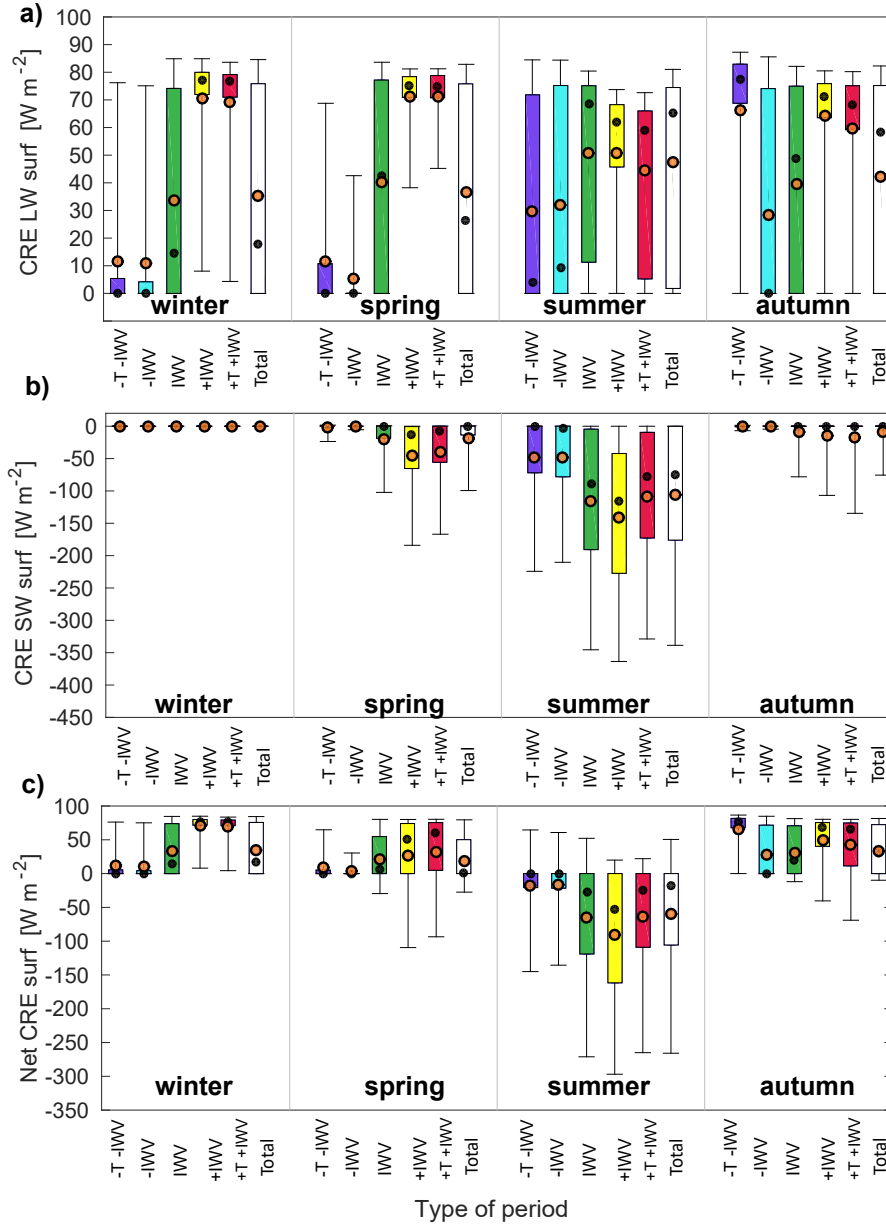
Figure 4.6: SW (a), LW (b), and net cloud radiative effect (c) at the surface for different anomaly periods and different seasons. Boxes indicate the 25th and 75th percentiles. Upper and lower whiskers show the 95th and 5th percentiles. The white boxes include all cases within a season. Mean (median) values are shown by the orange in black (black) circle marker. (published in Nomokonova et al. (2019a))

Besides the influence of cloud occurrence and microphysical properties, the LW CRE also depends on altitude at which clouds occur. Figure 4.7 shows cloud base height (CBH) measured by the ceilometer for the analyzed period. Note, that due to the instrument limitations (see Sec. 2.3), which are related to the attenuation of the ceilometer signal in optically thick clouds, only the lowest CBH was taken into account. Throughout a year, CBH is mostly below 2 km. During moist and dry anomalies CBH either does not change or slightly decreases, which may cause an increase in LW CRE. Although, Yeo et al. (2018), who analyzed the dependence
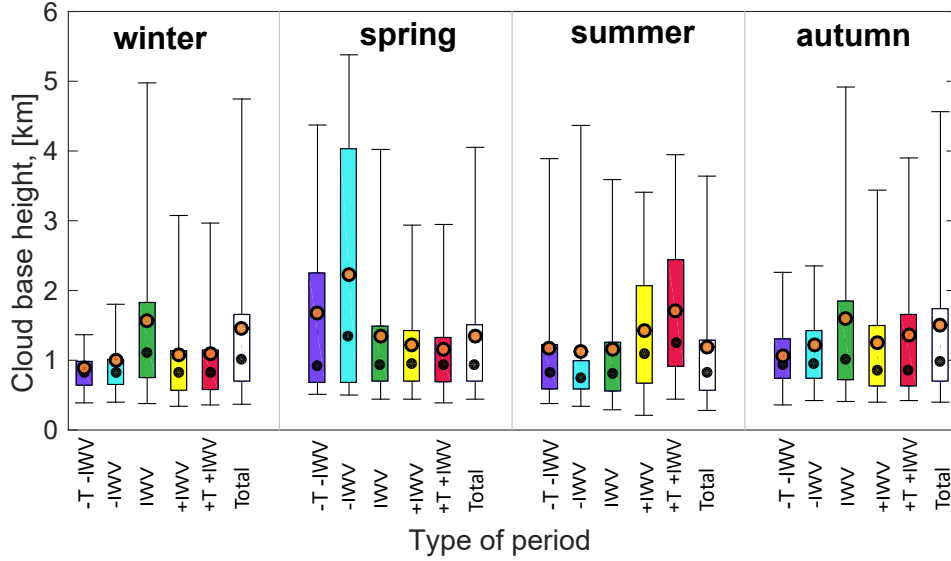
Figure 4.7: Cloud base height of liquid-containing clouds for different anomaly periods and different seasons. Boxes indicate the 25th and 75th percentiles. Upper and lower whiskers show the 95th and 5th percentiles. The white boxes include all cases within a season. Mean (median) values are shown by the orange in black (black) circle marker. (published in Nomokonova et al. (2019a))

of LW fluxes measured at Ny-Ålesund on CBH, showed that the mean LW CRE of clouds within the lowest 2 km does not differ by more than 10 W m^{-2}. Only dry anomalies in spring and moist anomalies in summer are related to higher CBH. Taking into account low cloud occurrence during dry conditions in spring the increase in CBH should not change LW CRE much. In summer the increase in CBH during moist conditions could be another factor (in addition to the effect of water vapor described above) preventing an increase in LW CRE.

The SW CRE is only significant when the sun is above the horizon. Thus, the strongest SW CRE can be found in summer. Under normal conditions in summer and spring the mean SW CRE is -115 and -19 W m^{-2}. An absolute change in CRE_{SW} can in general be caused by three main factors: cloud properties, SZA, and surface albedo (α_s). The 6-fold difference in the mean SW CRE in spring and summer might be associated with the changes only in surface albedo and SZA, since FOC of clouds, LWP, and IWP vary only slightly.

A number of studies have already shown that the surface albedo under clear sky and cloudy conditions can alter the SW CRE at the surface (Shupe and Intrieri, 2004; Miller et al., 2015; Miller et al., 2017; Ebell et al., 2020). Ebell et al. (2020) found that at Ny-Ålesund the surface albedo (ratio between upward and downward SW fluxes at the surface retrieved by the RRTMG) exceeds 0.8 when the surface is covered by snow and is below 0.15 in bare tundra. For the analyzed period, the change in the mean surface albedo between normal conditions and anomalies does not exceed ±0.05 in spring and ±0.1 in summer and autumn. Shupe and Intrieri (2004) showed that SW CRE is nearly proportional to $1 - \alpha_s$. The changes in SW CRE between normal and anomalous conditions caused by the variability in the surface albedo do not exceed 30% in spring and 15% in summer and autumn.

In addition to the surface albedo, the SW CRE at the surface depends on SZA (Minnett, 1999; Miller et al., 2018). Ebell et al. (2020) showed that in Ny-Ålesund the lowest SZA, which corresponds to the highest position of the sun, is in summer with the minimum of 55° in June. In spring values of SZA are larger.

There are two ways SZA can influence differences in SW CRE between anomalous and normal cases: (1) an anomaly can have a dominant daytime of occurrence, while normal conditions are uniformly distributed over a day, and (2) an anomaly can concentrate in a certain part of a season. In order to check for changes in SW CRE between anomalous and normal cases caused by diurnal cycles of SZA the periods whether anomalies have a dominant time of occurrence were checked . It was found that for the analyzed period normal and anomalous cases were nearly uniformly distributed among 6-hourly periods and therefore time of a day is neglected in the following analysis. In order to mitigate the remaining effects of SZA due to the sparse distribution of anomalies over seasons the approach of Sengupta et al. (2003) was followed and adapted to calculate the normalized SW CRE at the surface:

$$\mathrm{nCRE_{SW}} = \frac{\mathrm{CRE_{SW}}}{F_{\downarrow\mathrm{clr,SW}} - F_{\uparrow\mathrm{clr,SW}}}, \tag{4.1}$$

where $\mathrm{CRE_{SW}}$ is the surface SW CRE, and $F_{\downarrow\mathrm{clr,SW}}$ and $F_{\uparrow\mathrm{clr,SW}}$ are down- and upwelling SW fluxes at the surface that would be if the sky were cloud free.

Under normal conditions the mean $\mathrm{nCRE_{SW}}$ is -0.2 and -0.45 in spring and summer, respectively. Dry conditions increase the mean $\mathrm{nCRE_{SW}}$ to nearly 0 and -0.2 in spring and summer, respectively. In moist events the mean $\mathrm{nCRE_{SW}}$ decreases below –0.4. Since the effects of SZA are mitigated in $\mathrm{nCRE_{SW}}$, the variability in mean $\mathrm{nCRE_{SW}}$ for different anomalies is mostly defined by cloud properties and the surface albedo.

The relative change in $\mathrm{CRE_{SW}}$ is unsusceptible to differences in SZA but only when anomaly cases are uniformly distributed over a season. For anomaly cases uniformly distributed over a season no difference it is also expected in surface albedo between anomaly and normal conditions. Thus, similar relative changes in $\mathrm{CRE_{SW}}$ and $\mathrm{nCRE_{SW}}$ and near-zero change in the surface albedo indicate similar SZA and surface albedo for anomaly and normal cases, while the diversion would show that anomaly cases were sparsely distributed over a season.

Table 4.2 summarizes changes in $\mathrm{CRE_{SW}}$, $\mathrm{nCRE_{SW}}$, and the surface albedo related to dry and moist anomalies. The results show that dry cases are related to positive absolute changes in SW CRE, thus pointing to less efficient SW surface cooling by clouds relative to normal conditions. The largest difference of 67.2 W m^{-2} is in summer, when the cloud can produce the strongest SW shading (Shupe and Intrieri, 2004; Ebell et al., 2020). In spring and summer $\mathrm{CRE_{SW}}$, $\mathrm{nCRE_{SW}}$ change by nearly the same factor and the absolute change in the surface albedo does not exceed 0.05. Similar relative changes in $\mathrm{CRE_{SW}}$, $\mathrm{nCRE_{SW}}$ and near-zero absolute change in the surface albedo indicate that the difference in the mean SW CRE is mainly caused by changes in cloud properties and not by SZA. In autumn $\mathrm{CRE_{SW}}$ changed by –94% while $\mathrm{nCRE_{SW}}$ changed by –60%. The difference in the relative changes indicates that it is caused by SZA because dry autumn cases were not uniformly distributed over the season. The absolute change in the surface albedo was 0.45. Thus, the

difference in SW CRE between dry and normal cases under dry conditions in autumn were caused by all three factors, i.e. cloud properties, SZA, and the surface albedo. The direction of the changes in CRE_{SW} is consistent with Shupe and Intrieri (2004), who showed that an increase in the surface albedo corresponds to a reduction in the cloud induced surface SW cooling.

During moist anomalies SW CRE is more negative than for normal conditions. In summer the relative changes in CRE_{SW} and $nCRE_{SW}$ are close and the surface albedo is not altered by more than 0.06. Therefore, it was concluded that the change in the mean SW CRE of $–25.6$ W m^{-2} is mainly caused by cloud properties. In spring and autumn the absolute change in the surface albedo is also relatively low. Nevertheless, the relative changes in CRE_{SW} and $nCRE_{SW}$ differ. This indicates that the absolute change in the mean SW CRE is likely caused not only by cloud properties but also by SZA.

Gallagher et al. (2018) showed an effect of moist and dry anomalies on CRE. The authors analyzed the Summit site in Greenland, where typical IWV values are in the order of 1–3 kg m^{-2} (Pettersen et al., 2018), which is drier than at the Ny-Ålesund station (see Fig. 4.1). Gallagher et al. (2018) used data from 2011 to 2015. The authors found that the southern transport pattern, associated with increase in IWV by 0.69 kg m^{-2}, leads to a change in LW and SW CRE of $+13$ and $–3$ W m^{-2}, respectively, relative to corresponding typical values. Since Gallagher et al. (2018) did not analyze seasons separately, in order to compare the results, the results of present study were also averaged over the whole analyzed period. The mean differences between "+IWV" and "IWV" for LW and SW CRE for Ny-Ålesund were found to be $+21.2$ and -10.2 W m^{-2}, respectively. In contrast, northern circulation pattern in Greenland leads to decrease in IWV by 0.34 kg m^{-2} changes LW and SW CRE by -6.1 and 0.1 W m^{-2} (Gallagher et al., 2018). Our results for Ny-Ålesund are -21.5 and 21.6 W m^{-2}, respectively. Note, that the absolute values may differ because of more humid environment in Svalbard. Nevertheless, the sign of the LW CRE change is the same. SW CRE values are difficult to compare due to and possible differences in SZA and surface albedo. For instance, the change in SW CRE at the Summit station could be closer to 0 due to high albedo in Greenland throughout a year, while at Ny-Ålesund the surface albedo is less than 0.15 in summer (Ebell et al., 2020).

Figure 4.6c depicts a relation of the net CRE to anomaly types. As was reported by Curry et al. (1996), due to the absence of sunlight in the Arctic region during the polar night the LW CRE is dominant and the Arctic clouds warm the surface. Therefore, the mean net CRE in autumn and winter is mostly defined by LW CRE. Influences of water vapor anomalies have been previously discussed in details.

In summer and spring both LW and SW contribute to the mean net CRE resulting in -71.5 and 24.7 W m^{-2} under normal conditions, respectively. Dry conditions correspond to less positive LW and less negative SW CRE, which lead to the mean net CRE of -19 and 4.3 W m^{-2} in summer and spring, respectively. During moist periods LW CRE increases relative to normal conditions in spring and does not change much in summer, while SW CRE becomes more negative in both seasons. Thus, the mean net CRE under moist conditions in spring changes to 31.5 W m^{-2} and to $–101$ W m^{-2} in summer.

Table 4.2: Absolute and relative changes in CRE_{SW}, $nCRE_{SW}$, and surface albedo (α_s) related to dry and moist anomalies. The absolute changes are calculated as a difference between anomalous and normal cases. The relative changes are shown in brackets and are given in percent with respect to normal conditions. Mean values of CRE_{SW} (in $W\,m^{-2}$), $nCRE_{SW}$, and α_s during normal condition are shown in the rightmost column "Normal conditions. (from Nomokonova et al. (2019a))

Parameter	"−IWV"			"+IWV"			Normal conditions		
	ΔCRE_{SW}	$\Delta nCRE_{SW}$	$\Delta \alpha_s$	ΔCRE_{SW}	$\Delta nCRE_{SW}$	$\Delta \alpha_s$	CRE_{SW}	$nCRE_{SW}$	α_s
Spring	+18.8(−95)	+0.2(−98)	+0.05(+7)	−25.2(+128)	−0.3(+156)	−0.06(−7)	-19.73	-0.31	0.81
Summer	+67.2(−58)	+0.2(−51)	+0.03(+26)	−25.6(+22)	−0.1(+19)	+0.06(+50)	-115.71	-0.59	0.13
Autumn	+8.8(−94)	+0.2(−60)	+0.45(+173)	−4.9(+52)	−0.4(+115)	−0.08(−30)	-9.39	-0.31	0.26

4.5   Trends in anomaly occurrence

Since IWV anomalies show a strong impact on cloud properties and their radiative effect, the next question is how the occurrence of dry and moist conditions at Ny-Ålesund has changed in the last decades. The MWR observations at Ny-Ålesund are only available since 2011, and, therefore, cannot be used for such a long-term analysis. Instead, the radiosonde observations were used for the estimation of the occurrence of "-IWV" and "+IWV" events for the time frame from 1993 to 2018. Note, that 6-hour averaged values of IWV from MWR used for the previous analysis cannot be obtained from radiosondes. Therefore, the IWV value for each radiosonde profile was estimated and the profile was classified using the thresholds defined in Sec. 4.1. Even though, results obtained from a radiometer would probably have been slightly different, the radiosondes still show a tendency in the IWV anomalies.

Figure 4.8 shows changes in anomaly occurrences. According to a two-sided t-test, dry and moist anomalies in all seasons show significant trends with the 95% confidence level except for moist anomalies in spring. Dry anomalies have significant negative trends in all seasons, which are especially pronounced in autumn and winter with values of -10.7 and -12.9% decade^{-1}, respectively. About a half of the profiles in autumn and winter of 1993 corresponded to dry anomalies. These trends might be associated with changes in atmospheric circulation found by Dahlke and Maturilli (2017) for the Svalbard region. The dry events in spring and summer also exhibit negative trends but the decrease of their occurrence is at lower rates of – 6.8 and –4% decade^{-1}, respectively. The highest rate of trends for "+IWV" cases were found for winter and autumn with slopes of 5.6 and 6.4% decade^{-1}, respectively. Our results are in line with Mewes and Jacobi (2019), who showed that in winter the occurrence of North Atlantic and North Pacific pathways has increased and decreased, respectively. The North Atlantic and North Pacific air transports are associated with increased and decreased surface temperature and IWV in the Svalbard region (Dahlke and Maturilli, 2017).

Taking into account the link between anomaly types, cloud properties, and CRE (Figs. 4.3–4.6), it is concluded that during the last 25 years the changes in the occurrence of dry and moist anomalies at Ny-Ålesund may have lead to an increase in cloud occurrence, LWP, and IWP in all seasons. In turn, this could have enhanced the cloud related surface warming in autumn, winter, and spring but produce stronger cooling in summer. If the trends of anomaly occurrence continue in the future, it is expected that CRE will become more positive in autumn, winter, and spring and more negative in summer.

4.6   Summary and conclusions

This chapter is devoted to the analysis of anomalous, in terms of IWV and temperature at 1450 m altitude, atmospheric conditions at Ny-Ålesund. The main focus is on the impact of anomalous conditions on cloud properties and their CRE. Within this work, anomalies are defined as a deviation of 6-hour averaged IWV and/or temperature below and above 10th- and 90th percentile of the corresponding parameter over the reference period from 2011 to 2018. Different anomaly types were
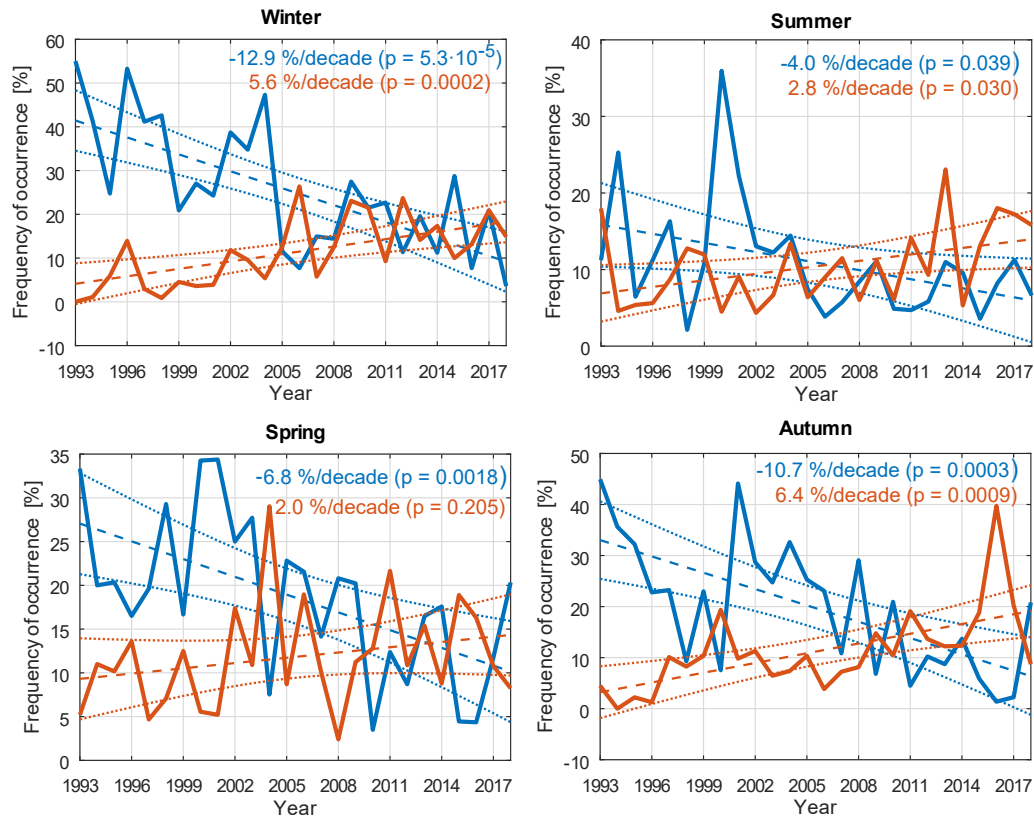
Figure 4.8: Frequency of occurrence of moist ("+IWV", red line) and dry ("-IWV", blue line) events using radiosonde data from 1993-2018 for different seasons (winter (a), summer (b), spring (c), autumn (d)). The red and blue lines correspond to the frequency of occurrence of dry and moist events, respectively. The dashed lines show the linear trend. Dotted lines show the 95th confident intervals for the trends derived by the bootstrapping resampling method. The significance (p value) of the two-sided t-test at 95% level is shown in brackets. (published in Nomokonova et al. (2019a))

related to air flows using backward trajectories FLEXTRA and cloud observations from Cloudnet. The output of the rapid radiative transfer model recently applied by Ebell et al. (2020) to the Ny-Ålesund observations was used to associate the anomaly types to a variation in CRE.

A number of studies on anomalous conditions in the Arctic concentrate only on moist intrusions and/or cover only the winter season (Woods and Caballero, 2016; Graversen and Burtu, 2016; Johansson et al., 2017; Hegyi and Taylor, 2018). In this chapter the focus is not only on warm and moist events, but also on dry and cold anomalies, which have recently been shown to have an impact on the Arctic climate (Sillmann et al., 2013; Collins et al., 2013; Kanno et al., 2019). This chapter also covers all seasons since, for example, surface melt and ice freeze-up in transition periods strongly depend on anomalies in temperature and water vapor (Mortin et al., 2016; Hegyi and Taylor, 2018).

The periods of positive and negative anomalies in temperature and water vapor are correlated with large-scale air transport. Most of the moist events are associated

with air flow from the North Atlantic, while dry periods are mainly caused by air circulating in the Arctic region. This finding is in agreement with previous studies (Maturilli and Kayser, 2016; Dahlke and Maturilli, 2017; Wu, 2017; Mewes and Jacobi, 2019). An analysis of seasonal variability of transport pathways shows that in autumn and summer a significant part of moist events originates from the Scandinavian region and Barents sea. In winter and spring dry conditions were associated with counterclockwise air circulations over the North Pole region. This is in agreement with the results from Mewes and Jacobi (2019), who showed that in winter this type of circulation is related to the North Pacific pathway, which causes cold anomalies for the Svalbard region. In autumn, two distinct pathways, leading to dry conditions at Ny-Ålesund, have been found: from South-East and West. The latter brought the 5-day "-T -IWV" episode observed from 26 to 30 September 2018 with unexpectedly high (typically the FOC of cloud is low during dry anomalies) occurrence of clouds.

Anomalies in IWV correlate with FOC of clouds. In general, dry anomalies are related to cloud occurrence ranging from 26% in spring to 70% in summer, which is on average more than 30% lower than during normal conditions. It was found, that dry conditions also show FOC of multi-layer clouds decreased by a factor of 2 to 4. Although, for autumn and spring FOC of clouds was 2 times higher for "-T -IWV" events than for "-IWV" cases, which is probably due to higher likelihood of cloud particle formation at lower temperatures for a given amount of water vapor. During the moist periods, the FOC of clouds increases up to 90–99%. This increase is mainly caused by more frequent multi-layer clouds while FOC of single-layer clouds is almost not affected. In contrast to dry anomalies, the occurrence of clouds between "+IWV" and "+T +IWV" events does not show a large difference because most of the time moist anomalies were accompanied by the periods with the positive temperature anomaly. 67% of moist anomalies are accompanied by strong temperature increase, while only 43% of dry cases correspond to cold anomalies.

"-IWV" events are characterized by 30% relative decrease in FOC of profiles containing both ice and liquid with respect to normal conditions. These types of profiles become 30% more frequent under moist conditions relative to normal conditions. Profiles with only ice or only liquid are affected by water vapor anomalies to a lesser degree.

Excess and shortage in water vapor has been found to be correlated with mean LWP and IWP. During winter and spring, "+IWV" events are related to a factor of 2–3 increase in LWP and IWP relative to normal conditions, while dry anomalies lead to a reduction of LWP and IWP by an order of magnitude. For example, during normal conditions the mean IWP in autumn is nearly the same as in winter. Nevertheless, the relative change in mean IWP during dry and moist events in spring does not exceed a factor of 2. Thus, the difference between winter/spring and summer/autumn cannot be explained only by water vapor anomalies and should be related to other feedback processes (e.g. difference in aerosol load, orographic effect, dynamics and etc.). During dry anomalies in summer mean LWP decreases by a factor of 2, while mean IWP does not change much. In autumn mean LWP and IWP increase by 30% during dry anomalies. Under moist anomalies mean LWP and IWP increase by a factor of 1.5 and 2.3, respectively. In autumn LWP and IWP increase by a factor of 2 during moist conditions.

Dry(moist) anomalies are associated with less(more) cloud related surface SW cooling. In spring and summer during dry anomaly periods the mean SW CRE was higher. Relative to the normal conditions the changes were 19 and 67 W m^{-2} in spring and summer, respectively. The higher values are associated with lower cloudiness and LWP in dry cases. The difference between summer and spring is caused by the variability of SZA and the surface albedo. During moist periods in spring and summer the cloud related cooling is enhanced by 25 W m^{-2} compared to normal conditions.

The mean LW CRE at the surface is reduced during dry anomalies with respect to normal cases by 25–35 W m^{-2} in winter and spring, and by 11–19 W m^{-2} in summer and autumn. In contrast, moist periods are related to an increase of the mean LW CRE in comparison to normal conditions. The increase was observed in all seasons except summer. For instance, in winter, spring and autumn the mean LW CRE raises from 35–41 W m^{-2} under normal conditions to 64-71 W m^{-2} during moist events. Thus, in winter the mean LW CRE during moist periods was even higher than the typical value in summer (51 W m^{-2}). In summer mean LW CRE did not change during "+IWV" periods and decreased by 6 W m^{-2} during "+T +IWV" periods relative to normal conditions. The effect of reduction in LW CRE during warm and moist conditions in summer is consistent with findings by Cox et al. (2015) and Ebell et al. (2020).

Moist conditions increase the mean net CRE at the surface in autumn, winter, and spring by 5–37 W m^{-2} with respect to normal conditions. This change is mostly defined by cloud radiative properties in LW, which are related to enhanced cloudiness, LWP, and IWP. Dry conditions reduce the mean net CRE by 2–37 W m^{-2} in autumn, winter, and spring. In summer the net CRE is dominated by the SW CRE and, therefore, moist conditions show stronger cloud related surface cooling. During dry conditions in summer there is an increase in the mean net CRE by 49 m^{-2}.

Long-term radiosonde observations show significant trends in the IWV anomaly occurrence. Moist anomalies are getting more frequent with a slope varying for different seasons from 2.8 to 6.4% decade^{-1}, while occurrence of dry anomalies declines at rates from −12.9 to −4% decade^{-1}. Similar results were found for Greenland in study by Mattingly et al. (2016), which shows that most pronounced increasing moist and decreasing dry IWV patterns were in winter. Since moist and dry anomalies are associated with the North Atlantic and the North Pacific, respectively, our results are consistent with findings of Mewes and Jacobi (2019). The authors showed an increase and decrease in occurrence of the North-Atlantic and North-Pacific air transports in winter, respectively. Dahlke and Maturilli (2017) also showed an increase in occurrence of air masses coming from North Atlantic in winter season. Matthes et al. (2015) reported that cold spell events are becoming less frequent in winter and summer for the whole Arctic region.

Since the anomalies are related to a certain patterns in cloud properties and CRE, the trends in the anomaly occurrence over the past 25 years may have lead to increased cloud occurrence, LWP, IWP and, therefore, to higher cloud related surface warming. In addition, if the trends of anomaly occurrences persist in the future, CRE might be more positive in autumn, winter, and spring and more negative summer.

These results show some aspects on how large-scale air transportation may influence atmospheric conditions and, consequently, CRE at Ny-Ålesund. This information is essential for better understanding of relations between these three components of the Arctic climate. As indicated above in this chapter, the significant trends in the occurrence of anomalous conditions are expected to lead to changes in cloud properties and their radiative effect. Nevertheless, qualitative estimates of these changes are challenging since a long-term Cloudnet dataset at Ny-Ålesund is not currently available. Within the (AC)³ (ArctiC Amplification: Climate Relevant Atmospheric and SurfaCe Processes, and Feedback Mechanisms) project the cloud measurements are planned to be continued.

Even though only IWV and temperature are considered in the present study, cloud formation and development also depends on a number of other factors such as aerosol load and chemical composition (Baustian et al., 2012; Murray et al., 2012; Wex et al., 2019), dynamics (Korolev and Field, 2008; Schmidt et al., 2014), influence of surface layer (Morrison et al., 2012) and local orographic effects (Houze, 2012) and other processes. Analysis of these factors is out of the scope of the present study and might be considered in the future studies.

Chapter 5

25 years of longwave cloud radiative effect at Ny-Ålesund

The previous chapter showed that the occurrence of IWV anomaly periods at Ny-Ålesund has shown significant trends over the past 25 years. The trends in the atmospheric state may lead to changes in cloud macrophysical and microphysical properties. The changes in cloud properties in turn affect the surface radiation budget and thus may partly contribute to the observed trends in the surface radiation fluxes reported by Maturilli et al. (2015). As it was mentioned in Sec. 1.3 a minimum set of a cloud radar, ceilometer, and MWR was not set up at Ny-Ålesund until June 2016 and, therefore, long-term statistics of cloud microphysical and radiative properties at Ny-Ålesund is not yet available. Nevertheless, CRE can be estimated from other long-term datasets available for Ny-Ålesund, such as more than 20 years of surface LW and SW fluxes observations and cloud base height measurements, and 8 years of MWR data. For instance, a study of Chen et al. (2006) showed that it is possible to model the sensitivities of CRE to various cloud properties (such as cloud fraction, LWP, cloud base height, and cloud base temperature) by means of neural networks. In a recent study, Nyeki et al. (2019) estimated CRE without cloud observations with active instruments. The authors showed that CRE can be inferred from surface radiation and meteorological measurements, estimating clear-sky longwave fluxes from 2 m temperature and IWV.

The aim of this chapter is to extend the existing 2-year dataset of CRE obtained by Ebell et al. (2020) to the previous two decades. Following Chen et al. (2006), a number of neural networks are trained using different combinations of observables as inputs and the available CRE time series as a target. The present study focuses only on the surface LW CRE due to the large contribution to the surface warming in the Arctic region particular during polar nights without solar radiation (Shupe and Intrieri, 2004; Cox et al., 2016). The extended CRE dataset is analyzed for a presence of significant trends. Further, CRE is parameterized using the occurrence of normal, moist, and dry periods as input.

5.1   Design of neural network retrieval

A neural network is a powerful machine learning tool, which has been widely used for function approximation, classification, and pattern recognition. One of the main advantages of neural networks is that they do not require prior knowledge on the relations between modeled and observed parameters used as input. The description given in this chapter covers the preparation of the dataset, the numerical technique employed for the training of the neural network and the analysis of the model performances. The first two sections of this chapter are based on the handbook on the neural network design by Hagan et al. (2014).

In this thesis neural networks are used to solve a problem of a function approximation. For this task two layer neural networks are typically used. A simplified structure of such a neural network is shown in Fig. 5.1. Input parameters and nodes in the hidden and output layers are connected with weighting links. Each node calculates a sum of the weighted parameters and applies a transfer function, which is a function relating an input of a node with its output. Thus, a two-layer neural network is equivalent to a multidimensional nonlinear regression and can be described by the following equation:

$$\mathbf{y} = \mathbf{f}_2(\mathbf{W}_2\mathbf{f}_1(\mathbf{W}_1\mathbf{p} + \mathbf{b}_1) + \mathbf{b}_2), \tag{5.1}$$

where $\mathbf{y}$ is a vector of output variables, $\mathbf{p}$ is a vector of input variables, $\mathbf{W}_{1,2}$ are weighting matrices, $\mathbf{b}_{1,2}$ are vectors with biases, and $\mathbf{f}_{1,2}$ are transfer functions for the hidden and output layers.

Training of a neural network is an iterative procedure, which estimates weighting matrices $\mathbf{W}_{1,2}$ and bias vectors $\mathbf{b}_{1,2}$ using a training dataset with samples of input variables and corresponding output variables called targets. During each iteration $\mathbf{W}_{1,2}$ and $\mathbf{b}_{1,2}$ are updated in order to minimize the squared difference between the neural network outputs and the targets.

5.1.1   Pre-training

A training of a neural network requires several pre-training steps to be applied to the used dataset: selection of data, data preprocessing, and choice of the network architecture. Long-term datasets collected at Ny-Ålesund include more than 20 years of observations with BSRN and ceilometers, and about 8 year of MWR observations. Thus the following parameters are available for the analysis: zenith TB at 14 frequencies, cloud occurrence, CBH, LW up flux, LW down flux, 2 m temperature, 2 m relative humidity. These parameters were chosen as inputs for neural networks because all of them are directly related to LW CRE. As shown in Eq. 1.3, the difference Q_{LW} between LW down and upwelling fluxes is the all sky component of the LW CRE. Therefore, Q_{LW} calculated from $F_{\downarrow LW}$ and $F_{\uparrow LW}$ measured by BSRN are one of the input variables chosen for the analysis. As it was mentioned in Sec. 2.2, TBs measured by MWR are used to estimate atmospheric temperature, humidity, IWV, and LWP. Since, as shown in Sec. 1.4, all these parameters have an impact on LW CRW, TBs were chosen as one of the input variables for the neural network training. Section 1.5 showed that some studies use surface measurements of LW
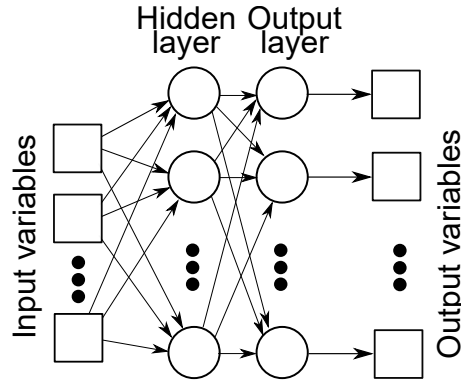
Figure 5.1: A simplified scheme of a 2 layer neural network. Input and output variables are scalars and shown as squares. Nodes of the hidden and output layers are shown as circles. The nodes perform weighting, add biases, and apply the transfer functions as shown in Eq. 5.1.

downwelling flux, air temperature, and relative humidity to identify the presence of clouds, when active instrumentation is not available, and to approximate clear sky LW fluxes.

Equations 2.6 and 2.7 show that the values of LWP estimated from MWR's TBs are used to retrieve cloud microphysics. CRE calculated using the retrieved microphysics can be affected by instrumental biases of MWR. The instrumental biases are likely to vary within the 8 years of observations. For training only a 2-year period is used, thus the relations between CRE and the measured TBs during the training period can differ from previous 6-year period. In order to avoid instrumental effects, simulated TBs are used for the training. Another reason to utilize simulated TBs for the neural network training is that their values were derived using the same thermodynamic and cloud profiles as those used for the modeling of CRE. The TBs are simulated using thermodynamic profiles from GDAS1 and the ICON model (Sec. 2.6) and cloud profiles from the dataset described in Sec. 2.7 by applying the same radiative transfer model as used for the radiometer retrievals (Sec. 2.2). Ebell et al. (2020) extended the thermodynamic profiles to 30 km with mean monthly climatological profiles based on radiosonde observations from Ny-Ålesund and linearly interpolated the profiles to the 30 s Cloudnet grid. The lowest temperature in the model is replaced by the temperature measured at 10 m.

It is known that observations taken by MWRs are partly correlated at different frequencies (Tan et al., 2011). Therefore, the principal component analysis is applied to the simulated TBs in order to reduce the dimension of the data. The dimension reduction helps to simplify the neural network architecture and drastically speeds up the training procedure. Using simulated TBs for the time period from June 2016 to October 2018 the covariance matrix $\mathbf{C}_{TB}$ was calculated:

$$C_{i,j} = \langle (TB_i - \langle TB_i \rangle)(TB_j - \langle TB_j \rangle) \rangle, \qquad (5.2)$$

where $C_{i,j}$ are elements of the covariance matrix, i and j denote MWR channels (1–14) and $\langle \rangle$ denotes the mean value. The covariance matrix $\mathbf{C}_{TB}$ can be decomposed as follows:

$$\mathbf{P}\mathbf{C}_{TB}\mathbf{P}^T = \mathbf{D}, \tag{5.3}$$

where $\mathbf{D}$ is a diagonal matrix, $\mathbf{P}$ is a rotation operator, and T denotes transposition. The rows of the matrix $\mathbf{P}$ are the eigenvectors or principal components while diagonal elements of $\mathbf{D}$ are eigenvalues. The eigenvectors constitute an orthonormal basis for the space spanned by $\mathbf{C}_{TB}$ and the eigenvalues are the variances associated with the corresponding principal components. In the following discussion only the 3 principal components with the largest eigenvalues are used. For the neural network training projections of simulated TBs on the 3 principal components are used. These projections are denoted TBPC hereafter.

Instruments measuring surface LW fluxes have a field of view of 180° and, therefore, the observed fluxes are influenced by 3D effects associated with horizontal fluctuations of the atmospheric state. In contrast, RRTMG assumes horizontal homogeneity of the atmosphere and does not take into account 3D effects (Ebell et al., 2020). In order to avoid the influence of the 3D effects on the training of the neural network, the surface LW fluxes simulated by RRTMG were used. For consistency purposes, simulated fluxes were derived using the same thermodynamic and cloud profiles as those used for the modeling of CRE.

Chen et al. (2006) showed that estimation of LW CRE using neural networks requires an input characterizing cloud fraction and/or cloud height. The long-term dataset at Ny-Ålesund contains ceilometer observations which can be used for this purpose. In general, as for previously described input variables, it would be beneficial to use simulated ceilometer data in order to avoid instrument related effects in the LW CRE retrieval, and to keep consistency in the source of the training dataset. Nevertheless, as it was shown in Sec. 3.5, NWP models may not properly characterize liquid phase in clouds. Therefore, proper simulations of ceilometer observations are currently not available. Cloudnet cloud profiles obtained from ceilometer and cloud radar observations are used by RRTMG to calculate CRE. As a consequence, CRE is set to 0 when there is no cloud detected. Thus, a neural network trained with the cloud detection from Cloudnet as an input would strongly rely on this input in order to discriminate cloudy and clear sky conditions. Ceilometers are known to miss clouds with low concentration of particles (Bühl et al., 2013). Therefore, if ceilometer data alone (without the radar) are utilized to identify the cloud presence and used as the input to the neural network trained with the Cloudnet cloud detection, the neural network may erroneously consider some cloudy profiles as cloud free and consequently assign CRE close to 0. This indicates, that the utilization of the cloud detection from Cloudnet as an input may lead to uncertainties related to the cloud detection abilities of the ceilometer alone. Thus, in this study the cloud base height measurements are used as an input for the neural network training. Cloud base heights are taken from the ceilometer CL51. This ceilometer is able to detect multiple cloud bases in a single column. In this study only the lowest cloud base is used. The first cloud base is the most important for the LW radiation. In addition, previous two ceilometers only measured the lowest cloud base. Cloud fraction is set to one if a cloud base is detected and is set to 0 otherwise.

LW CRE calculated using RRTMG by Ebell et al. (2020) is used as the output variable. LW CRE has 30 s time resolution corresponding to the resolution of Cloudnet. Note that calculations of LW CRE are made only for profiles with valid radiometer,

Table 5.1: Standard deviations of the noise added to the variables used for the neural network training.

Variable	Value
CRE [W m^{-2}]	20.2
$F_{\downarrow LW}$ [W m^{-2}]	12.5
Q_{LW} [W m^{-2}]	14.8
2 m temperature [°C]	1
2 m relative humidity [%]	10
TB [K]	4

ceilometer, and radar data. In addition to zenith observations, MWR performs periodical scanning cycles. Samples corresponding to these scans are excluded. Profiles with liquid precipitation are also excluded from the analysis because observations of MWR can be contaminated by the presence of liquid water on the radome. The availability of 30 s LW CRE samples for the period from June 2016 to October 2018 is relatively uniform and on average about 50% of the data can be used.

A proper neural network training requires that the training dataset should adequately represent the input space, i.e. the range of the input parameters in the training dataset and the long-term observations should be similar. Therefore, distributions of the input parameters used for the training were compared with those from the measurements (see Appendix A). The results show that the training dataset covers 80–100% of the variability observed over 8 years for TBs and 25 years for radiation and meteorological observations.

Ebell et al. (2020) estimated random uncertainties of LW CRE averaged over 10 min intervals to be about 20 W m^{-2}. Since averaging typically reduces the random variability, LW CRE and all the input variables with the original 30 s time resolution are averaged over 10 min intervals. In addition, the 10 min averaging minimizes the influence of field-of-view differences of the used instrumentation and small-scale cloud inhomogeneities (Shupe et al., 2015). For each of 10 min intervals availability of all the variables is checked. 10 min intervals where at least one of the variables has less than 70% of samples are excluded from the analysis. It was found that about 85% of the averaged values of cloud fraction correspond to either no cloudy samples (cloud fraction = 0) or all cloudy samples (cloud fraction = 1). Since the amount of intermediate values of the cloud fraction is low, all the values of the cloud fraction above 0 are set to 1.

In total, there are 73020 10 min samples with all the input and output variables available from 11 June 2016 to 8 October 2018. In order to take into account the uncertainties between the simulated variables and measured quantities, Gaussian noise was added to the input and output variables. The noise standard deviation values are chosen to match the measurement uncertainties (see Chapter 2) and are reported in Table 5.1.

According to a standard practice (Hagan et al., 2014), all the variables used for neural network training are normalized such that they all span between –1 and 1:

$$p_{k,\mathrm{nrm}} = \frac{2(p_k - p_{k,\mathrm{min}})}{(p_{k,\mathrm{max}} - p_{k,\mathrm{min}})} - 1, \qquad (5.4)$$
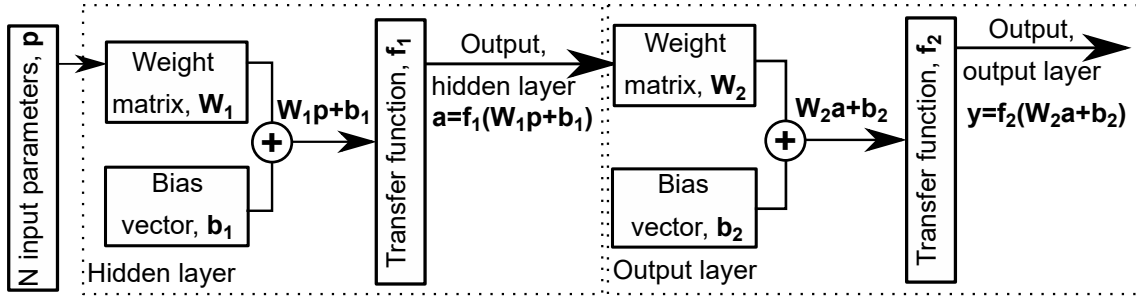
Figure 5.2: The 2-layer neural network used in this study. The weight matrices $\mathbf{W}_1$ and $\mathbf{W}_2$ have dimensions $30 \times N$ and 1×30, respectively. N is a number of input parameters. $\mathbf{b}_1$ and $\mathbf{b}_2$ are 30×1 and 1×1 vectors, respectively.

where p_k and $p_{k,\mathrm{nrm}}$ are values of the k-th input variable before and after the normalization, $p_{k,\mathrm{min}}$ and $p_{k,\mathrm{max}}$ are the minimum and maximum values of the k-th input variable.

As it was mentioned above the function approximation or regression tasks are typically solved using a two layer perceptron neural network. The number of nodes in the output layer corresponds to the number of output variables, which is 1. For the hidden layer, 30 nodes was chosen. This number was found to be a compromise between the training quality and the training speed. The hyperbolic tangent sigmoid is used as the transfer function in the hidden layer:

$$f_{ts}(x) = \frac{e^x - e^{-x}}{e^x + e^{-x}}, \tag{5.5}$$

while the linear transfer function is used in the output layer:

$$f_l(x) = x. \tag{5.6}$$

The resulting architecture of the used neural network is shown in Fig. 5.2.

The parameters chosen as inputs for the neural network training have different availability ranging from 8 years for TBs from MWR to about 25 years for surface fluxes from BSRN. Therefore, within this study different sets of input parameters are used to train a number of neural networks, which are applicable for different time periods. A list of the neural networks is given in Table 5.2. The sets of input variables were chosen in a way to check how good can different instruments or instrument sets approximate LW CRE. For instance, the neural networks 1 and 2 are based only on MWR observations, the neural networks 8 and 9 use only BSRN, while other neural networks use a combination of the instruments.

5.1.2   Training the networks

As a first step of the training procedure, the weight matrices $\mathbf{W}_{1,2}$ and bias vectors $\mathbf{b}_{1,2}$ are initialized. As a rule of thumb, initial values of the weights and biases should be set to small random values. For the hidden layer, the initialization method introduced by Nguyen and Widrow (1990) is used. According to this method, magnitudes of the elements of the weight matrix $\mathbf{W}_1$ are set to $0.7 \times 30^{1/N}$, where 30

Table 5.2: The list of neural networks trained within this study to retrieve LW CRE.

Index	Input variables
1	TBs
2	TBPC
3	TBPC and cloud fraction
4	TBPC, cloud fraction, and Q_{LW}
5	TBPC, cloud fraction, Q_{LW}, and cloud base height
6	cloud fraction, Q_{LW}, and month
7	cloud fraction, Q_{LW}, month, 2 m temperature, and 2 m relative humidity
8	Q_{LW}, month, and $F_{\downarrow LW}$
9	Q_{LW}, $F_{\downarrow LW}$, 2 m temperature, and 2 m relative humidity

corresponds to the number of nodes in the hidden layer, N is the number of input parameters used for the neural network training. Signs of the elements are set randomly. Elements of the bias vector $\mathbf{b}_1$ are set to uniform random values between $-0.7 \times 30^{1/N}$ and $0.7 \times 30^{1/N}$. Elements of $\mathbf{W}_2$ and $\mathbf{b}_2$ are set to uniform random values between –0.5 and 0.5.

For the training, the Levenberg-Marquardt minimization algorithm with the Bayesian regularization (Hagan et al., 2014) was used. This algorithm consists of the following steps:

1. The state vector $\mathbf{x}_0$ is formed by all the elements of the weight matrices $\mathbf{W}_{1,2}$ and bias vectors $\mathbf{b}_{1,2}$. The size of the state vector is denoted n hereafter. The sum of squared elements E_w of the state vector is calculated.

2. γ, which is the number of effective parameters, is set to n.

3. For each sample $\mathbf{y}$ is calculated using the Eq. 5.1 and normalized input variables $\mathbf{p}$.

4. The error vector $\mathbf{v}$ is derived. Elements of $\mathbf{v}$ are differences between $\mathbf{y}$ and corresponding normalized target values. The sum E_d of squared errors is calculated.

5. Two parameters α and β controlling the complexity of the network are calculated:

$$\alpha = \frac{\gamma}{2E_w}, \tag{5.7}$$

$$\beta = \frac{N - \gamma}{2E_d}. \tag{5.8}$$

6. The cost function F is computed:

$$F = \beta E_d + \alpha E_w. \tag{5.9}$$

The first and the seconds terms in Eq. 5.9 penalize the deviation of the neural network output from the target values and the complexity of the neural network, respectively.

7. The Jacobian matrix $\mathbf{J}$ characterizing the sensitivities of the output variables to the elements of the weight matrices $\mathbf{W}_{1,2}$ and the bias vectors $\mathbf{b}_{1,2}$ is calculated:

$$J_{q,p} = \frac{\partial v_q}{\partial x_p}, \tag{5.10}$$

where v_q is the q-th element of the error vector and x_p is the p-th element in the state vector.

8. A new state vector $\mathbf{x}_{k+1}$, with k denoting the iteration index, is calculated as follows:

$$\mathbf{x}_{k+1} = \mathbf{x}_k - \left[\beta\mathbf{J}^T\mathbf{J} + (\mu + \alpha)\mathbf{U}\right]^{-1}\left(\beta\mathbf{J}^T\mathbf{v} + \alpha\mathbf{x}_k\right), \tag{5.11}$$

where $\mathbf{U}$ is the $n \times n$ identity matrix. During the initial iteration ($k = 0$) the coefficient $\mu = 0.01$ is used.

9. E_w, E_d and F are recalculated. If after an iteration F does not decrease, the steps 7–9 are repeated with μ multiplied by 5. If the iteration yields lower F, μ is divided by 5.

10. γ is updated:

$$\gamma = n - 2\alpha\text{tr}(\mathbf{H})^{-1}, \tag{5.12}$$

where Hessian matrix is approximated by:

$$\mathbf{H} = 2\beta\mathbf{J}^T\mathbf{J} + 2\alpha\mathbf{U}. \tag{5.13}$$

11. New estimates of α and β are derived according to Eqs. 5.7 and 5.8, respectively.

12. The steps 7–11 are repeated 100 times. The number of iterations should be large enough to allow the iterative minimization scheme to converge. The neural networks trained for this study typically required much less iterations to fully converge.

The described training algorithm includes the Bayesian regularization, which avoids the over-fitting problem (Hagan et al., 2014). In order to illustrate this, the dataset was split into the training and validation datasets with 80 and 20% of the samples, respectively. Samples for these datasets were chosen randomly. The training dataset was used for the neural network training, while the validation dataset was only used to check for over-fitting. For each set of input parameters listed in Table 5.2 3 to 5 instances of each neural network type were trained. Among these, the neural networks with the lowest final cost functions were taken for the following analysis.

Table 5.3: Statistics of differences between the neural networks outputs and the target values of LW CRE with the added Gaussian noise. The values were calculated using the training and validation (numbers in brackets) datasets for different input parameters. Neural network indexes are the same as provided in Table 5.2. The period from June 2016 to October 2018 was used. Note, that the neural networks cannot predict random noise and, therefore, the values of RMSD always exceed the standard deviation of the Gaussian noise of 20.2 W m^{-2} added to LW CRE during the pre-training.

Index	RMSD [W m^{-2}]	STD [W m^{-2}]	Bias [W m^{-2}]	Correlation
1	34.2 (34.0)	34.2 (34.0)	-0.3 (0.0)	0.53 (0.54)
2	34.2 (34.0)	34.2 (34.1)	-0.6 (-0.2)	0.53 (0.53)
3	27.3 (27.0)	27.3 (27.0)	0.0 (-0.1)	0.74 (0.74)
4	22.7 (22.6)	22.7 (22.6)	-0.4 (-0.0)	0.83 (0.83)
5	22.0 (22.0)	22.0 (22.0)	0.3 (-0.0)	0.84 (0.84)
6	22.9 (22.9)	22.9 (22.9)	-0.0 (-0.1)	0.83 (0.82)
7	22.7 (22.6)	22.7 (22.6)	-0.0 (0.0)	0.83 (0.84)
8	22.1 (22.1)	22.1 (22.1)	-0.4 (-0.0)	0.84 (0.84)
9	21.8 (21.9)	21.8 (21.9)	-0.6 (-0.2)	0.84 (0.84)

5.2 Assessment of the neural network model performances

5.2.1 Neural network model quality

Before the neural networks are applied to the measurement dataset, the quality of the obtained networks was analyzed. For this purpose differences between the neural network outputs and the target values of LW CRE were derived separately for the training and the validation datasets. The root-mean-squared difference (RMSD), mean and standard deviation of the difference, as well as the correlation between the neural network outputs and the target values of LW CRE were calculated. The results are summarized in Table 5.3. Similar values for the training and the validation dataset indicates that the Bayesian regularization successfully avoided the over-fitting problem during the trainings.

The results show that all the bias values are close to 0 and the correlation ranges from 0.52–0.84. This indicates that the neural networks captures general relations between the input variables and LW CRE. Since neural networks (and also other regression algorithms) cannot predict random noise, the lowest possible RMSD is limited by the noise added to LW CRE during the pre-training (see Table 5.1). Neural networks based only on microwave brightness temperatures (indexes 1 and 2) showed the worst results with about 34 W m^{-2} RMSD. There are no differences between neural networks 1 and 2, which indicates that most of the information on the LW CRE is contained in the first three principal components. Additional information on cloud occurrence, LW net radiation, and cloud base height (neural networks 3–5) improves the performance of the neural networks. Apparently, cloud base height does not improve the performance much if the cloud fraction has been

Table 5.4: Parameters of linear regressions between neural network outputs and LW CRE without additional noise. All available 10 min samples were used for the linear regressions including the training and validation datasets. An ideal model would have the slope and offset of 1 and 0, respectively.

Index	Slope	Offset [W m^{-2}]
1	0.38	23.8
2	0.38	23.6
3	0.74	9.9
4	0.91	3.4
5	0.94	2.1
6	0.90	3.8
7	0.91	3.5
8	0.93	2.4
9	0.95	2.0

already used as an input. Neural networks 4–9 show RMSD close to the limit of 20.2 W m^{-2} defined by the added noise.

In order to check how well a neural network explains the variability of the LW CRE, linear regressions between the network outputs and LW CRE without the added noise were obtained. Slopes and offsets of the linear regressions are shown in Table 5.4. The results indicate that the neural networks 1 and 2, which are based on microwave TBs only, have relatively large offsets and slopes of 0.38. During clear sky conditions, these neural networks overestimate LW CRE and show values about 10 W m^{-2}, while for optically thick clouds they underestimate LW CRE and the maximum output values of LW CRE are about 70 W m^{-2}. Therefore, these neural networks cannot properly model the 10 min variability of LW CRE. The neural network 3, which uses TBPC and cloud fraction, performs better with smaller offset and the slope closer to unity. Much better results were shown by neural networks 4–9 with offsets of 2.0–3.8 W m^{-2} and slopes close to 1.

5.2.2   Validation of the neural network model

As the next step, the neural networks were applied to the observations for the period from June 2016 to October 2018 in order to see their performance on a real measurements taken as inputs instead of simulations. Differences between the neural network outputs and the target values of LW CRE with the added Gaussian noise were analyzed in terms of RMSD, mean and standard deviation of the difference, as well as the correlation. Table 5.5 shows the difference statistics when observations from the MWR and BSRN are used instead of simulated TBs, TBPC, Q_{LW}, and $F_{\downarrow LW}$.

A comparison of Tables 5.3 and 5.5 shows that the difference statistics for the simulated and measured input variables are similar. Better results of neural networks 1–3 with measurements are likely to be caused by lower instrumental noise of the MWR than was assumed for the simulated TBs. Nevertheless, for the years 2011–2016 the noise statistics of the MWR can be different from 2016–2018. Mean differences are in

Table 5.5: Statistics of differences between the neural networks outputs and the target values of LW CRE with the added Gaussian noise. Measured variables were used as input parameters for neural networks instead of simulations. Neural network indexes are the same as provided in Table 5.2. The period from June 2016 to October 2018 was used. Note, that the neural networks cannot predict random noise and, therefore, the values of RMSD always exceed the standard deviation of the Gaussian noise of 20.2 W m^{-2} added to LW CRE during the pre-training.

Index	RMSE [W m^{-2}]	STD [W m^{-2}]	Bias [W m^{-2}]	Correlation
1	30.3	30.2	2.2	0.66
2	30.2	30.2	0.8	0.66
3	25.8	25.7	1.9	0.76
4	22.8	22.8	-0.2	0.82
5	22.6	22.6	0.3	0.82
6	22.9	22.9	-0.3	0.82
7	22.9	22.9	0.0	0.82
8	23.4	23.4	-0.6	0.81
9	22.7	22.7	-0.6	0.83

general larger in the case of measurements taken as inputs, although the magnitude of the mean differences does not exceed 2.2 W m^{-2}.

5.2.3 Uncertainty analysis of the LW CRE retrievals based on neural networks

As it is shown in Table 5.5, RMSE of the estimated 10 min LW CRE is relatively large taking into account that the typical range of LW CRE is from 0 to 85 W m^{-2}. Therefore, a longer averaging is required for an analysis of these estimates. In this chapter the main focus is to relate seasonal changes of LW CRE to trends in the occurrence of wet and dry anomalies and, therefore, LW CRE is averaged seasonally. Ebell et al. (2020) estimated the random uncertainty of the LW CRE from RRTMG averaged over a month to be in the order of 0.4–0.5 W m^{-2}. Averaging over a season would further reduce this estimate by a factor of $\sqrt{3}$ assuming that the random error in monthly averaged LW CRE is not correlated. In contrast to the random uncertainty, the systematic uncertainty in LW CRE is not reduced by averaging. Using the time period from June 2016 to October 2018 Ebell et al. (2020) found differences between simulated and measured surface LW net fluxes for all sky and clear sky conditions to be -0.2 and -4.9 W m^{-2}, respectively. The authors note that the bias in the case of clear sky conditions results from 3D effects, which are not taken into account by RRTMG, a misclassification of the scene (cloudy/cloud-free, cloud type), and uncertainties in the cloud microphysical properties. It is not clear whether these biases would be the same for previous periods, and therefore, as a proxy of the uncertainty related to the modeling of the surface clear-sky LW flux of ± 4.7 W m^{-2} is further used.

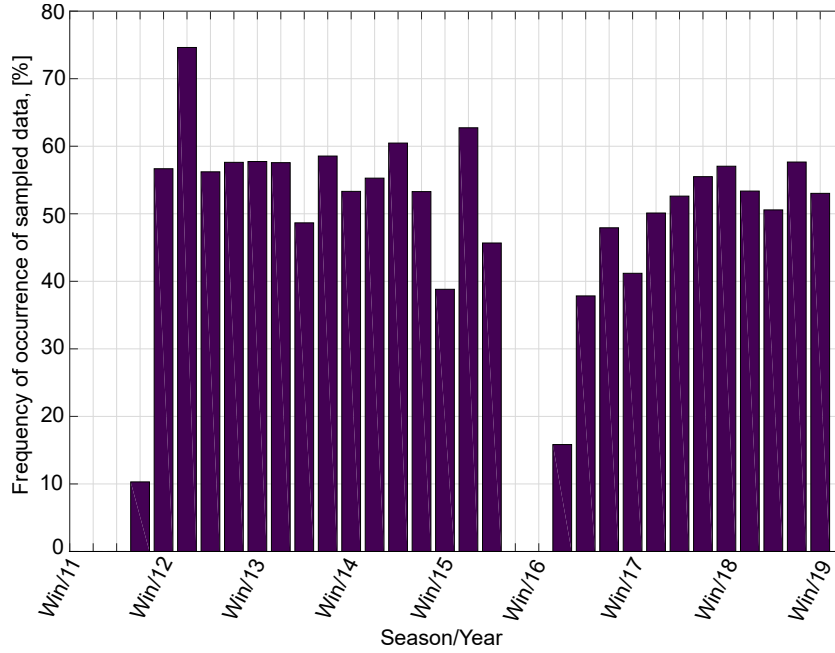Training of neural networks was based on LW CRE calculated using RRTMG (Ebell

Figure 5.3: Yearly seasonal frequency of occurrence of sampled MWR radiometer data for the period of cloud observations.

et al., 2020). As the period with calculated LW CRE is relatively short, the uncertainties of the neural network LW CRE retrievals applied to a longer datasets may be related to several aspects. First, during the training of the neural networks the cost function was calculated for all available samples in the training dataset. These samples are fairly uniformly distributed over the period from June 2016 to October 2018. Nevertheless, neural networks may perform better for some particular seasons and/or years. The second aspect is that LW CRE is only calculated when data from all the instruments required for Cloudnet were available. MWR data were often excluded from the analysis due to the wet radome during liquid precipitation or problems with the hardware. Therefore, the availability of data used for the training might be not homogeneous in time, which can be one of the reasons why neural networks perform differently for different seasons. Moreover, this aspect can affect the performance of neural networks on a longer dataset. Third, neural networks 1–5 require zenith observations with MWR, while this instrument routinely performs scanning patterns, thus reducing number of samples available for the application of the neural networks. Availability of proper MWR samples is mostly around 40–50% (Fig. 5.3). Figure 5.4 shows how different input variables are affected by the subsampling due to MWR radiometer availability. For this, the seasonal averages of variables were calculated for all available samples and only those with valid MWR data. In general, the results show similar behavior in all the variables with relatively small changes. Beside the averages, it is important to check how the sampling affects the distributions of the input parameters within each period. The analysis of the parameter distributions estimated from all available sample and only when MWR data are available (shown in Appendix B) does not show strong deviations. Typical absolute differences between the distributions at the percentile levels of 25, 50, and 75 are less than 250 m, 10 W m^{-2}, 6 W m^{-2}, 3%, and 1°C in cloud base height, $F_{\downarrow SW}$, Q_{LW}, relative humidity at 2 m, and temperature at 2 m, respectively.
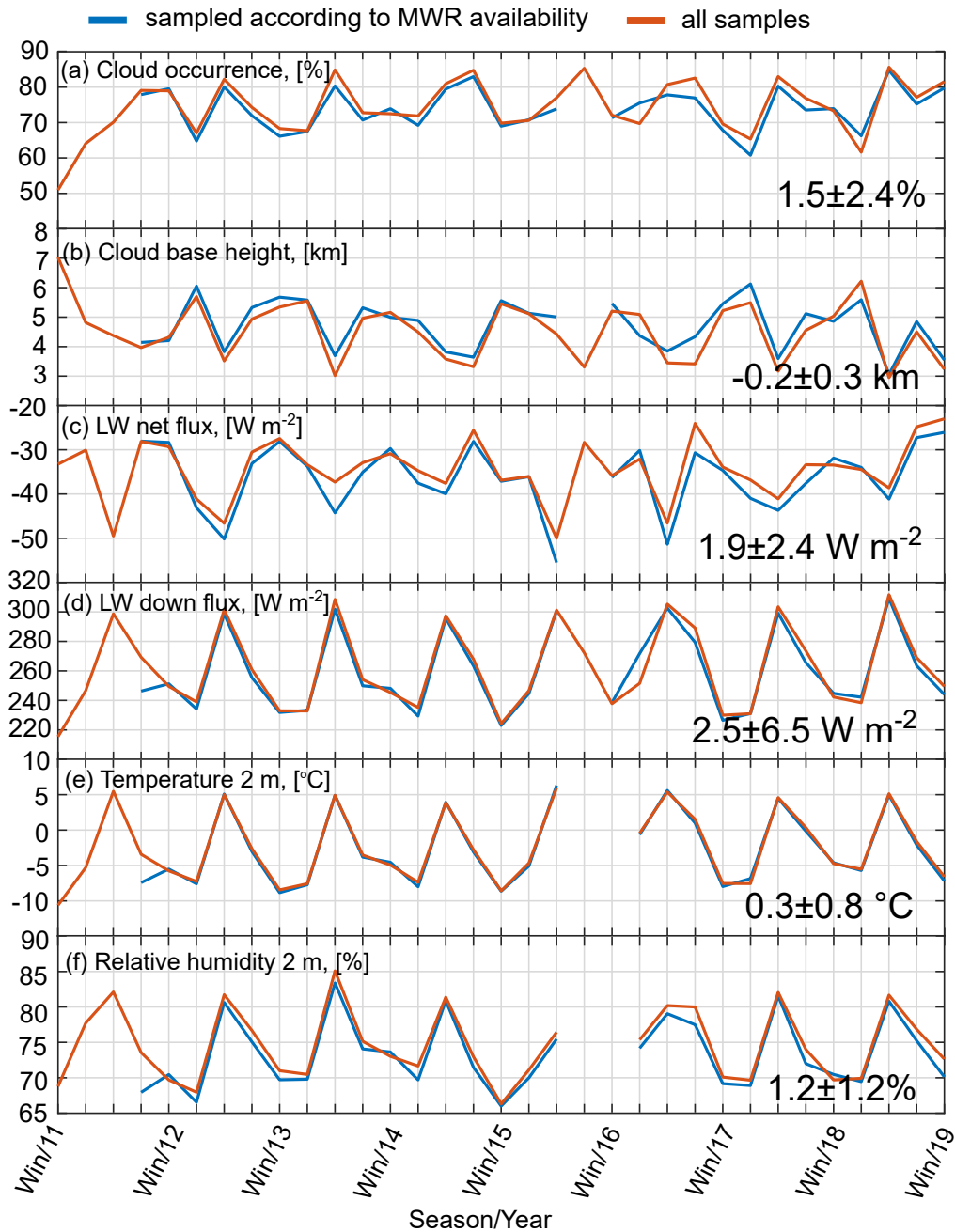
Figure 5.4: Input parameters used for the neural networks based on availability of MWR radiometer data (blue lines) and all samples (red lines). The values in the right lower angle in each panel indicate mean and $\pm$ standard deviation of the difference (all minus MWR).

As it is shown in Table 5.2 the neural networks use different sets of input parameters and, thus, are subject to different sampling effects described above. Therefore, in order to evaluate uncertainties in estimated LW CRE related to the three sampling aspects, all the trained neural networks were applied to the period from 1 December 2011 to 30 Nov 2018. During this period data for all 9 neural networks are available (see Table 5.6). Neural networks 1–5 require MWR data and thus are not applied to samples with liquid precipitation or scans. In contrast, neural networks 6–9 use only ceilometer and BSRN data and are applied to samples including liquid precipitation. Note, that within this work, no algorithm was applied to ceilometer
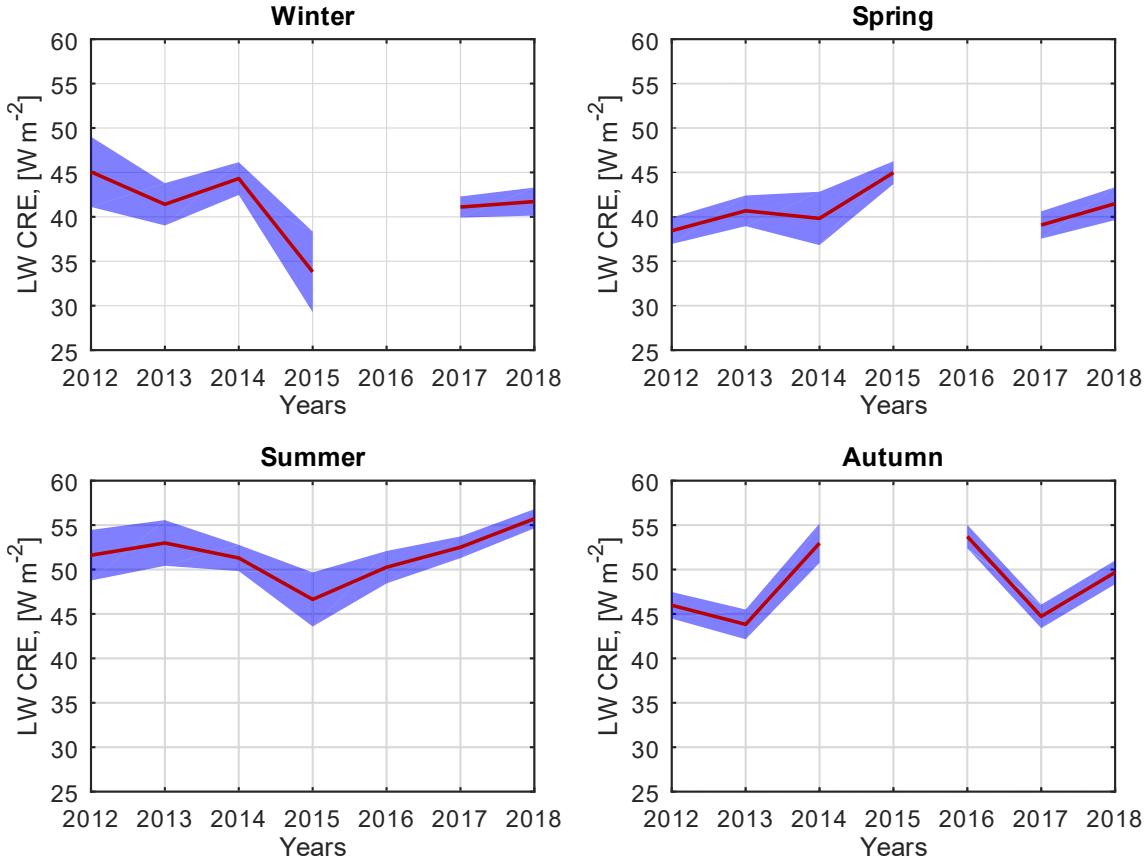
Figure 5.5: LW CRE estimated by all 9 neural networks for different seasons for the period from December 2011 to December 2018. The red lines show LW CRE averaged over the seasonal LW CRE obtained with the neural networks. The blue shaded areas correspond to ± one standard deviation. Only seasons with valid inputs for all the neural networks are shown.

data to identify precipitating samples in order to improve the performance of neural networks. The range of LW CRE outputs from the 9 neural networks is used as a proxy for the sampling uncertainty. Figure 5.5 shows the ensemble-averaged LW CRE estimated from all the neural networks for different seasons. A standard deviation calculated using all seasons and years was found to be 2 ± 0.9 W m^{-2}. This value is further used as the uncertainty σ_{smp} related to the sampling effects.

Assuming that the uncertainties due to modeling of the surface LW net flux σ_m by the RRTMG and the sampling aspects σ_{smp} are uncorrelated, the resulting uncertainty σ_Σ of the LW CRE retrieved with neural networks and averaged over one season is estimated as follows:

$$\sigma_\Sigma = \sqrt{\sigma_m^2 + \sigma_{smp}^2}. \tag{5.14}$$

Taking into account that $\sigma_m \approx 5$ W m^{-2} and $\sigma_{smp} \approx 2$ W m^{-2}, σ_Σ is equal to 5.4 W m^{-2}.

Table 5.6: Availability of variables for LW CRE estimation with neural networks.

Variable	Instrument	Availability	Neural networks
TBs and TBPC	MWR	8 Nov 2011 to 31 Dec 2018	1–5
Cloud fraction cloud base height	Ceilometers LD-40 and CL51	14 Jul 1998 to 31 Dec 2018	3–7
Q_{LW} and $F_{\downarrow LW}$	BSRN	2 Aug 1992 to 31 Dec 2018	4–9
2 m temperature relative humidity	BSRN	1 Aug 1993 to 31 Dec 2018	7 and 9

5.3 Trends in CRE and their relation to occurrence of anomalous conditions

According to Table 5.6, for the estimation of LW CRE over the last 25 years, observations from BSRN and ceilometers have to be used. Therefore, in order to check the long-term LW CRE for trends only neural networks 6–9 are applied. Figure 5.6 shows LW CRE averaged over 3 month periods (further denoted as season-averaged LW CRE). All 4 neural networks show similar patterns in the time series of the season-averaged LW CRE. For the periods when all 4 neural networks have valid input variables, the spread among the outputs of the neural networks was checked. For each period the standard deviation of the season-averaged LW CRE from the 4 neural networks was calculated. The spread was characterized as an average of these standard deviations over the whole analyzed period. The spread was calculated separately for winter, spring, summer, and autumn and was found to be 5.5, 4.9, 3.0, and 5.1 W m^{-2}, respectively. This spread is about a factor of two higher than the uncertainty σ_{smp} associated with sampling found for the period from 2011 to 2018 in the previous section. Nevertheless, according to Eq. 5.14, the higher deviation causes 1.4 W m^{-2} increase in the resulting uncertainty σ_Σ and does not strongly affects the results shown further.

As it was shown in Sec. 2.1 ceilometer observations at Ny-Ålesund started in 1992. Nevertheless, the ceilometer LD-WHX05 operated at Ny-Ålesund had different specifications and showed cloud observations inconsistent with respect to ceilometers LD-40 and CL51 (Maturilli and Ebell, 2018). Therefore, the neural networks 6 and 7 are only applicable from the summer 1998, when the ceilometer LD-40 was set up at Ny-Ålesund. Thus, the largest time coverage in the LW CRE estimation is provided by the neural networks 8 and 9. Since outputs of the neural networks 8 and 9 differ, their average is taken as a best estimate of the LW CRE. Using this average, a linear fit was found for different seasons (shown by solid black lines in Fig. 5.6). According to the two-sided t-test, LW CRE has trends in winter and autumn with a confidence exceeding 95%. The found trends are 3.4 and 2.2 W m^{-2} decade^{-1} in winter and autumn, respectively. In summer, there is a negative trend of –1.8 W m^{-2} decade^{-1} with a confidence level of 0.94. For the spring season, no significant trends was found. Thus, the LW surface warming by clouds at Ny-Ålesund has been increasing
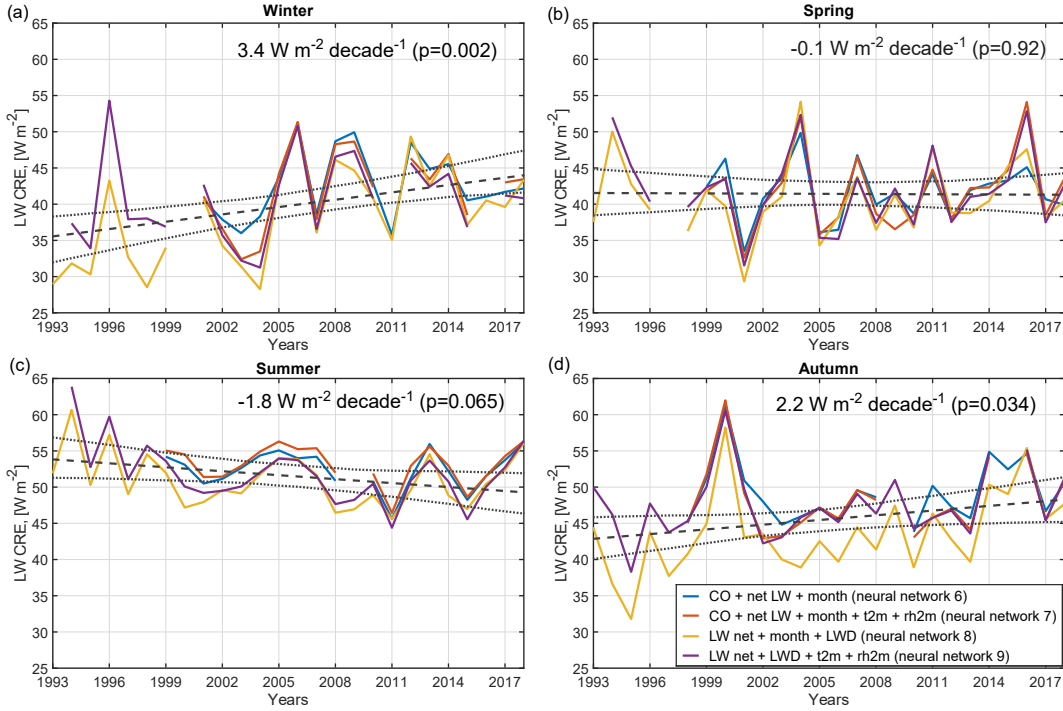
Figure 5.6: Time series of season-averaged LW CRE estimated with neural networks 6–9 for the period 1993–2018. The black dashed lines show linear fits of the average output from the neural networks 8 and 9. The black dotted lines show the 95th confident intervals for the fits derived by the bootstrapping resampling method. The numbers in the upper right corners in each panel indicate slopes of the fit. The p-value of the two-sided significance t-test is shown in brackets.

for the winter and autumn seasons over the last 25 years. At the same time, it is likely that the LW cloud-induced surface warming has been decreasing for the summer season.

The found trends in LW CRE could be caused by a change in a number of cloud properties listed in Sec. 1.4. Since, as it is shown in Sec. 1.2, the cloud properties at Ny-Ålesund might be influenced by the thermodynamic state of the atmosphere and long-distance air transport, the changes in LW CRE may be associated with the trends in the occurrence of the atmospheric anomalies discussed in Sec. 4.5. In order to relate the retrieved LW CRE to normal and anomalous conditions, for each radiosonde from 1993 to 2018, the IWV was calculated and the profile was classified using the thresholds specified in Sec. 4.1. An average of 10-min LW CRE samples from the neural networks 8 and 9 was calculated (CRE_{8+9}). For samples with a single output either from the neural network 8 or 9 this output is taken as a sample of CRE_{8+9} in order to increase the availability of the LW CRE estimate. For each radiosonde CRE_{8+9} was averaged over ± 1 hour from the radiosonde launch time.

In order to check how the sampling around radiosonde launches influences CRE_{8+9}, season-averaged CRE_{8+9} using all samples and samples ± 1 hour from the radiosonde launch time were calculated. The results depicted in Fig. 5.7 show that the difference due to the sampling is 1.8 ± 2.8 W m^{-2}. The largest difference of 13 W m^{-2} was found for winter 1996, when in addition to regular radiosondes launched at around
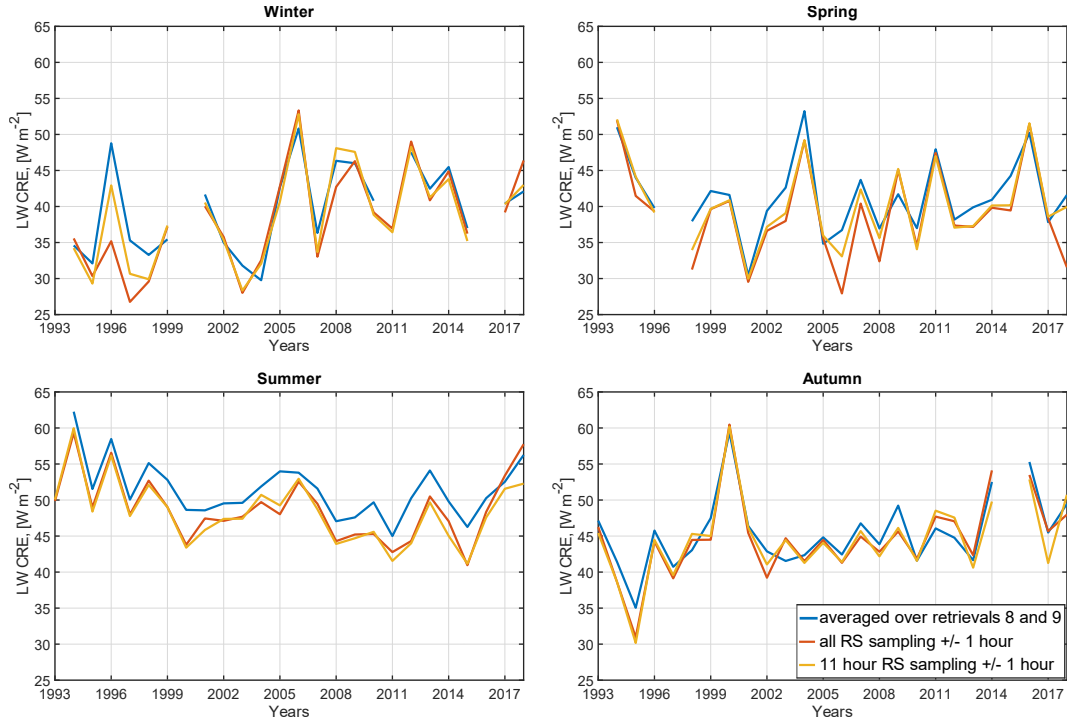
Figure 5.7: Time series of season-averaged CRE_{8+9} calculated using all valid samples (blue line), all valid samples within ± 1 hour from all radiosonde launches (red line), and all valid samples within ± 1 hour from 11 UTC radiosonde launches (yellow line).

11 and 23 UTC, 1 to 3 radiosondes on some days were launched. In the case only 11 UTC radiosondes are taken for the sampling, the difference in winter 1996 is less than 5 W m^{-2}. This indicates that the additional radiosondes were probably launched within a measurement campaign focused on clear-sky conditions. Since the large difference was only found for a few cases, all the radiosondes were used for the following analysis (red line in Fig. 5.7).

As it was shown in Sec. 4.2, moist (dry) anomalies are related to higher (lower) cloud occurrence, LWP, and IWP and, as a result, higher (lower) LW CRE with respect to normal conditions. In order to understand the contribution of different conditions to LW CRE, the season-averaged CRE_{8+9} found for normal and anomalous conditions was weighted by the occurrence of the corresponding conditions (Fig. 4.8). The results are shown in Fig. 5.8. As expected, a major part of LW CRE is defined by normal conditions since their occurrence is the highest. Even though the occurrence of moist anomalies is 7–11 times smaller than the occurrence of normal conditions, the contribution of moist anomalies to LW CRE is about 20–30% of the contribution of the normal conditions. The contribution of the dry anomalies to the absolute value of the LW CRE is mostly below 10 W m^{-2}. Nevertheless, this does not mean that dry conditions are not important for LW CRE. The higher the occurrence of the dry anomalies, the lower the occurrence of normal and/or moist conditions, and, in turn, the lower the resulting LW CRE. Before the early 2000s, the contributions of moist and dry conditions were about the same, which is possible when the occurrence of the moist anomalies is much lower than the occurrence of dry anomalies. After 2005 the contribution of moist anomalies is higher for all seasons because the occurrence
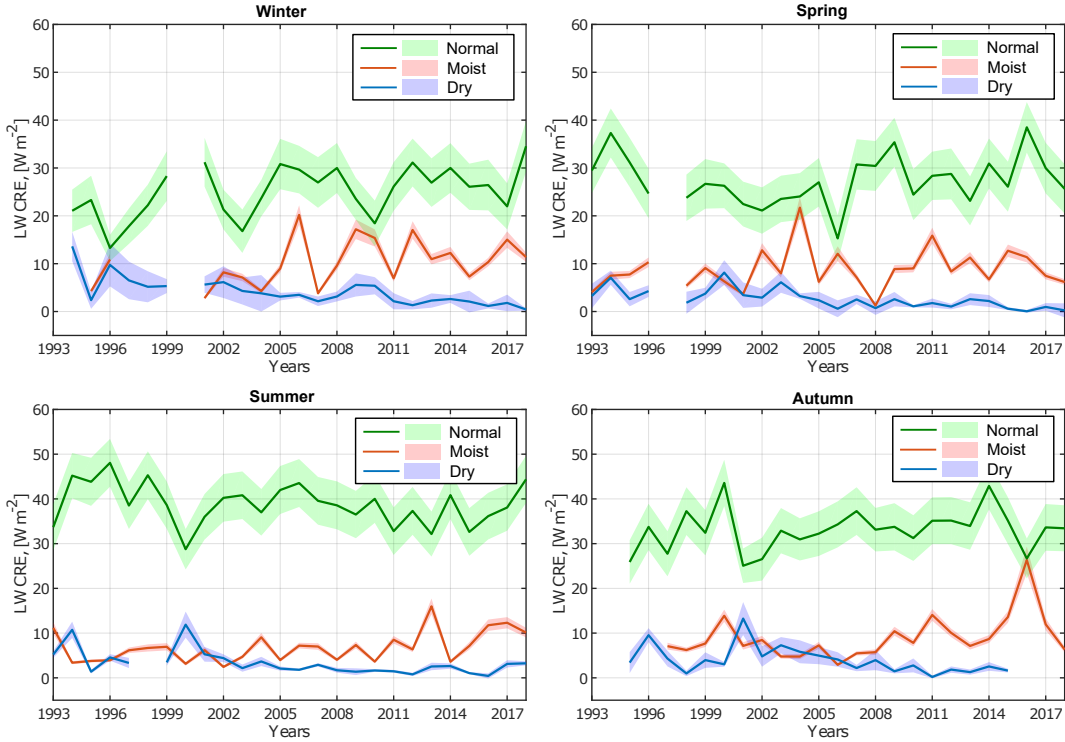
Figure 5.8: Time series of the seasonal CRE_{8+9} averaged for normal (green solid line), moist (red solid line), and dry (blue solid line) cases multiplied by the occurrence of the corresponding type of conditions. The shaded areas correspond to the uncertainty estimated as $\pm\sigma_\Sigma$ weighted by the occurrence of the corresponding type of conditions. The information on the condition types is derived from radiosondes.

of moist anomalies tends to increase in time.

Trends in occurrences of different conditions at Ny-Ålesund may be related to trends in LW CRE. For instance, the positive trends in the occurrence of moist anomalies and the negative trends in the occurrence of dry anomalies in winter and autumn found in Sec. 4.5 could explain the LW CRE trends in these seasons. Nevertheless, cloud properties typical for normal and anomalous conditions could have also changed over 25 years. Therefore, season-averaged CRE_{8+9} for normal and anomalous conditions need to be checked for trends. Figure 5.9 shows that in winter and autumn there are no significant trends in season-averaged CRE_{8+9} for different conditions. In spring, there is a significant trend of –5.3 W m^{-2} decade^{-1} for dry conditions. In summer, the season-averaged CRE_{8+9} is likely (90% confidence level) to have a trend of –2.7 W m^{-2} decade^{-1} under normal conditions. These results show, that LW radiative properties of clouds for different conditions have not significantly changed over the last 25 years except for dry conditions in spring and normal condition in summer. Therefore, the largest trends in LW CRE observed in winter and autumn are mostly defined by the changes in occurrence of the normal and anomalous conditions. In spring, the negative trend in the LW CRE during the dry conditions is counteracted by the increased occurrence of normal conditions, having higher typical LW CRE and, thus, the resulting LW CRE in spring shows no significant trend (Fig. 5.6). In summer the negative trend in LW CRE during normal conditions agrees with the trend in LW CRE shown in Fig. 5.6, taking into
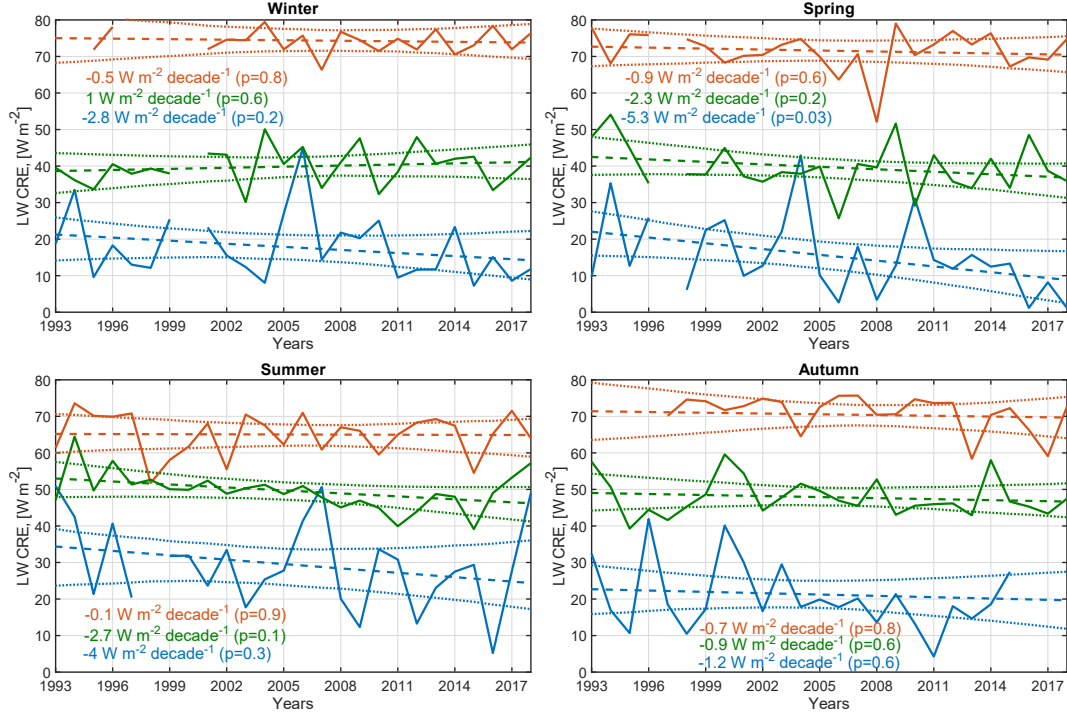
Figure 5.9: Time series of seasonal CRE_{8+9} calculated for normal (green solid line), moist (red solid line), and dry (blue solid line) conditions. The dashed lines show linear fits. The colored numbers show trends with p-values of the two-sided t-test given in brackets. The color of the text indicates the type of conditions. The dotted lines correspond to the 95% confidence intervals for the linear fits derived using the bootstrapping approach. The information on the condition types is derived from radiosondes.

account that the occurrence of the normal conditions is relatively constant and is about 75% (Fig. 4.8).

Since trends in LW CRE are mostly defined by the occurrence of normal and anomalous conditions in winter and autumn, the season-averaged LW CRE can be parameterized as follows:

$$\mathrm{CRE}_{LW,w} = (F_w)_n(\mathrm{CRE}_{LW,w})_n + (F_w)_m(\mathrm{CRE}_{LW,w})_m + (F_w)_d(\mathrm{CRE}_{LW,w})_d, \quad (5.15)$$

$$\mathrm{CRE}_{LW,a} = (F_a)_n(\mathrm{CRE}_{LW,a})_n + (F_a)_m(\mathrm{CRE}_{LW,a})_m + (F_a)_d(\mathrm{CRE}_{LW,a})_d, \quad (5.16)$$

where w and a denote winter and autumn, respectively; $(F)_n$, $(F)_m$, and $(F)_d$ are frequency of occurrence of normal, moist, and dry conditions, respectively; $(\mathrm{CRE}_{LW})_n$, $(\mathrm{CRE}_{LW})_m$, and $(\mathrm{CRE}_{LW})_d$ are typical values of LW CRE for normal, moist, and dry conditions. A comparison of the parametrization given in Eqs. 5.15-5.16 with the season-averaged LW CRE using all available samples show a difference of 1.1 ± 4.4 W m^{-2} and the correlation of 0.69. A similar parameterization for summer gives 0 correlation because, as it was previously mentioned, the trend in LW CRE in summer is defined by the trend of LW CRE for normal conditions.

Table 5.7: Typical values of LW CRE for normal, moist, and dry conditions for the parameterizations in Eqs. 5.15 and 5.16. The values are given in [W m^{-2}].

Condition type	Winter	Autumn
Normal	40	48
Moist	74	71
Dry	18	21

5.4   Summary and conclusions

In this chapter a novel set of retrievals for the estimation of LW CRE at Ny-Ålesund was developed. The retrievals are based on the neural network approach and use ground-based observations in order to approximate LW CRE. A comparison of the retrievals revealed that neural networks using only MWR and ceilometer observations as the input could not fully reproduce the variability of the LW CRE simulated with RRTMG. The neural networks using surface radiation measurements in addition performed much better and yield near 0 W m^{-2} bias and a correlation of about 0.8 with respect to the LW CRE from RRTMG. The evaluation of the neural networks showed that the seasonal LW CRE calculated as an ensemble average has the uncertainty in the order of 6 W m^{-2}.

Two neural networks only require measurements from BSRN which are available for about 25 years. Analysis of the LW CRE estimated with these neural networks showed positive trends of 3.4 and 2.2 W m^{-2} decade^{-1} in winter and autumn, respectively, with more than 95% confidence. In summer LW CRE exhibit a negative trend of –1.8 W m^{-2} decade^{-1} with the confidence level of 94%. There were no significant trends found in spring.

As expected, normal conditions are the major contributor to the LW CRE, since their occurrence is the highest with respect to dry and moist anomalies. Even though the occurrence of moist anomalies is typically a factor of 7–11 lower that the one of normal conditions, the contribution of moist anomalies to LW CRE reaches 20-30% of the contribution from normal conditions. In some seasons, e.g. winter 2010, spring 2004, and autumn 2016, the contribution of normal and moist conditions is almost the same. Since dry conditions are mostly associated with clear-conditions their contribution to the season-average LW CRE is defined by limiting the occurrence of normal and moist conditions. For instance, a high occurrence of dry anomalies leads to relatively low occurrence of normal and/or moist conditions, and, thus, the LW CRE would be relatively low in this case.

The analysis of season-averaged LW CRE during different atmospheric conditions over the last 25 years shows that there are no significant trends except for dry conditions in spring and normal conditions in summer with –5.3 and –2.7 W m^{-2} decade^{-1} trends, respectively. The absence of trends indicates that radiative properties of clouds during normal, moist, and dry anomalies have been the same, while the significant trends found in summer and spring show that cloud properties have changed.

The largest trends in LW CRE found in winter and autumn are likely to be caused by changes in occurrence of moist and dry conditions. The found negative trend

in occurrence of dry anomalies in spring (see Fig. 4.8) is associated with increasing occurrence of normal and moist conditions. This redistribution of the thermodynamic conditions should in general increase the LW CRE, because cloud properties are enhanced during moist and normal conditions at Ny-Ålesund. Nevertheless, it was found that the estimated LW CRE shows no significant trend in spring. The analysis of the dry anomalies in spring shows that LW CRE exhibits a significant negative trend which compensates the expected increase in LW CRE.

The trend in summer is mostly caused by changes in LW CRE under normal conditions. The analysis performed within this study cannot explain the nature of the changes in cloud properties under normal conditions in summer and dry conditions in spring and, therefore, this topic should be further investigated.

For winter and autumn, which are the seasons with the fastest surface temperature growth rate at Ny-Ålesund (Maturilli et al., 2015), the seasonal LW CRE over the last 25 years can be parameterized as a linear combination of the occurrences of normal, moist, and dry conditions weighted by LW CRE typical for these conditions. Taking into account, that in winter and autumn the contribution of SW CRE to the net CRE is small, these parameterizations can be also used for the net CRE.

A potential application of the results obtained in this chapter is an evaluation of the surface CRE estimated from models. Zygmuntowska et al. (2012) showed issues in the evaluation of the ERA-Interim reanalysis model associated with uncertainties in active and passive satellite observations in the Arctic area. Major difficulties are related to low-level cloud observations from space. A number of studies, therefore, evaluate CRE from the reanalysis models in the Arctic area based on observations gathered at Barrow (Walsh et al., 2009) and during the SHEBA campaign (Engström et al., 2014). The long-term estimate of LW CRE at Ny-Ålesund can be used for a similar analysis.

Chapter 6

Summary and outlook

Clouds are one of the least understood atmospheric components affecting the climate and the water cycle in the Arctic region experiencing rapid warming during the last decades. The exact role of clouds in the complex interactions between different components of the Arctic environment is not clearly understood and a large effort is put towards a better representation of cloud related effects in climate and numerical weather prediction models. It is known that the Arctic climate is susceptible to long-distance air transportation from the mid-latitudes. There is an evidence that the periodical intrusions of relatively warm and moist air from the North Atlantic or cold and dry air from the North pole area modulate the atmospheric state including the amount of water vapor and cloud properties. A quantitative characterization of the relations between the air transport patterns and cloud properties at the Arctic stations has become a topic of recent studies (e.g. Gallagher et al., 2018). Improvements and evaluations of modeled cloud-related processes require accurate long-term observations of cloud microphysical and radiative properties.

Since more than few decades ago, ground-based remote instruments have shown their value for investigations of Arctic clouds. A set of instruments including but not limited to a cloud radar, a lidar, and a microwave radiometer can be used for detection and profiling of clouds. Even though, ground-based remote sensors do not provide a global or regional view on clouds, they deliver a unique continuous dataset with high temporal and spatial resolution, which can be obtained by no other means. A combined analysis of observations for these instruments allows for a classification and a quantitative characterization of cloud properties. Profiles of cloud properties obtained with state-of-the-art retrievals can be used as an input for modern radiative transfer models in order to estimate the contribution of clouds in the Arctic warming, which is currently one of the hot topics in atmospheric research.

Until recently only few Arctic sites mostly located in the western hemisphere were equipped with sets of cloud radars, lidars, and microwave radiometers and provided a continuous multi-year characterization of macrophysical, microphyscal, and radiative properties of clouds. In June 2016 the French-German Arctic research station AWIPEV situated in Ny-Ålesund, Norway, was complemented with a W-band cloud radar by the University of Cologne within the (AC)^3 project and, thus, the AWIPEW station became one of the sites capable of state-of-the-art cloud observations in the Arctic. Ny-Ålesund is located in the Arctic area with the fastest surface warming rate, which attracts the focus of many climate research groups. The climate at Ny-

Ålesund, and in the Svalbard area in general is complex and affected by multiple factors, among which are ocean-atmosphere-land heat interaction, advection from mid-latitudes, and orographic effects.

This study analyzes statistics of clouds from two and a half year of observations at Ny-Ålesund. In the first part of this thesis, a detailed range resolved information about cloud particles was obtained based on a categorization of atmospheric scatterers from the widely used Cloudnet processing algorithm and state-of-the-art microphysical retrievals. Addressing Question 1 from Sec. 1.7 (*What characteristics do clouds have at Ny-Ålesund?*), based on cloud observations from June 2016 to July 2017 the total occurrence of clouds was found to be ∼81%. Most of the liquid and ice hydrometeors occur in the lowest 2 km. Single layer clouds occur 36% of the time with 21, 9, and 6% of mixed-phase, ice, and liquid clouds, respectively. About 45% of profiles contained several cloud layers, but due to limitations in multi layer cloud observations a reliable classification and characterization of these profiles is mostly not possible. Single layer mixed-phase and liquid clouds have median LWP values of 17 and 37 g m^{-2}, respectively. The low LWP values are consistent with observations at other Arctic sites. Liquid phase was detected at temperatures down to –40°C with the highest occurrence at cloud top temperatures from –15 to 0°C. Median values of IWP in ice-containing clouds are about 15–20 g m^{-2}.

The derived cloud properties were related to in-cloud thermodynamic properties and compared to those estimated by the numerical weather prediction model ICON for Ny-Ålesund. Answering Question 2 (*How good can a numerical weather prediction model represent cloud properties at Ny-Ålesund?*), the comparison shows large differences in phase partitioning at different ambient temperatures between the NWP ICON model and observations, especially for mixed-phase clouds. In the observations, most of the liquid occurs at temperatures between –25 to 10°C, while in the NWP ICON model liquid phase is concentrated in the range from –10 to 5°C. This difference results in a large difference between observed and modeled single-layer ice and mixed-phase clouds. Due to the lower occurrence of liquid phase at temperatures below –5°C modeled clouds are often erroneously classified as pure ice. Thus, the model overestimates the occurrence of single layer ice clouds and underestimates the occurrence of mixed-phase clouds. An improvement in modeling of mixed-phase clouds requires better understanding of their life cycle, which is defined by a large number of processes including heterogeneous ice formation, air dynamics, and phase transitions. In order to characterize these processes more accurately, precise profiles of aerosols and in-cloud properties such as relative humidity, up- and downdrafts are needed. Profiling of the parameters may be based on the advanced instrumentation such as multiwavelength and Doppler lidars, and differential absorption radars.

It is well known, that the climate in the Svalbard region where Ny-Ålesund is located is strongly influenced by long-range air transport. Relatively warm and moist air typically comes from the North Atlantic area, while dry and cold air circulates in the Arctic region. These air masses are often associated with anomalous atmospheric conditions at Ny-Ålesund and are related to distinct macro and microphysical properties of clouds and their radiative effect. The classification of atmospheric conditions was based on the 8-year reference dataset of IWV from MWR. Periods when IWV exceeded the 90th percentile for a certain season were considered as moist, while cases with IWV below the 10th percentile were classified as dry. A large part

of moist(dry) anomalies were accompanied by an increase(decrease) in the atmospheric temperature. The analysis of the 6-day backward FLEXTRA trajectories agrees well with the previous studies and shows that most of the moist anomalies are related to air masses coming from the North Atlantic. Dry anomalies were mostly associated with the air from the North. In order to quantitatively estimate an impact of the anomalous conditions on clouds at Ny-Ålesund, a number of cloud properties were related to normal, moist, and dry conditions. Addressing Question 3 (*How do moist and dry conditions influence cloud properties including occurrence, cloud types, IWP, and LWP at Ny-Ålesund?*), for the period from June 2016 to October 2018 anomalous water vapor conditions were found to strongly affect macrophysical and microphysical properties of clouds. Dry anomalies are related to about 30% less cloud occurrence with respect to normal conditions. In contrast, during moist conditions the cloud occurrence typically reaches 90–99%. Excess and shortage in water vapor drastically affects LWP and IWP. In winter and spring, moist conditions are associated with a factor of 2–3 higher values in LWP and IWP relative to normal conditions, while dry cases lead to a reduction of these parameters by an order of magnitude. In summer, IWP and LWP shows similar relations to the anomalies but the magnitude of the changes is smaller than in winter and spring. In autumn, both moist and dry anomalies lead to an increase in LWP and IWP. In general, directions of the changes in macro- and microphysical cloud properties are as expected. Clouds are likely to form in profiles with relatively high IWV. Nevertheless, the magnitude of the changes is hard to explain from IWV alone. In order to better understand the cloud response to the water vapor anomalies, the cloud properties should be further related to vertical profiles of humidity. The humidity profile estimates can be improved by an analysis of passive observations at 183, 225, and 340 GHz from the Low HUMidity PROfiler (LHUMPRO), which was operated at the AWIPEV station for a limited time period at Ny-Ålesund within the (AC)^3 project.

Within the (AC)^3 project, microphysical properties of clouds retrieved within this study were used by Ebell et al. (2020) in order to run a radiative transfer model and to estimate radiative properties of clouds. Within this thesis CRE, which is one of the outputs of the model, was related to different conditions at Ny-Ålesund. Answering Question 4 (*How do changes in cloud properties due to moist and dry conditions influence CRE at Ny-Ålesund?*), the distinct cloud properties during dry and moist conditions at Ny-Ålesund lead to noticeable differences in CRE. Dry anomalies are associated with lower cloud related surface SW cooling relative to normal conditions. In spring and summer the changes are 19 and 67 W m^{-2}, respectively. These changes result from lower cloud occurrence and LWP typical for dry conditions. In contrast, enhanced cloud properties during moist conditions are related to the SW cloud related cooling of the surface increased by 25 W m^{-2} relative to normal cases. On average, LW CRE was found to be lower by 11–35 W m^{-2} during dry anomalies, while the moist conditions enhanced LW CRE by about 30 W m^{-2} with respect to normal conditions. In seasons when the sun is low the net CRE is dominated by LW CRE. During these periods moist anomalies are associated with enhanced cloud properties and, therefore, cause more cloud related surface warming at Ny-Ålesund. In contrast, dry anomalies are typically related to much lower cloud fraction, and, thus reduce the surface warming due to clouds with respect to normal conditions. In summer, SW CRE becomes dominant and moist conditions cause stronger surface cooling relative to normal cases, while dry conditions tend to reduce the cloud

related surface cooling.

Radiosondes routinely launched at Ny-Ålesund since 1993 allow for answering Question 5 (*Do long-term observations of the atmospheric state at Ny-Ålesund show significant trends in the occurrence of moist and dry conditions over the last decades?*). Moist anomalies show significant positive trends varying for different seasons from 2.8 to 6.4% decade^{-1}. In contrast, the occurrence of dry anomalies has been declining at rates from -12.9 to -4% decade^{-1}. Since the anomalies are related to certain patterns in cloud properties and CRE, the long-term trends in the anomaly occurrences may have lead to stronger cloud related surface cooling in summer and warming in other seasons.

The analyzed period from June 2016 to October 2018 is relatively short with respect to the vast observations having been performed at Ny-Ålesund for more than two decades. The surface radiation measurements having been run since August 1992 provide a long-term dataset which reveals trends in longwave and shortwave radiation. Nevertheless, this dataset does not provide an information on the cloud contribution to these trends. A number of recent studies have shown that the neural networks can be used in order to estimate LW CRE. In this thesis this approach is used to extend the LW CRE estimated by the radiative transfer model for the analyzed period to 25 years of surface radiation observations at Ny-Ålesund. The cloud observations taken within the $(AC)^3$ project play a key role for this extension. LW CRE estimated by the radiative transfer model is used for its approximation from a number of variables having been measured for long time, such as LW down-welling and net radiation, 2 m temperature and relative humidity etc. This approximation is made by means of neural networks. In total 9 neural networks estimating LW CRE and using different sets of input parameters were trained. Two neural networks use data from MWR only as a input, another two require surface LW fluxes, temperature, and relative humidity, while the remaining neural networks use observations from MWR, ceilometer, and BSRN as the input. All the neural networks were applied to the 8-year period when observations from all instruments were available. The resulting ensemble of LW CRE was used to estimate the uncertainty of the neural network approach. The uncertainty of the season averaged LW CRE from the neural networks is estimated to be in the order of 6 W m^{-2}. The two neural networks that use BSRN measurements as the input were applied to the 25-year-long dataset for the estimation of the long-term LW CRE at Ny-Ålesund. Answering Question 6 (*If there are trends in the occurrence of moist and dry conditions at Ny-Ålesund, what is their impact on LW CRE?*), the analysis of LW CRE estimated with neural networks shows significant positive trends of 3.4 and 2.2 W m^{-2} decade^{-1} in winter and autumn, respectively. In summer, a negative trend of -1.8 W m^{-2} decade^{-1} was found, while no significant trends were found for the spring season. The analysis of LW CRE during different atmospheric conditions over the last 25 years revealed no significant trends except for dry conditions in spring and normal conditions in summer. Therefore, it is concluded that the trends in winter and autumn mainly result from changes in occurrence of normal and anomalous conditions, while the LW CRE trend in summer is mostly caused by changes in cloud properties during normal conditions. For winter and autumn seasons, which exhibit the fastest surface temperature changes at Ny-Ålesund, a parameterization of season-averaged LW CRE is proposed. This parameterization requires occurrences of normal, moist, and dry conditions, which can be obtained from radiosondes, MWR, or models. Since

the net CRE in winter and autumn are mostly defined by LW CRE, the parameterization can be used to characterize the cloud induced surface warming in these seasons at Ny-Ålesund.

The characterization of macro- and microphysical properties of clouds given in this study covers the time period from June 2016 to October 2018. In order to get more robust statistics and to analyze year-to-year cloud variability, long-term observations at Ny-Ålesund are required. Currently, the continuous atmospheric profiling is ongoing within the $(AC)^3$ project. Taking into account that Arctic clouds are characterized by low values of LWP, which are often within the accuracy of the MWR used in this study, future focus could be on improvement of LWP retrievals. These improvements can be based on considering passive observations at higher frequencies for the retrieval. For instance, the used cloud radar has an embedded passive channel operating at 89 GHz. This channel is more sensitive to liquid water in a column an can potentially improve the retrieval performance (Löhnert and Crewell, 2003). Marke et al. (2016) showed that additional passive infrared measurements also improve LWP estimate in comparison to the HATPRO retrieval, especially for clouds with low values of LWP. Such observations are available since summer 2019 at AWIPEV.

In order to provide more information on ice and mixed-phase clouds, which is valuable for improving the parameterization of these types of clouds in the existing numerical weather prediction models, a classification of ice particles is beneficial. Advanced ice classification methods require polarimetric (Myagkov et al., 2016) and multi-frequency (Kneifel et al., 2015) cloud radar observations. Therefore, the observations at the AWIPEV station are planned to be complemented with a polarimetric scanning Ka-band radar. In addition, an analysis of cloud radar Doppler information from cloud radars may potentially improve the phase partitioning in mixed-phase clouds (Luke et al., 2010) and retrievals of ice particle's size (Matrosov, 2011).

In this thesis, only integrated values of the water vapor in a column were analyzed. As a next step vertical distributions of the humidity and their relations to cloud properties should be analyzed, because the amount of water vapor is one of the key factors defining formation and development of cloud particles. In addition, the amount of water vapor and properties of clouds could be also related to a presence and strength of up and down-drafts in the atmosphere.
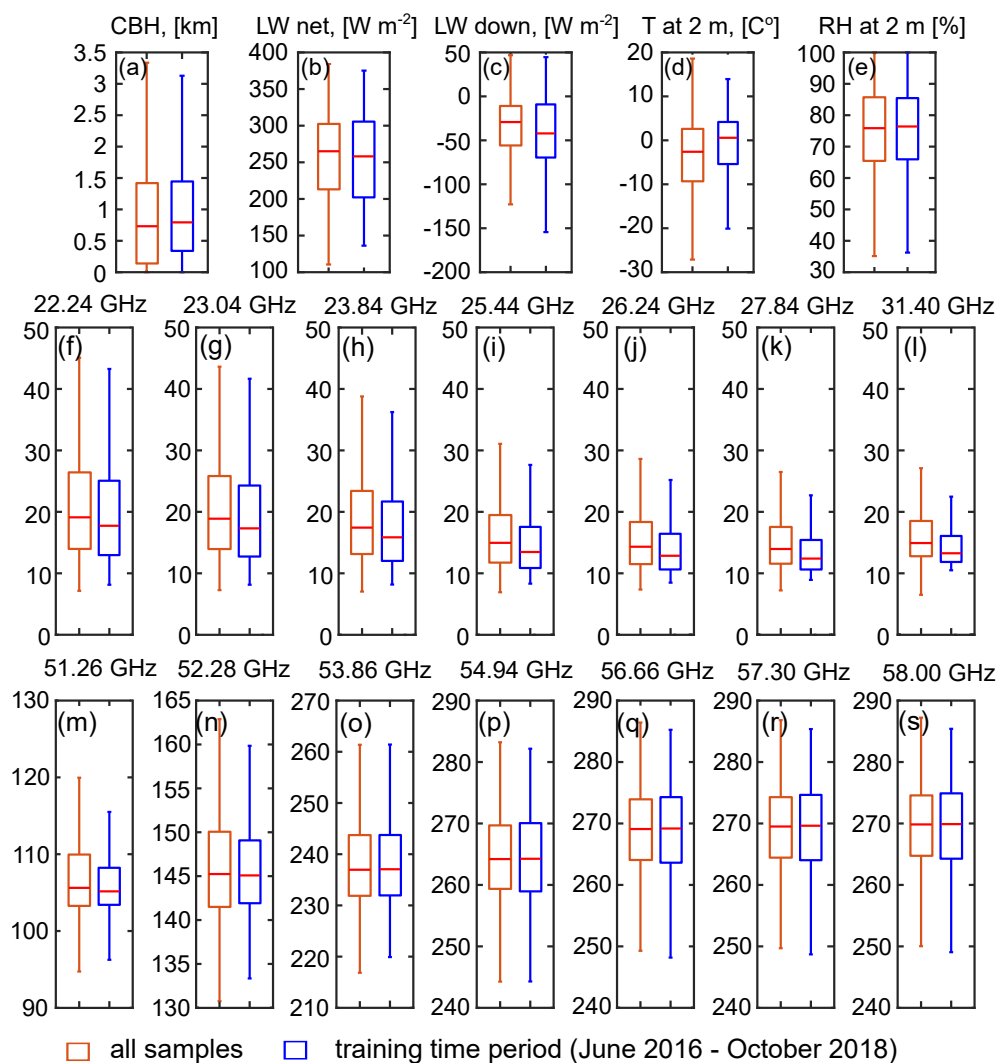
Appendix A

Figure A.1: Distributions of input parameters calculated from all available measurements (red boxplots) and those used for the trainings (blue boxplots). The input parameters for the trainings are simulated (see Sec. 5.1.1), except CBH (a), temperature (d) and relative humidity (e) at 2 m. The training period is from June 2016 to October 2018. Panels (f)-(s) show the distributions for TBs in [K]. The red horizontal bars inside the boxplots denote median values, the bottom and top of the edges of the boxes correspond to the 25th and 75th percentiles, respectively. The upper and lower whiskers indicate the 95th and 5th percentiles, respectively.
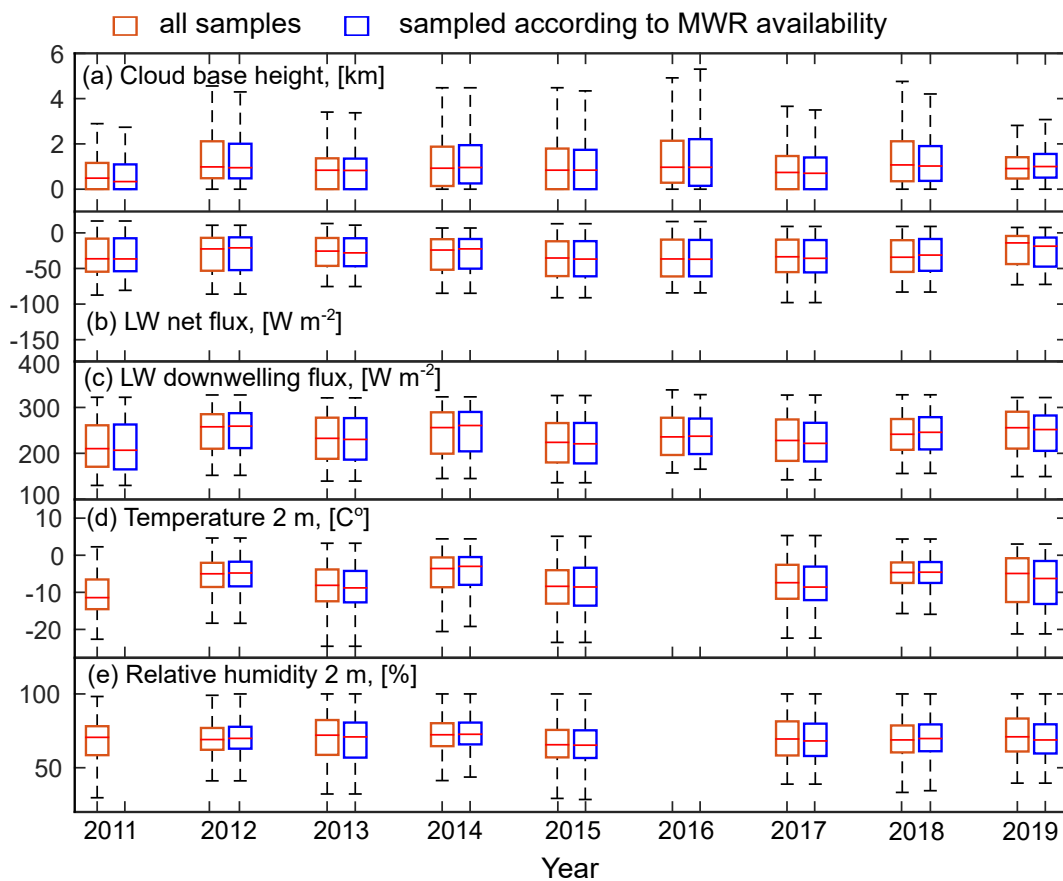
Appendix B

Figure B.1: Distributions of cloud base height (a), longwave net flux (b), longwave downwelling flux (c), temperature (d), and relative humidity (e) at 2 m averaged over winter seasons for all samples (red boxplots) and according to the MWR data availability (blue boxes). The red horizontal bars inside the boxplots denote median values. The bottom and top edges of the boxes correspond to 25th and 75th percentiles, respectively. The upper and lower whiskers indicate the 95th and 5th percentiles, respectively.
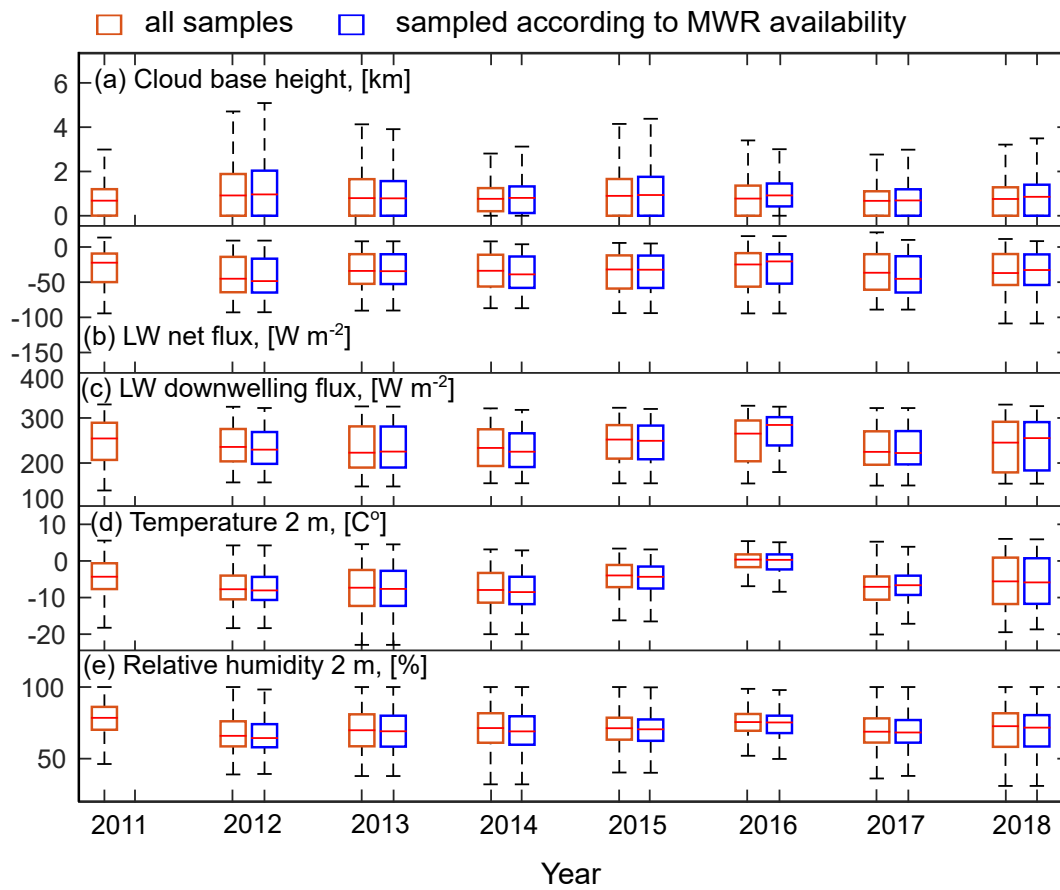
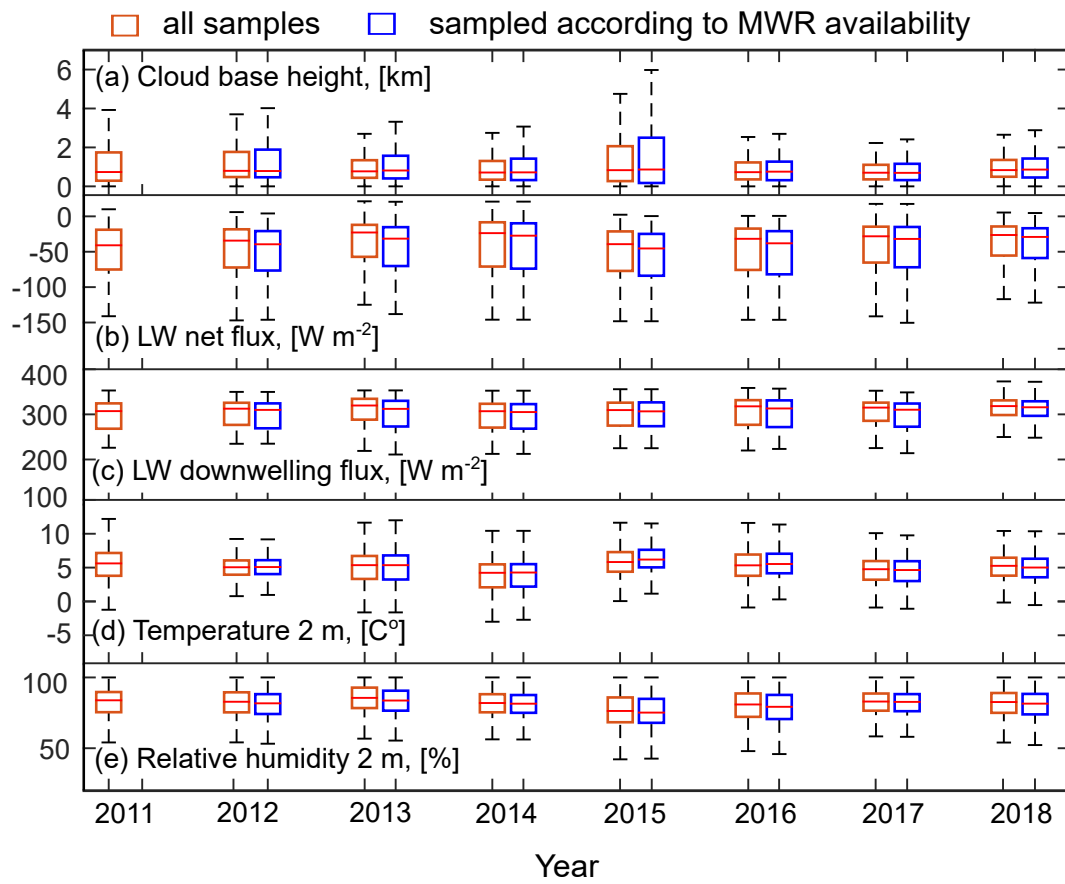Figure B.2: The same as Fig. B.1 but for spring periods.

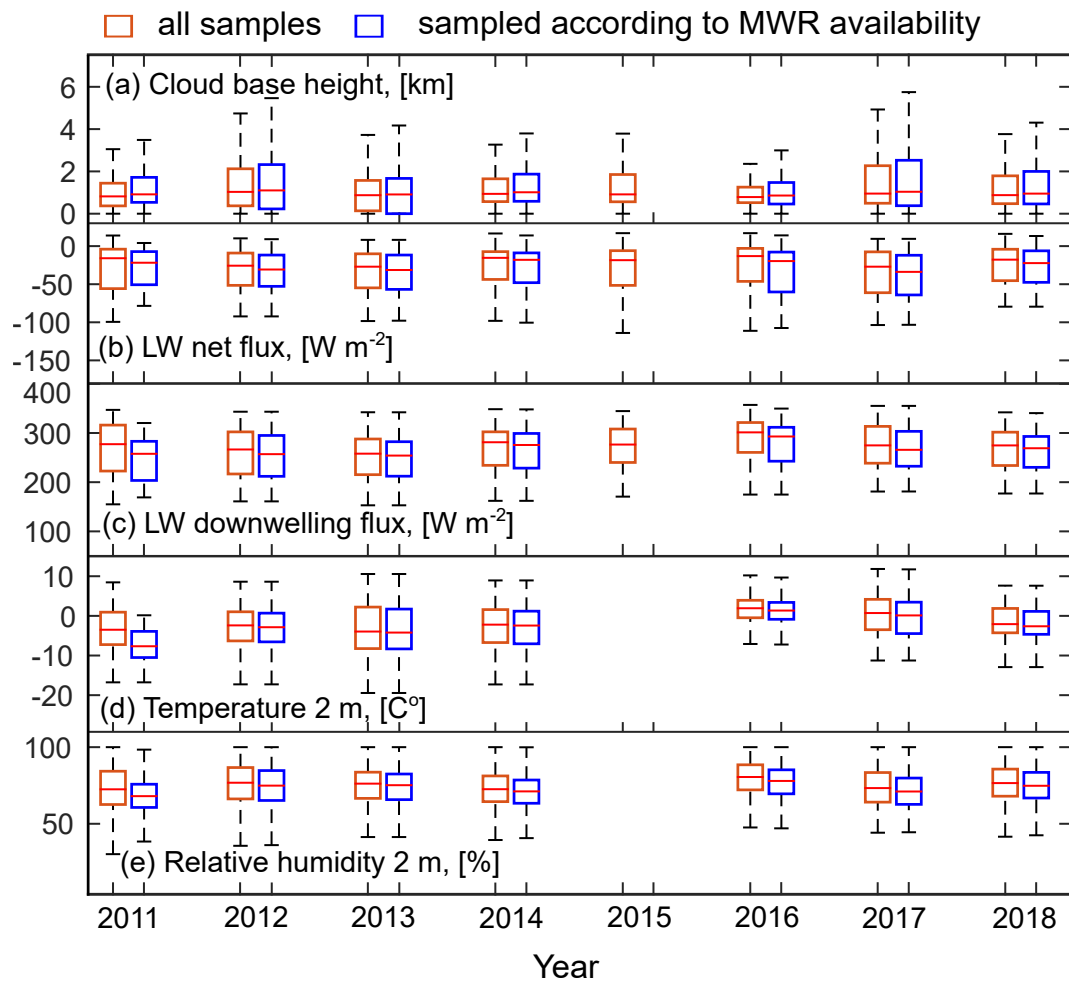Figure B.3: The same as Fig. B.1 but for summer periods.

Figure B.4: The same as Fig. B.1 but for autumn periods.

List of acronyms

ACLOUD	Arctic CLoud Observations Using airborne measurements during polar Day
ASCOS	Arctic Summer Cloud Ocean Study
AWIPEV	Alfred Wegener Institute Helmholtz Centre for Polar and Marine Research and the French Polar Institute Paul Emile Victor
$(AC)^3$	Arctic Amplification: Climate Relevant Atmospheric and Surface Processes, and Feedback Mechanisms
BSRN	Baseline Surface Radiation Network
CALIOP	Cloud-Aerosol Lidar with Orthogonal Polarization
CALIPSO	Cloud-Aerosol Lidar and Infrared Pathfinder Satellite Observations
CBH	Cloud Base Height
CCN	Cloud Condensation Nuclei
CERES	Clouds and Earth's Radiant Energy System
CMIP5	Coupled Model Intercomparison Project Phase 5
CRE	Cloud radiative effect
CWP	Cloud water path
DARDAR	liDAR-raDAR algorithm
DISORT	Discrete Ordinate Radiative Transfer
FMCW	Frequency Modulated Continuous Wave
FOC	Frequency of OCcurrence
EMCWF	European Centre for Medium Range Weather Forcast
EPOS	Earth Parameter and Orbit System Software (Ge et al., 2006)
GDAS	Global Data Assimilation System
GPS	Global Positioning System
GRUAN	Global Climate Observing System (GCOS) Reference Upper-Air Network
HATPRO	Humidity and Temperature profiler
JOYRAD-94	94 GHz cloud radar previously installed in JOYCE (Jülich ObservatorY for Cloud Evolution)
ICON	ICOsahedral Non-hydrostatic model (Zängl et al., 2015)
IN	Ice Nuclei
IWC	Ice Water Content

IWP	Ice Water Path
IWV	Integrated Water Vapor
LHUMPRO	Low HUMidity PROfiler
LMDZ5B	Atmospheric general circulation model of Laboratoire de Météorologie Dynamique (LMD), model with Zoom capacity
LW	Longwave
LWC	Liquid Water Content
LWF	Liquid Water Fraction
LWP	Liquid Water Path
MC	Multi-layer Clouds
MIRAC-A	Microwave Radar of Arctic Clouds Active remote sensing component
MODIS	MODerate-resolution Imaging Spectroradiometer
M-PACE	Mixed-Phase Arctic Cloud Experiment
MWR	Microwave Radiometer
NCEP	National Centers for Environmental Prediction
NWP	Numerical Weather Prediction model
PASCAL	Physical feedback of Arctic PBL, Sea ice, Cloud And AerosoL
PIR	Precision Infrared Radiometers
PSD	Particle Size Distribution
RMSE	Root-Mean-Squared Error
RPG	Radiometer Physics GmbH
RTM	Radiative Transfer Model
RRTMG	Rapid Radiative Transfer Model
SBDART	Santa Barbara Discrete Ordinate Radiative Transfer Atmospheric Radiative Transfer
SC	Single-layer Clouds
SHEBA	Surface Heat Budget of the Arctic Ocean
SIC	Single-layer Ice Clouds
SLC	Single-layer Liquid Clouds
SMC	Single-layer Mixed-phase Clouds
SW	Shortwave
SZA	Solar Zenith Angle
TB	Brightness Temperature
TBPC	Brightness Temperature on 3 Principle Components
TOA	Top Of Atmosphere

List of symbols

A	Surface area of an ice particle
$\mathbf{b}_1$, $\mathbf{b}_2$	Vectors with biases of for the hidden and output layers of the neural network
C	effective temperature/humidity lapse rate coefficient
C_a	radar constant related to radar specification
$\mathbf{C}_{TB}$	covariance matrix
$C_{i,j}$	elements of the covariance matrix with i and j indexes denote the different MWR channels
CO_2	carbon dioxide
CRE	surface net cloud radiative effect
CRE_{8+9}	surface longwave cloud radiative effect of averaged outputs of neural networks 8 and 9
CRE_{LW}	surface longwave cloud radiative effect
$CRE_{LW,a}$, $CRE_{LW,w}$	season-averaged surface longwave cloud radiative effect for autumn and winter
$(CRE_{LW})_d$, $(CRE_{LW})_m$, $(CRE_{LW})_n$	typical values of surface longwave cloud radiative effect for dry, moist and normal conditions
CRE_{SW}	surface shortwave cloud radiative effect
D	particle's size
e_w	water vapor pressure
E_d	sum of squared errors
E_w	sum of squared elements of the state vector
F	cost function
$(F)_d$, $(F)_m$, $(F)_n$	frequency of occurrence of dry, moist and normal conditions
$F_{\downarrow SW}$,$F_{\uparrow SW}$	surface downwelling / upwelling shortwave radiative fluxes
$F_{\downarrow LW}$,$F_{\uparrow LW}$	surface downwelling / upwelling longwave radiative fluxes
$F_{\downarrow clr,LW}$, $F_{\uparrow clr,LW}$	clear sky downwelling / upwelling longwave radiative flux
$F_{\downarrow clr,SW}$, $F_{\uparrow clr,SW}$	clear sky downwelling / upwelling shortwave radiative flux
$\mathbf{f}_1$, $\mathbf{f}_2$	transfer functions for the hidden and output layers of the neural network

$f_l(x)$	transfer function for the output layer of the neural network
$f_{ts}(x)$	transfer function for the hidden layer of the neural network
$\mathbf{J}$	Jacobian matrix
$\mathbf{H}$	Hessian matrix
h	altitude
h_{l1}, h_{l2}	altitudes of lower / upper boundaries of liquid containing cloud
h_{i1}, h_{il2}	altitudes of lower / upper boundaries of ice containing cloud
$\mathbf{D}$	diagonal matrix
+IWV, -IWV	periods with increased / decreased integrated water vapor
κ_{abs}	combined liquid and ice phase longwave cloud absorption coefficient
κ_l, κ_i	liquid water / ice absorption coefficients
$|K_w|$	dielectric factor of liquid water
LWF	liquid water fraction
n	size of the state vector
N	number of input parameters used for the neural network training
$N_i(D), N_l(D)$	particle size distribution of ice / liquid water particles
nCRE_{SW}	normalized shortwave cloud radiative effect at the surface
$\mathbf{p}$	Vector of input variables of neural network
$p_{k,nrm}$	k-th input variable of the neural network after the normalization
p_k	k-th input variable of the neural network before the normalization
$p_{k,max}$	maximum value of the k-th input variable of the neural network
$p_{k,min}$	minimum value of the k-th input variable of the neural network
$\mathbf{P}$	rotation operator
$\mathbf{p}$	normalized input variables for neural network training
$\mathbf{P}^T$	transpose of matrix $\mathbf{P}$
P_r	returned power measured by the radars
ρ_i, ρ_l	density of ice / liquid water
ρ_w	water density
Q	surface net radiation budget
Q_{LW}	all-sky surface net longwave radiation budget
Q_{SW}	all-sky surface net shortwave radiation budget
Q_{LWclr}	clear sky surface net longwave radiation budget
Q_{SWclr}	clear sky surface net shortwave radiation budget
Q_i	absorption efficiency of an ice particle
r	range of the radar to the scatters
r_{eff}	effective radius
$r_{\mathrm{eff,ice}}, r_{\mathrm{eff,liq}}$	effective radius of ice / liquid water particles
RHi, RHw	relative humidity with respect to ice / water

S_0	Solar irradiance
σ	Stefan–Boltzmann constant
σ_i	Volume absorption coefficient
σ_m	modeling uncertainty of the surface longwave net flux
σ_{smp}	uncertainty of the surface longwave net flux due to sampling aspect
σ_Σ	resulting uncertainty of the longwave cloud radiative effect retrieved from neural network
σ_x	logarithmic spread of the cloud droplet distribution
T	air temperature
T_a, T_c	effective temperatures of the above cloud atmosphere / the cloud
T_{amb}	ambient air temperature
t_{bs}, t_{cs}	broadband shortwave atmospheric / cloud transmittances
t_{bl}	broadband longwave transmittance of the below cloud atmosphere
t_{cl}	cloud longwave transmittance
+T, -T	periods with increased / decreased temperature at 1450 m
+T +IWV, -T -IWV	periods with both increased / decreased integrated water vapor and temperature
$\mathbf{U}$	identity matrix
V	volume of water in a particle
v_q	q-th element in the error vector
$\mathbf{W}_1, \mathbf{W}_2$	weighting matrices for the hidden and output layers of the neural network
$\mathbf{x}_0$	state vector formed by all elements of the weight matrices and bias vectors of neural network
x_p	p-th element in the state vector
x_1	new state vector
$\mathbf{y}$	vector of output variables of the neural network
Z	radar reflectivity
z	solar zenith angle
α_{ext}	visible extinction coefficient
α_s	broadband surface albedo
α and β	parameters controlling the complexity of the neural network used 5.9 for the Levenberg-Marquardt minimization algorithm
β_{diff}	diffusivity factor
Δz	range resolution
$\Delta CRE_{SW}, \Delta nCRE_{SW}$	relative changes of CRE / normalized CRE in anomalous conditions with respect to normal conditions
$\Delta \alpha_s$	relative changes of surface albedo in anomalous conditions with respect to normal conditions
γ	number of effective parameters
ϵ_{cl} and ϵ_s	broadband emissivities of cloud / surface
μ	coefficient used in Eq.5.11 for the Levenberg-Marquardt minimization algorithm to adjust the number of iterations

Bibliography

Bailey, M. and Hallett, J. (2004). Growth rates and habits of ice crystals between 20° and 70°C. *Journal of the Atmospheric Sciences*, 61(5):514–544.

Bailey, M. and Hallett, J. (2009). A comprehensive habit diagram for atmospheric ice crystals: confirmation from the laboratory, AIRS II, and other field studies. *Journal of the Atmospheric Sciences*, 66(9):2888–2899.

Barker, H. W., Stephens, G. L., Partain, P. T., Bergman, J. W., Bonnel, B., Campana, K., Clothiaux, E. E., Clough, S., Cusack, S., Delamere, J., Edwards, J., Evans, K. F., Fouquart, Y., Freidenreich, S., Galin, V., Hou, Y., Kato, S., Li, J., Mlawer, E., Morcrette, J. J., O'Hirok, W., Räisänen, P., Ramaswamy, V., Ritter, B., Rozanov, E., Schlesinger, M., Shibata, K., Sporyshev, P., Sun, Z., Wendisch, M., Wood, N., and Yang, F. (2003). Assessing 1D atmospheric solar radiative transfer models: Interpretation and handling of unresolved clouds. *Journal of Climate*, 16(16):2676–2699.

Baustian, K. J., Cziczo, D. J., Wise, M. E., Pratt, K. A., Kulkarni, G., Hallar, A. G., and Tolbert, M. A. (2012). Importance of aerosol composition, mixing state, and morphology for heterogeneous ice nucleation: A combined field and laboratory approach. *Journal of Geophysical Research (Atmospheres)*, 117(D6):D06217.

Benestad, R. E., Førland, E. J., and Hanssen-Bauer, I. (2002). Empirically downscaled temperature scenarios for Svalbard. *Atmospheric Science Letters*, 3(2-4):71–93.

Bennartz, R., Shupe, M. D., Turner, D. D., Walden, V. P., Steffen, K., Cox, C. J., Kulie, M. S., Miller, N. B., and Pettersen, C. (2013). July 2012 Greenland melt extent enhanced by low-level liquid clouds. *Nature*, 496:83–86.

Blanchard, Y., Pelon, J., Eloranta, E. W., Moran, K. P., Delanoë, J., and Sèze, G. (2014). A synergistic analysis of cloud cover and vertical distribution from A-Train and ground-based sensors over the high Arctic station Eureka from 2006 to 2010. *Journal of Applied Meteorology and Climatology*, 53:2553–2570.

Block, K., Schneider, F. A., Mülmenstädt, J., Salzmann, M., and Quaas, J. (2019). Climate models disagree on the sign of total radiative feedback in the arctic. *Tellus A: Dynamic Meteorology and Oceanography*, 72(1):1–14.

Boeke, R. C. and Taylor, P. C. (2016). Evaluation of the Arctic surface radiation budget in CMIP5 models. *Journal of Geophysical Research (Atmospheres)*, 121(14):8525–8548.

Boeke, R. C. and Taylor, P. C. (2018). Seasonal energy exchange in sea ice retreat regions contributes to differences in projected Arctic warming. *Nature Communications*, 9:5017.

Boisvert, L. N., Petty, A. A., and Stroeve, J. C. (2016). The impact of the extreme winter 2015/16 Arctic cyclone on the Barents-Kara Seas. *Monthly Weather Review*, 144:4279–4287.

Bringi, V. N. and Chandrasekar, V. (2001). *Polarimetric Doppler Weather Radar*. Cambridge University Press.

Bühl, J., Ansmann, A., Seifert, P., Baars, H., and Engelmann, R. (2013). Toward a quantitative characterization of heterogeneous ice formation with lidar/radar: Comparison of calipso/cloudsat with ground-based observations. *Geophysical Research Letters*, 40(16):4404–4408.

Ceppi, P., Brient, F., Zelinka, M. D., and Hartmann, D. L. (2017). Cloud feedback mechanisms and their representation in global climate models. *WIREs Climate Change*, 8(4):e465.

Cesana, G., Kay, J. E., Chepfer, H., English, J. M., and de Boer, G. (2012). Ubiquitous low-level liquid-containing arctic clouds: New observations and climate model constraints from calipso-goccp. *Geophysical Research Letters*, 39(20).

Cesana, G., Waliser, D. E., Jiang, X., and Li, J.-L. F. (2015). Multimodel evaluation of cloud phase transition using satellite and reanalysis data. *Journal of Geophysical Research: Atmospheres*, 120(15):7871–7892.

Chen, Y., Aires, F., Francis, J. A., and Miller, J. R. (2006). Observed relationships between Arctic longwave cloud forcing and cloud parameters using a neural network. *Journal of Climate*, 19(16):4087.

Clough, S. A., Shephard, M. W., Mlawer, E. J., Delamere, J. S., Iacono, M. J., Cady-Pereira, K., Boukabara, S., and Brown, P. D. (2005). Atmospheric radiative transfer modeling: a summary of the AER codes. *Journal of Quantitative Spectroscopy and Radiative Transfer*, 91(2):233–244.

Cohen, J., Screen, J. A., Furtado, J. C., Barlow, M., Whittleston, D., Coumou, D., Francis, J., Dethloff, K., Entekhabi, D., Overland, J., and Jones, J. (2014). Recent arctic amplification and extreme mid-latitude weather. *Nature Geoscience*, 7(9):627–637. 1752-0908.

Collins, M., Knutti, R., Arblaster, J., Dufresne, J.-L., Fichefet, T., Friedlingstein, P., Gao, X., Gutowski, W. J., Johns, T., Krinner, G., Shongwe, M., Tebaldi, C., Weaver, A. J., and Wehner, M. (2013). *Long-term climate change: Projections, commitments and irreversibility*, chapter 12, page 1029–1136. Cambridge University Press, Cambridge, United Kingdom and New York, NY, USA.

Connolly, P. J., Emersic, C., and Field, P. R. (2012). A laboratory investigation into the aggregation efficiency of small ice crystals. *Atmospheric Chemistry and Physics*, 12(4):2055–2076.

Coumou, D., Di Capua, G., Vavrus, S., Wang, L., and Wang, S. (2018). The influence of Arctic amplification on mid-latitude summer circulation. *Nature Communications*, 9:2959.

Cox, C. J., Uttal, T., Long, C. N., Shupe, M. D., Stone, R. S., and Starkweather, S. (2016). The role of springtime arctic clouds in determining autumn sea ice extent. *Journal of Climate*, 29(18):6581–6596.

Cox, C. J., Walden, V. P., Rowe, P. M., and Shupe, M. D. (2015). Humidity trends imply increased sensitivity to clouds in a warming Arctic. *Nature Communications*, 6:10117.

Curry, J. A., Schramm, J. L., Rossow, W. B., and Randall, D. (1996). Overview of arctic cloud and radiation characteristics. *Journal of Climate*, 9(8):1731–1764.

Dahlke, S. and Maturilli, M. (2017). Contribution of atmospheric advection to the amplified winter warming in the arctic north atlantic region. *Advances in Meteorology*, 2017(Article ID 4928620):8.

DallOsto, M., Geels, C., Beddows, D. C. S., Boertmann, D., Lange, R., Nøjgaard, J. K., Harrison, R. M., Simo, R., Skov, H., and Massling, A. (2018). Regions of open water and melting sea ice drive new particle formation in north east greenland. *Nature*, 6109.

de Boer, G., Collins, W. D., Menon, S., and Long, C. N. (2011). Using surface remote sensors to derive radiative characteristics of mixed-phase clouds: an example from m-pace. *Atmospheric Chemistry and Physics*, 11(23):11937–11949.

de Boer, G., Dexheimer, D., Mei, F., Hubbe, J., Longbottom, C., Carroll, P. J., Apple, M., Goldberger, L., Oaks, D., Lapierre, J., Crume, M., Bernard, N., Shupe, M. D., Solomon, A., Intrieri, J., Lawrence, D., Doddi, A., Holdridge, D. J., Hubbell, M., Ivey, M. D., and Schmid, B. (2019). Atmospheric observations made at Oliktok Point, Alaska, as part of the Profiling at Oliktok Point to Enhance YOPP Experiments (POPEYE) campaign. *Earth System Science Data*, 11(3):1349–1362.

de Boer, G., Eloranta, E. W., and Shupe, M. D. (2009). Arctic mixed-phase stratiform cloud properties from multiple years of surface-based measurements at two high-latitude locations. *Journal of Atmospheric Sciences*, 66:2874.

Delanoe, J. and Hogan, R. (2010). Combined cloudsat-calipso-modis retrievals of the properties of ice clouds. *Journal of Geophysical Research (Atmospheres)*, 115.

Delanoe, J. and Hogan, R. J. (2008). A variational scheme for retrieving ice cloud properties from combined radar, lidar, and infrared radiometer. *Journal of Geophysical Research (Atmospheres)*, 113(D7). D07204.

Delanoë, J., Protat, A., Bouniol, D., Heymsfield, A., Bansemer, A., and Brown, P. (2007). The characterization of ice cloud properties from Doppler radar measurements. *Journal of Applied Meteorology and Climatology*, 46:1682. D00H24.

DeMott, P. J., Prenni, A. J., Liu, X., Kreidenweis, S. M., Petters, M. D., Twohy, C. H., Richardson, M. S., Eidhammer, T., and Rogers, D. C. (2010). Predicting global atmospheric ice nuclei distributions and their impacts on climate. *Proceedings of the National Academy of Sciences*, 107(25):11217–11222.

DeMott, P. J., Prenni, A. J., McMeeking, G. R., Sullivan, R. C., Petters, M. D., Tobo, Y., Niemand , M., Möhler, O., Snider, J. R., and Wang, Z. (2015). Integrating laboratory and field data to quantify the immersion freezing ice nucleation activity of mineral dust particles. *Atmospheric Chemistry and Physics*, 15(1):393–409.

Devasthale, A., Sedlar, J., Kahn, B. H., Tjernström, M., Fetzer, E. J., Tian, B., Teixeira, J., and Pagano, T. S. (2016). A decade of spaceborne observations of the arctic atmosphere: Novel insights from nasa's airs instrument. *Bulletin of the American Meteorological Society*, 97(11):2163–2176.

Dick, G., Gendt, G., and Reigber, C. (2001). First experience with near real-time water vapor estimation in a German GPS network. *Journal of Atmospheric and Solar-Terrestrial Physics*, 63(12):1295 – 1304. Probing the Atmosphere Using the Global Positioning System.

Dirksen, R. J., Sommer, M., Immler, F. J., Hurst, D. F., Kivi, R., and Vömel, H. (2014). Reference quality upper-air measurements: GRUAN data processing for the Vaisala RS92 radiosonde. *Atmospheric Measurement Techniques*, 7(12):4463–4490.

Dong, X., Xi, B., Crosby, K., Long, C. N., Stone, R. S., and Shupe, M. D. (2010). A 10 year climatology of Arctic cloud fraction and radiative forcing at Barrow, Alaska. *Journal of Geophysical Research (Atmospheres)*, 115:D17212.

Donovan, D. P. and van Lammeren, A. C. A. P. (2001). Cloud effective particle size and water content profile retrievals using combined lidar and radar observations, 1, Theory and examples. *Journal of Geophysical Researchn (Atmospheres)*, 106:27425.

Driemel, A., Augustine, J., Behrens, K., Colle, S., Cox, C., Cuevas-Agulló, E., Denn, F. M., Duprat, T., Fukuda, M., Grobe, H., Haeffelin, M., Hodges, G., Hyett, N., Ijima, O., Kallis, A., Knap, W., Kustov, V., Long, C. N., Longenecker, D., Lupi, A., Maturilli, M., Mimouni, M., Ntsangwane, L., Ogihara, H., Olano, X., Olefs, M., Omori, M., Passamani, L., Pereira, E. B., Schmithüsen, H., Schumacher, S., Sieger, R., Tamlyn, J., Vogt, R., Vuilleumier, L., Xia, X., Ohmura, A., and König-Langlo, G. (2018). Baseline surface radiation network (bsrn): structure and data description (1992–2017). *Earth System Science Data*, 10(3):1491–1501.

Ebell, K., Crewell, S., Löhnert, U., Turner, D. D., and O'Connor, E. J. (2011). Cloud statistics and cloud radiative effect for a low-mountain site. *Quarterly Journal of the Royal Meteorological Society*, 137(S1):306–324.

Ebell, K., Nomokonova, T., Maturilli, M., and Ritter, C. (2020). Radiative effect of clouds at ny-alesund, svalbard, as inffered from ground-based remote sensing observations. *Journal of Applied Meteorology and Climatology*, 59(1):3–22.

Ebert, E. E. and Curry, J. A. (1992). A parameterization of ice cloud optical properties for climate models. *Journal of Geophysical Research*, 97(D4):3831–3836.

Engström, A., Karlsson, J., and Svensson, G. (2014). The importance of representing mixed-phase clouds for simulating distinctive atmospheric states in the Arctic*. *Journal of Climate*, 27(1):265–272.

Feofilov, A. G., Stubenrauch, C. J., and Delanoë, J. (2015). Ice water content vertical profiles of high-level clouds: classification and impact on radiative fluxes. *Atmospheric Chemistry and Physics*, 15(21):12327–12344.

Forbes, R. M. and Ahlgrimm, M. (2014). On the representation of high-latitude boundary layer mixed-phase cloud in the ECMWF global model. *Monthly Weather Review*, 142:3425–3445.

Francis, J. A. and Vavrus, S. J. (2015). Evidence for a wavier jet stream in response to rapid Arctic warming. *Environmental Research Letters*, 10(1):014005.

Frey, R. A., Ackerman, S. A., Liu, Y., Strabala, K. I., Zhang, H., Key, J. R., and Wang, X. (2008). Cloud detection with MODIS. Part I: Improvements in the MODIS cloud mask for collection 5. *Journal of Atmospheric and Oceanic Technology*, 25(7):1057.

Frisch, A. S., Feingold, G., Fairall, C. W., Uttal, T., and Snider, J. B. (1998). On cloud radar and microwave radiometer measurements of stratus cloud liquid water profiles. *Journal of Gheophysical Research (Atmospheres)*, 103:23.

Frisch, S., Shupe, M., Djalalova, I., Feingold, G., and Poellot, M. (2002). The retrieval of stratus cloud Droplet effective radius with cloud radars. *Journal of Atmospheric and Oceanic Technology*, 19:835.

Fu, S. and Xue, H. (2017). The effect of ice nuclei efficiency on Arctic mixed-phase clouds from large-eddy simulations. *Journal of Atmospheric Sciences*, 74:3901–3913.

Fukuta, N. and Takahashi, T. (1999). The growth of atmospheric ice crystals: A summary of findings in vertical supercooled cloud tunnel studies. *Journal of Atmospheric Sciences*, 56:1963–1979.

Gallagher, M. R., Shupe, M. D., and Miller, N. B. (2018). Impact of atmospheric circulation on temperature, clouds, and radiation at Summit station, Greenland, with self-organizing maps. *Journal of Climate*, 31(21):8895–8915.

Garrett, T. J., Radke, L. F., and Hobbs, P. V. (2002). Aerosol effects on cloud emissivity and surface longwave heating in the Arctic. *Journal of Atmospheric Sciences*, 59(3):769–778.

Ge, M., Gendt, G., Dick, G., Zhang, F. P., and Rothacher, M. (2006). A new data processing strategy for huge GNSS global networks. *Journal of Geodesy*, 80(4):199–203.

Gendt, G., Dick, G., Reigber, C., Tomassini, M., Liu, Y., and Ramatschi, M. (2004). Near real time GPS water vapor monitoring for numerical weather prediction in Germany. *Journal of the Meteorological Society of Japan. Ser. II*, 82(1B):361–370.

Gjelten, H. M., Øyvind Nordli, Isaksen, K., Førland, E. J., Sviashchennikov, P. N., Wyszynski, P., Prokhorova, U. V., Przybylak, R., Ivanov, B. V., and Urazgildeeva, A. V. (2016). Air temperature variations and gradients along the coast and fjords of western Spitsbergen. *Polar Research*, 35(1):29878.

Graversen, R. G. (2006). Do changes in the midlatitude circulation have any impact on the Arctic surface air temperature trend? *Journal of Climate*, 19:5422.

Graversen, R. G. and Burtu, M. (2016). Arctic amplification enhanced by latent energy transport of atmospheric planetary waves. *Quarterly Journal of the Royal Meteorological Society*, 142:2046–2054.

Graversen, R. G., Langen, P. L., and Mauritsen, T. (2014). Polar Amplification in CCSM4: Contributions from the lapse rate and surface albedo feedbacks. *Journal of Climate*, 27:4433–4450.

Hagan, M., Demuth, H., Hudson Beale, M., and De Jesus, O. (2014). *Neural network design*. ISBN 978-0-9717321-1-7, 2nd edition.

Haynes, J. M., Luo, Z., Stephens, G. L., Marchand, R. T., and Bodas-Salcedo, A. (2007). A multipurpose radar simulation package: QuickBeam. *Bulletin of the American Meteorological Society*, 88:1723–1727.

Hegyi, B. M. and Taylor, P. C. (2018). The unprecedented 2016-2017 Arctic sea ice growth season: The crucial role of atmospheric rivers and longwave fluxes. *Geophysical Reserch Letters*, 45:5204–5212.

Heymsfield, A. J., Protat, A., Bouniol, D., Austin, R. T., Hogan, R. J., Delanoë, J., Okamoto, H., Sato, K., van Zadelhoff, G.-J., Donovan, D. P., and Wang, Z. (2008). Testing IWC retrieval methods using radar and ancillary measurements with in situ data. *Journal of Applied Meteorology and Climatology*, 47(1):135–163.

Hogan, R. J., Brooks, M. E., Illingworth, A. J., Donovan, D. P., Tinel, C., Bouniol, D., and Baptista, J. P. V. P. (2006). Independent evaluation of the ability of spaceborne radar and lidar to retrieve the microphysical and radiative properties of ice clouds. *Journal of Atmospheric and Oceanic Technology*, 23(2):211–227.

Hogan, R. J., Field, P. R., Illingworth, A. J., Cotton, R. J., and Choularton, T. W. (2002). Properties of embedded convection in warm-frontal mixed-phase cloud from aircraft and polarimetric radar. *Quarterly Journal of the Royal Meteorological Society*, 128:451–476.

Hogan, R. J., Francis, P. N., Flentje, H., Illingworth, A. J., Quante, M., and Pelon, J. (2003). Characteristics of mixed-phase clouds. I: Lidar, radar and aircraft observations from CLARE'98. *Quarterly Journal of the Royal Meteorological Society*, 129:2089–2116.

Hogan, R. J., Mittermaier, M. P., and Illingworth, A. J. (2006). The retrieval of ice water content from radar reflectivity factor and temperature and its use in evaluating a mesoscale model. *Journal of Applied Meteorology and Climatology*, 45:301–317.

Hogan, R. J. and O'Connor, E. J. (2004). Facilitating cloud radar and lidar algorithms: the Cloudnet instrument synergy/target categorization product. Cloudnet project documentation - available online: http://www.cloudnet.org/data/products/categorize.html.

Hoose, C. and Möhler, O. (2012). Heterogeneous ice nucleation on atmospheric aerosols: a review of results from laboratory experiments. *Atmospheric Chemistry and Physics*, 12(20):9817–9854.

Hosler, C. L. and Hallgren, R. E. (1960). The aggregation of small ice crystals. *Discuss. Faraday Soc.*, 30:200–207.

Hourdin, F., Grandpeix, J.-Y., Rio, C., Bony, S., Jam, A., Cheruy, F., Rochetin, N., Fairhead, L., Idelkadi, A., Musat, I., Dufresne, J.-L., Lahellec, A., Lefebvre, M.-P., and Roehrig, R. (2013). LMDZ5B: the atmospheric component of the IPSL climate model with revisited parameterizations for clouds and convection. *Climate Dynamics*, 40(9-10):2193–2222.

Houze, Robert A., J. (2012). Orographic effects on precipitating clouds. *Reviews of Geophysics*, 50(1):RG1001.

Huang, J., Zhang, X., Zhang, Q., Lin, Y., Hao, M., Luo, Y., Zhao, Z., Yao, Y., Chen, X., Wang, L., Nie, S., Yin, Y., Xu, Y., and Zhang, J. (2017). Recently amplified arctic warming has contributed to a continual global warming trend. *Nature Climate Change*, 7:875–879.

Hwang, Y.-T., Frierson, D. M. W., and Kay, J. E. (2011). Coupling between Arctic feedbacks and changes in poleward energy transport. *Geophysical Reserch Letters*, 38:L17704.

Iacono, M. J., Mlawer, E. J., Clough, S. A., and Morcrette, J.-J. (2000). Impact of an improved longwave radiation model, RRTM, on the energy budget and thermodynamic properties of the NCAR community climate model, CCM3. *Journal of Geophysical Research: Atmospheres*, 105(D11):14873–14890.

Illingworth, A. J., Hogan, R. J., O'Connor, E., Bouniol, D., Brooks, M. E., Delanoé, J., Donovan, D. P., Eastment, J. D., Gaussiat, N., Goddard, J. W. F., Haeffelin, M., Baltink, H. K., Krasnov, O. A., Pelon, J., Piriou, J.-M., Protat, A., Russchenberg, H. W. J., Seifert, A., Tompkins, A. M., van Zadelhoff, G.-J., Vinit, F., Willén, U., Wilson, D. R., and Wrench, C. L. (2007). Cloudnet. *Bulletin of the American Meteorological Society*, 88(6):883–898.

Intrieri, J. M., Shupe, M. D., Uttal, T., and McCarty, B. J. (2002). An annual cycle of Arctic cloud characteristics observed by radar and lidar at SHEBA. *Journal of Geophysical Research (Oceans)*, 107:8030.

Isaksen, K., Nordli, Å., Førland, E. J., Łupikasza, E., Eastwood, S., and Niedźwiedź, T. (2016). Recent warming on Spitsbergen—Influence of atmospheric circulation and sea ice cover. *Journal of Geophysical Research (Atmospheres)*, 121(20):11,913–11,931.

Johansson, E., Devasthale, A., Tjernström, M., Ekman, A. M. L., and L'Ecuyer, T. (2017). Response of the lower troposphere to moisture intrusions into the arctic. *Geophysical Research Letters*, 44(5):2527–2536. 2017GL072687.

Jung, C. H., Yoon, Y. J., Kang, H. J., Gim, Y., Lee, B. Y., Ström, J., Krejci, R., and Tunved, P. (2018). The seasonal characteristics of cloud condensation nuclei (CCN) in the arctic lower troposphere. *Tellus Series B Chemical and Physical Meteorology B*, 70(1):1–13.

Kanamitsu, M. (1989). Description of the NMC global data assimilation and forecast system. *Weather and Forecasting*, 4:335–342.

Kanji, Z. A., Ladino, L. A., Wex, H., Boose, Y., Burkert-Kohn, M., Cziczo, D. J., and Krämer, M. (2017). Overview of ice nucleating particles. *Meteorological Monographs*, 58:1.1–1.33.

Kanno, Y., Walsh, J. E., Abdillah, M. R., Yamaguchi, J., and Iwasaki, T. (2019). Indicators and trends of polar cold airmass. *Environmental Research Letters*, 14(2):025006.

Kapsch, M.-L., Graversen, R. G., and Tjernström, M. (2013). Springtime atmospheric energy transport and the control of Arctic summer sea-ice extent. *Nature Clim. Change*, 3:744–748.

Karlsson, J. and Svensson, G. (2011). The simulation of Arctic clouds and their influence on the winter surface temperature in present-day climate in the CMIP3 multi-model dataset. *Climate Dynamics*, 36:623–635.

Kay, J. E., Bourdages, L., Miller, N. B., Morrison, A., Yettella, V., Chepfer, H., and Eaton, B. (2016). Evaluating and improving cloud phase in the Community Atmosphere Model version 5 using spaceborne lidar observations. *Journal of Geophysical Research (Atmospheres)*, 121:4162–4176.

Kay, J. E. and Gettelman, A. (2009). Cloud influence on and response to seasonal Arctic sea ice loss. *Journal of Geophysical Research (Atmospheres)*, 114:D18204.

Kay, J. E., L'Ecuyer, T., Gettelman, A., Stephens, G., and O'Dell, C. (2008). The contribution of cloud and radiation anomalies to the 2007 Arctic sea ice extent minimum. *Geophysical Research Letters*, 35:L08503.

King, M. D., Platnick, S., Menzel, W. P., Ackerman, S. A., and Hubanks, P. A. (2013). Spatial and temporal distribution of clouds observed by MODIS onboard the Terra and Aqua satellites. *IEEE Transactions on Geoscience and Remote Sensing*, 51(7):3826–3852.

King, M. D., Platnick, S., Wind, G., Arnold, G. T., and Dominguez, R. T. (2010). Remote sensing of radiative and microphysical properties of clouds during TC4:

Results from MAS, MASTER, MODIS, and MISR. *Journal of Geophysical Research: Atmospheres (1984–2012)*, 115(D10).

Klein, S. A., McCoy, R. B., Morrison, H., Ackerman, A. S., Avramov, A., Boer, G. D., Chen, M., Cole, J. N. S., Del Genio, A. D., Falk, M., Foster, M. J., Fridlind, A., Golaz, J.-C., Hashino, T., Harrington, J. Y., Hoose, C., Khairoutdinov, M. F., Larson, V. E., Liu, X., Luo, Y., McFarquhar, G. M., Menon, S., Neggers, R. A. J., Park, S., Poellot, M. R., Schmidt, J. M., Sednev, I., Shipway, B. J., Shupe, M. D., Spangenberg, D. A., Sud, Y. C., Turner, D. D., Veron, D. E., Salzen, K. V., Walker, G. K., Wang, Z., Wolf, A. B., Xie, S., Xu, K.-M., Yang, F., and Zhang, G. (2009). Intercomparison of model simulations of mixed-phase clouds observed during the ARM mixed-phase Arctic cloud experiment. I: single-layer cloud. *Quarterly Journal of the Royal Meteorological Society*, 135:979–1002.

Kneifel, S., von Lerber, A., Tiira, J., Moisseev, D., Kollias, P., and Leinonen, J. (2015). Observed relations between snowfall microphysics and triple-frequency radar measurements. *Journal of Geophysical Research (Atmospheres)*, pages 6034–6055. 2015JD023156.

Komurcu, M., Storelvmo, T., Tan, I., Lohmann, U., Yun, Y., Penner, J. E., Wang, Y., Liu, X., and Takemura, T. (2014). Intercomparison of the cloud water phase among global climate models. *Journal of Geophysical Research: Atmospheres*, 119(6):3372–3400.

Korolev, A. and Field, P. R. (2008). The effect of dynamics on mixed-phase clouds: Theoretical considerations. *Journal of Atmospheric Sciences*, 65:66.

Korolev, A. V., Isaac, G. A., Cober, S. G., Strapp, J. W., and Hallett, J. (2003). Microphysical characterization of mixed-phase clouds. *Quarterly Journal of the Royal Meteorological Society*, 129:39–65.

Korolev, A. V. and Mazin, I. P. (2003). Supersaturation of water vapor in clouds. *Journal of Atmospheric Sciences*, 60:2957–2974.

Küchler, N., Kneifel, S., Löhnert, U., Kollias, P., Czekala, H., and Rose, T. (2017). A W-Band radar-radiometer system for accurate and continuous monitoring of clouds and precipitation. *Journal of Atmospheric and Oceanic Technology*, 34:2375–2392.

Ladino Moreno, L. A., Stetzer, O., and Lohmann, U. (2013). Contact freezing: a review of experimental studies. *Atmospheric Chemistry and Physics*, 13(19):9745–9769.

Lanconelli, C., Busetto, M., Dutton, E. G., König-Langlo, G., Maturilli, M., Sieger, R., Vitale, V., and Yamanouchi, T. (2011). Polar baseline surface radiation measurements during the International Polar Year 2007–2009. *Earth System Science Data*, 3(1):1–8.

Lange, R., Dall'Osto, M., Skov, H., Nøjgaard, J., Nielsen, I., Beddows, D., Simo, R., Harrison, R., and Massling, A. (2018). Characterization of distinct Arctic aerosol accumulation modes and their sources. *Atmospheric Environment*, 183:1 – 10.

Liu, Y., Ackerman, S. A., Maddux, B. C., Key, J. R., and Frey, R. A. (2010). Errors in cloud detection over the Arctic using a satellite imager and implications for observing feedback mechanisms. *Journal of Climate*, 23(7):1894–1907.

Liu, Y., Key, J. R., Ackerman, S. A., Mace, G. G., and Zhang, Q. (2012). Arctic cloud macrophysical characteristics from CloudSat and CALIPSO. *Remote Sensing of Environment*, 124:159–173.

Liu, Y., Shupe, M. D., Wang, Z., and Mace, G. (2017). Cloud vertical distribution from combined surface and space radar–lidar observations at two Arctic atmospheric observatories. *Atmospheric Chemistry and Physics*, 17(9):5973–5989.

Loehnert, U. (2002). *Derivation of cloud liquid water from ground-based active and passive microwave remote sensors.* PhD thesis, Meteorological Institute, Rheinische Friedrich-Wilhems-Universitat Bonn.

Löhnert, U. and Crewell, S. (2003). Accuracy of cloud liquid water path from ground-based microwave radiometry 1. Dependency on cloud model statistics. *Radio Science.*

Löhnert, U. and Maier, O. (2012). Operational profiling of temperature using ground-based microwave radiometry at Payerne: prospects and challenges. *Atmospheric Measurement Techniques*, 5(5):1121–1134.

Long, C. N. and Ackerman, T. P. (2000). Identification of clear skies from broadband pyranometer measurements and calculation of downwelling shortwave cloud effects. , 105(D12):15,609–15,626.

Long, C. N. and Turner, D. D. (2008). A method for continuous estimation of clear-sky downwelling longwave radiative flux developed using ARM surface measurements. *Journal of Geophysical Research: Atmospheres*, 113(D18).

Luke, E. P., Kollias, P., and Shupe, M. D. (2010). Detection of supercooled liquid in mixed-phase clouds using radar Doppler spectra. *Journal of Geophysical Research (Atmospheres)*, 115:19201.

Maahn, M., Burgard, C., Crewell, S., Gorodetskaya, I. V., Kneifel, S., Lhermitte, S., Van Tricht, K., and van Lipzig, N. P. M. (2014). How does the spaceborne radar blind zone affect derived surface snowfall statistics in polar regions? *Journal of Geophysical Research (Atmospheres)*, 119:13.

Marchand, R., Mace, G. G., Ackerman, T., and Stephens, G. (2008). Hydrometeor detection using Cloudsat – An Earth-orbiting 94-GHz cloud radar. *Journal of Atmospheric and Oceanic Technology*, 25:519.

Marke, T., Ebell, K., Löhnert, U., and Turner, D. D. (2016). Statistical retrieval of thin liquid cloud microphysical properties using ground-based infrared and microwave observations. *Journal of Geophysical Research (Atmospheres)*, 121:14.

Matrosov, S. Y. (2009). A method to estimate vertically integrated amounts of cloud ice and liquid and mean rain rate in stratiform precipitation from radar and auxiliary data. *Journal of Applied Meteorology and Climatology*, 48:1398.

Matrosov, S. Y. (2011). Feasibility of using radar differential Doppler velocity and dual-frequency ratio for sizing particles in thick ice clouds. *Journal of Geophysical Research (Atmospheres)*, 116(D15):17202.

Matthes, H., Rinke, A., and Dethloff, K. (2015). Recent changes in Arctic temperature extremes: warm and cold spells during winter and summer. *Environmental Research Letters*, 10(11):114020.

Mattingly, K. S., Ramseyer, C. A., Rosen, J. J., Mote, T. L., and Muthyala, R. (2016). Increasing water vapor transport to the Greenland ice sheet revealed using self-organizing maps. *Geophysical Research Letters*, 43(17):9250–9258.

Maturilli, M. and Ebell, K. (2018). 25 years of cloud base height measurements by ceilometer in Ny-Ålesund, Svalbard. *Earth System Science Data*, 10:1451–1456.

Maturilli, M., Herber, A., and König-Langlo, G. (2013). Climatology and time series of surface meteorology in Ny-Ålesund, Svalbard. *Earth System Science Data*, 5:155–163.

Maturilli, M., Herber, A., and König-Langlo, G. (2015). Surface radiation climatology for Ny-Ålesund, Svalbard (78.9° N), basic observations for trend detection. *Theoretical and Applied Climatology*, 120(1):331–339.

Maturilli, M. and Kayser, M. (2016). Arctic warming, moisture increase and circulation changes observed in the Ny-Ålesund homogenized radiosonde record. *Theoretical and Applied Climatology*.

Matus, A. V. and L'Ecuyer, T. S. (2017). The role of cloud phase in Earth's radiation budget. *Journal of Geophysical Research: Atmospheres*, 122(5):2559–2578.

McGrath, R., Semmler, T., Sweeney, C., and Wang, S. (2006). Impact of balloon drift errors in radiosonde data on climate statistics. *Journal of Climate*, 19(14):3430–3442.

Mewes, D. and Jacobi, C. (2019). Heat transport pathways into the Arctic and their connections to surface air temperatures. *Atmospheric Chemistry and Physics*, 19:3927–3937.

Meyer, A., Fer, I., Sundfjord, A., and Peterson, A. K. (2017). Mixing rates and vertical heat fluxes north of Svalbard from Arctic winter to spring. *Journal of Geophysical Research (Oceans)*, 122(6):4569–4586.

Miles, N. L., Verlinde, J., and Clothiaux, E. E. (2000). Cloud droplet size distributions in low-level stratiform clouds. *Journal of Atmospheric Sciences*, 57:295–311.

Miller, N. B., Shupe, M. D., Cox, C. J., Noone, D., Persson, P. O. G., and Steffen, K. (2017). Surface energy budget responses to radiative forcing at Summit, Greenland. *The Cryosphere*, 11(1):497–516.

Miller, N. B., Shupe, M. D., Cox, C. J., Walden, V. P., Turner, D. D., and Steffen, K. (2015). Cloud radiative forcing at Summit, Greenland. *Journal of Climate*, 28:6267–6280.

Miller, N. B., Shupe, M. D., Lenaerts, J. T. M., Kay, J. E., de Boer, G., and Bennartz, R. (2018). Process-based model evaluation using surface energy budget observations in Central Greenland. *Journal of Geophysical Research (Atmospheres)*, 123:4777–4796.

Minnett, P. J. (1999). The influence of solar zenith angle and cloud type on cloud radiative forcing at the surface in the Arctic. *Journal of Climate*, 12(1):147–158.

Mioche, G., Jourdan, O., Ceccaldi, M., and Delanoë, J. (2015). Variability of mixed-phase clouds in the Arctic with a focus on the Svalbard region: a study based on spaceborne active remote sensing. *Atmospheric Chemistry and Physics*, 15:2445–2461.

Mlawer, E. J., Taubman, S. J., Brown, P. D., Iacono, M. J., and Clough, S. A. (1997). Radiative transfer for inhomogeneous atmospheres: RRTM, a validated correlated-k model for the longwave. *Journal of Geophysical Research (Atmospheres)*, 102(D14):16663–16682.

Morrison, H., de Boer, G., Feingold, G., Harrington, J., Shupe, M. D., and Sulia, K. (2012). Resilience of persistent Arctic mixed-phase clouds. *Nature Geoscience*, 5:11–17.

Morrison, H., Pinto, J. O., Curry, J. A., and McFarquhar, G. M. (2008). Sensitivity of modeled arctic mixed-phase stratocumulus to cloud condensation and ice nuclei over regionally varying surface conditions. *Journal of Geophysical Research (Atmospheres)*, 113:D05203.

Mortin, J., Svensson, G., Graversen, R. G., Kapsch, M.-L., Stroeve, J. C., and Boisvert, L. N. (2016). Melt onset over Arctic sea ice controlled by atmospheric moisture transport. *Geophysical Research Letters*, 43:6636–6642.

Mülmenstädt, J., Sourdeval, O., Delanoë, J., and Quaas, J. (2015). Frequency of occurrence of rain from liquid-, mixed-, and ice-phase clouds derived from A-Train satellite retrievals. *Geophysical Research Letters*, 42:6502–6509.

Murray, B. J., O'Sullivan, D., Atkinson, J. D., and Webb, M. E. (2012). Ice nucleation by particles immersed in supercooled cloud droplets. *Chem. Soc. Rev.*, 41:6519–6554.

Myagkov, A., Seifert, P., Bauer-Pfundstein, M., and Wandinger, U. (2016). Cloud radar with hybrid mode towards estimation of shape and orientation of ice crystals. *Atmospheric Measurement Techniques*, 9:469–489.

Myagkov, A., Seifert, P., Wandinger, U., Bühl, J., and Engelmann, R. (2016). Relationship between temperature and apparent shape of pristine ice crystals derived from polarimetric cloud radar observations during the ACCEPT campaign. *Atmospheric Measurement Techniques*, 9(8):3739–3754.

Myhre, G., Shindell, D., Bréon, F.-M., Collins, W., Fuglestvedt, J., Huang, J., Koch, D., Lamarque, J.-F., Lee, D., Mendoza, B., Nakajima, T., Robock, A., Stephens, G., Takemura, T., and Zhang, H. (2013). *Anthropogenic and natural radiative forcing*, pages 659–740. Cambridge University Press, Cambridge, UK.

Nguyen, D. and Widrow, B. (1990). Improving the learning speed of 2-layer neural networks by choosing initial values of the adaptive weights. In *1990 IJCNN International Joint Conference on Neural Networks*, pages 21–26 vol.3.

Nomokonova, T. and Ebell, K. (2019). Cloud microphysical properties retrieved from ground-based remote sensing at Ny-Ålesund (10 June 2016 - 8 October 2018). University of Cologne, PANGAEA, https://doi.pangaea.de/10.1594/PANGAEA.898556.

Nomokonova, T., Ebell, K., Löhnert, U., Maturilli, M., and Ritter, C. (2019a). The influence of anomalous atmospheric conditions at Ny-Ålesund on clouds and their radiative effect. *Atmospheric Chemistry and Physics Discussions*, 2019:1–34.

Nomokonova, T., Ebell, K., Löhnert, U., Maturilli, M., Ritter, C., and O'Connor, E. (2019b). Statistics on clouds and their relation to thermodynamic conditions at Ny-Ålesund using ground-based sensor synergy. *Atmospheric Chemistry and Physics*, 19(6):4105–4126.

Nörenberg, D. (2008). Development of ground equipment for atmospheric propagation conditions assessment from 10 up to 90 GHz frequency bands (ATPROP). Software documentation, Institute for Geophysics and Meteorolgy, University of Cologne, and Radiometer Physics GmbH, Meckenheim. ESA CONTRACT 19839/06/NL/GLC.

Nyeki, S., Wacker, S., Aebi, C., Gröbner, J., Martucci, G., and Vuilleumier, L. (2019). Trends in surface radiation and cloud radiative effect at four Swiss sites for the 1996–2015 period. *Atmospheric Chemistry and Physics*, 19(20):13227–13241.

O'Connor, E. J., Illingworth, A. J., and Hogan, R. J. (2004). A technique for autocalibration of cloud lidar. *Journal of Atmospheric and Oceanic Technology*, 21(5):777–786.

Ohmura, A. (2012). Present status and variations in the Arctic energy balance. *Polar Science*, 6(1):5–13.

Ørbæk, J. B., Hisdal, V., and Svaasand , L. E. (1999). Radiation climate variability in Svalbard: surface and satellite observations. *National Institute Polar Research Memoirs*, 18(2):127–134.

Overland, J. E., D. K., Francis, J. A., Hall, R. J., Hanna, E., Kim, S.-J., Screen, J. A., Shepherd, T. G., and Vihma, T. (2016). Nonlinear response of mid-latitude weather to the changing Arctic. *Nature Climate Change*. 2016/10/26/online.

Overland, J. E., Hanna, E., Hanssen-Bauer, I., Kim, S. J., Walsh, J. E., Wang, M., Bhatt, U., and Thoman, R. (2017). Surface air temperature. In *Arctic Report Card: Update for 2017*.

Overland, J. E. and Wang, M. (2016). Recent extreme Arctic temperatures are due to a split Polar vortex. *Journal of Climate*, 29:5609–5616.

Palm, S. P., Strey, S. T., Spinhirne, J., and Markus, T. (2010). Influence of Arctic sea ice extent on polar cloud fraction and vertical structure and implications for regional climate. *Journal of Geophysical Research (Atmospheres)*, 115:D21209.

Persson, P. O. G., Shupe, M. D., Perovich, D., and Solomon, A. (2017). Linking atmospheric synoptic transport, cloud phase, surface energy fluxes, and sea-ice growth: observations of midwinter SHEBA conditions. *Climate Dynamics*, 49(4):1341–1364.

Peterson, A. K., Fer, I., McPhee, M. G., and Rand elhoff, A. (2017). Turbulent heat and momentum fluxes in the upper ocean under Arctic sea ice. *Journal of Geophysical Research (Oceans)*, 122(2):1439–1456.

Pettersen, C., Bennartz, R., Merrelli, A. J., Shupe, M. D., Turner, D. D., and Walden, V. P. (2018). Precipitation regimes over central Greenland inferred from 5 years of ICECAPS observations. *Atmospheric Chemistry and Physics*, 18(7):4715–4735.

Pithan, F. and Mauritsen, T. (2014). Arctic amplification dominated by temperature feedbacks in contemporary climate models. *Nature Geoscience*, 7:181–184.

Protat, A., Armstrong, A., Haeffelin, M., Morille, Y., Pelon, J., Delanoë, J., and Bouniol, D. (2006). Impact of conditional sampling and instrumental limitations on the statistics of cloud properties derived from cloud radar and lidar at SIRTA. *Geophysical Research Letters*, 33:L11805.

Qiu, S., Xi, B., and Dong, X. (2018). Influence of wind direction on thermodynamic properties and Arctic mixed-phase clouds in autumn at Utqiaġvik, Alaska. *Journal of Geophysical Research (Atmospheres)*, 123(17):9589–9603.

Raddatz, R. L., Asplin, M. G., Papakyriakou, T., Candlish, L. M., Galley, R. J., Else, B., and Barber, D. G. (2013). All-sky downwelling longwave radiation and atmospheric-column water vapour and temperature over the Western maritime Arctic. *Atmosphere-Ocean*, 51(2):145–152.

Ramanathan, V., Cess, R. D., Harrison, E. F., Minnis, P., Barkstrom, B. R., Ahmad, E., and Hartmann, D. (1989). Cloud-radiative forcing and climate: results from the Earth radiation budget experiment. *Science*, 243(4887):57–63.

Ray, P. S. (1972). Broadband complex refractive indices of ice and water. *Applied Optics*, 11:1836–1844.

Ricchiazzi, P., Yang, S., Gautier, C., and Sowle, D. (1998). SBDART: A research and teaching software tool for plane-parallel radiative transfer in the Earth's atmosphere. *Bulletin of the American Meteorological Society*, 79(10):2101–2114.

Rinke, A., Dethloff, K., Dorn, W., Handorf, D., and Moore, J. C. (2013). Simulated Arctic atmospheric feedbacks associated with late summer sea ice anomalies. *Journal of Geophysical Research (Atmospheres)*, 118:7698–7714.

Rose, T., Crewell, S., Löhnert, U., and Simmer, C. (2005). A network suitable microwave radiometer for operational monitoring of the cloudy atmosphere. *Atmospheric Research*, 75(3):183 – 200. CLIWA-NET: Observation and Modelling of Liquid Water Clouds.

Sandvik, A., Biryulina, M., Kvamstø, N. G., Stamnes, J. J., and Stamnes, K. (2007). Observed and simulated microphysical composition of arctic clouds: Data properties and model validation. *Journal of Geophysical Research (Atmospheres)*, 112:D05205.

Schmidt, J., Ansmann, A., Bühl, J., Baars, H., Wandinger, U., Müller, D., and Malinka, A. V. (2014). Dual-FOV Raman and Doppler lidar studies of aerosol-cloud interactions: Simultaneous profiling of aerosols, warm-cloud properties, and vertical wind. *Journal of Geophysical Research (Atmospheres)*, 119(9):5512–5527.

Sedlar, J. and Tjernström, M. (2017). Clouds, warm air, and a climate cooling signal over the summer Arctic. *Geophysical Research Letters*, 44:1095–1103.

Sedlar, J., Tjernström, M., Mauritsen, T., Shupe, M. D., Brooks, I. M., Persson, P. O. G., Birch, C. E., Leck, C., Sirevaag, A., and Nicolaus, M. (2011). A transitioning Arctic surface energy budget: the impacts of solar zenith angle, surface albedo and cloud radiative forcing. *Climate Dynamics*, 37(7):1643–1660.

Sengupta, M., Clothiaux, E. E., Ackerman, T. P., Kato, S., and Min, Q. (2003). Importance of accurate liquid water path for estimation of solar radiation in warm boundary layer clouds: An observational study. *Journal of Climate*, 16(18):2997–3009.

Serreze, M. C., Barrett, A. P., and Cassano, J. J. (2011). Circulation and surface controls on the lower tropospheric air temperature field of the Arctic. *Journal of Geophysical Research (Atmospheres)*, 116:D07104.

Serreze, M. C., Barrett, A. P., Stroeve, J. C., Kindig, D. N., and Holland, M. M. (2009). The emergence of surface-based Arctic amplification. *The Cryosphere*, 3(1):11–19.

Shupe, M. D. (2007). A ground-based multisensor cloud phase classifier. *Geophysical Research Letters*, 34:L22809.

Shupe, M. D. (2011). Clouds at Arctic atmospheric observatories. Part II: Thermodynamic phase characteristics. *Journal of Applied Meteorology and Climatology*, 50:645–661.

Shupe, M. D. and Intrieri, J. M. (2004). Cloud radiative forcing of the Arctic surface: The influence of cloud properties, surface albedo, and solar zenith angle. *Journal of Climate*, 17:616–628.

Shupe, M. D., Matrosov, S. Y., and Uttal, T. (2006). Arctic mixed-phase cloud properties derived from surface-based sensors at SHEBA. *Journal of Atmospheric Sciences*, 63:697–711.

Shupe, M. D., Turner, D. D., Walden, V. P., Bennartz, R., Cadeddu, M. P., Castellani, B. B., Cox, C. J., Hudak, D. R., Kulie, M. S., Miller, N. B., Neely, III, R. R., Neff, W. D., and Rowe, P. M. (2013). High and dry: New observations of tropospheric and cloud properties above the Greenland ice sheet. *Bulletin of the American Meteorological Society*, 94:169–186.

Shupe, M. D., Turner, D. D., Zwink, A., Thieman, M. M., Mlawer, E. J., and Shippert, T. (2015). Deriving Arctic cloud microphysics at Barrow, Alaska: Algorithms, results, and radiative closure. *Journal of Applied Meteorology and Climatology*, 54:1675–1689.

Shupe, M. D., Walden, V. P., Eloranta, E., Uttal, T., Campbell, J. R., Starkweather, S. M., and Shiobara, M. (2011). Clouds at Arctic atmospheric observatories. Part I: Occurrence and macrophysical properties. *Journal of Applied Meteorology and Climatology*, 50:626–644.

Sillmann, J., Kharin, V. V., Zhang, X., Zwiers, F. W., and Bronaugh, D. (2013). Climate extremes indices in the CMIP5 multimodel ensemble: Part 1. Model evaluation in the present climate. *Journal of Geophysical Research (Atmospheres)*, 118:1716–1733.

Smith, W. L., Ma, X. L., Ackerman, S. A., Revercomb, H. E., and Knuteson, R. O. (1993). Remote sensing cloud properties from high spectral resolution infrared observations. *Journal of Atmospheric Sciences*, 50(12):1708–1720.

Solomon, S., Qin, D., Manning, M., Chen, Z., Marquis, M., Averyt, K. B., Tignor, M., and Miller, H. L. (2007). Intergovernmental panel on climate change. In Solomon, S., Qin, D., Manning, M., Chen, Z., Marquis, M., Averyt, K. B., Tignor, M., and Miller, H. L., editors, *Climate Change 2007: The Physical Science Basis. Contribution of Working Group I to the Fourth Assessment Report of the Intergovernmental Panel on Climate Change*. Cambridge University Press.

Sommer, M., Dirksen, R., and Immler, F. (2012). RS92 GRUAN data product version 2 (RS92-GDP.2). *GRUAN Lead Centre*. DOI:10.5676/GRUAN/RS92-GDP.2.

Steinke, S., Eikenberg, S., Löhnert, U., Dick, G., Klocke, D., Di Girolamo, P., and Crewell, S. (2015). Assessment of small-scale integrated water vapour variability during HOPE. *Atmospheric Chemistry and Physics*, 15:2675–2692.

Stephens, G. L. (1978). Radiation profiles in extended water clouds. II: Parameterization schemes. *Journal of Atmospheric Sciences*, 35(11):2123–2132.

Stohl, A. (1998). Computation, accuracy and applications of trajectories—A review and bibliography. *Atmospheric Environment*, 32(6):947–966.

Stohl, A. and Seibert, P. (1998). Accuracy of trajectories as determined from the conservation of meteorological tracers. *Quarterly Journal of the Royal Meteorological Society*, 124(549):1465–1484.

Stohl, A., Wotawa, G., Seibert, P., and Kromp-Kolb, H. (1995). Interpolation errors in wind fields as a function of spatial and temporal resolution and their impact on different types of kinematic trajectories. *Journal of Applied Meteorology*, 34(10):2149–2165.

Sun, Z. and Shine, K. P. (1994). Studies of the radiative properties of ice and mixed-phase clouds. *Quarterly Journal of the Royal Meteorological Society*, 120:111–137.

Susskind, J., Schmidt, G. A., Lee, J. N., and Iredell, L. (2019). Recent global warming as confirmed by AIRS. *Environmental Research Letters*, 14(4):044030.

Tan, H., Mao, J., Chen, H., Chan, P. W., Wu, D., Li, F., and Deng, T. (2011). A study of a retrieval method for temperature and humidity profiles from microwave radiometer observations based on principal component analysis and stepwise regression. *Journal of Atmospheric and Oceanic Technology*, 28(3):378–389.

Taylor, P. C., Cai, M., Hu, A., Meehl, J., Washington, W., and Zhang, G. J. (2013). A decomposition of feedback contributions to Polar warming amplification. *Journal of Climate*, 26:7023–7043.

Tetzlaff, A., Lüpkes, C., Birnbaum, G., Hartmann, J., Nygård, T., and Vihma, T. (2014). Brief Communication: Trends in sea ice extent north of Svalbard and its impact on cold air outbreaks as observed in spring 2013. *The Cryosphere*, 8(5):1757–1762.

Tjernström, M., Leck, C., Birch, C. E., Bottenheim, J. W., Brooks, B. J., Brooks, I. M., Bäcklin, L., Chang, R. Y.-W., de Leeuw, G., Di Liberto, L., de la Rosa, S., Granath, E., Graus, M., Hansel, A., Heintzenberg, J., Held, A., Hind, A., Johnston, P., Knulst, J., Martin, M., Matrai, P. A., Mauritsen, T., Müller, M., Norris, S. J., Orellana, M. V., Orsini, D. A., Paatero, J., Persson, P. O. G., Gao, Q., Rauschenberg, C., Ristovski, Z., Sedlar, J., Shupe, M. D., Sierau, B., Sirevaag, A., Sjogren, S., Stetzer, O., Swietlicki, E., Szczodrak, M., Vaattovaara, P., Wahlberg, N., Westberg, M., and Wheeler, C. R. (2014). The Arctic summer cloud ocean study (ASCOS): overview and experimental design. *Atmospheric Chemistry and Physics*, 14:2823–2869.

Tjernström, M., Sedlar, J., and Shupe, M. D. (2008). How well do regional climate models reproduce radiation and clouds in the Arctic? An evaluation of ARCMIP simulations. *Journal of Applied Meteorology and Climatology*, 47:2405.

Tjernström, M., Shupe, M. D., Brooks, I. M., Achtert, P., Prytherch, J., and Sedlar, J. (2019). Arctic summer airmass transformation, surface inversions, and the surface energy budget. *Journal of Climate*, 32:769–789.

Trenberth, K. E. and Stepaniak, D. P. (2004). The flow of energy through the earth's climate system. *Quarterly Journal of the Royal Meteorological Society*, 130(603):2677–2701.

Trepte, Q. Z., Bedka, K. M., Chee, T. L., Minnis, P., Sun-Mack, S., Yost, C. R., Chen, Y., Jin, Z., Hong, G., Chang, F.-L., and Smith, W. L. (2019). Global cloud detection for CERES edition 4 using Terra and Aqua MODIS data. *IEEE Transactions on Geoscience and Remote Sensing*, 57(11):9410–9449.

Turner, D. D., Shupe, M. D., and Zwink, A. B. (2018). Characteristic atmospheric radiative heating rate profiles in Arctic clouds as observed at Barrow, Alaska. *Journal of Applied Meteorology and Climatology*, 57:953–968.

Turner, D. D., Vogelmann, A. M., Austin, R. T., Barnard, J. C., Cady-Pereira, K., Chiu, J. C., Clough, S. A., Flynn, C., Khaiyer, M. M., Liljegren, J., Johnson, K., Lin, B., Long, C., Marshak, A., Matrosov, S. Y., McFarlane, S. A., Miller, M., Min, Q., Minnis, P., O'Hirok, W., Wang, Z., and Wiscombe, W. (2007). Thin liquid water clouds: Their importance and our challenge. *Bulletin of the American Meteorological Society*, 88:177.

Uttal, T., Curry, J. A., McPhee, M. G., Perovich, D. K., Moritz, R. E., Maslanik, J. A., Guest, P. S., Stern, H. L., Moore, J. A., Turenne, R., Heiberg, A., Serreze, M. C., Wylie, D. P., Persson, O. G., Paulson, C. A., Halle, C., Morison, J. H., Wheeler, P. A., Makshtas, A., Welch, H., Shupe, M. D., Intrieri, J. M., Stamnes, K., Lindsey, R. W., Pinkel, R., Pegau, W. S., Stanton, T. P., and Grenfeld, T. C. (2002). Surface heat budget of the Arctic ocean. *Bulletin of the American Meteorological Society*, 83:255–276.

van den Broeke, M., Bamber, J., Ettema, J., Rignot, E., Schrama, E., van de Berg, W. J., van Meijgaard, E., Velicogna, I., and Wouters, B. (2009). Partitioning recent Greenland mass loss. *Science*, 326(5955):984.

Vavrus, S. (2004). The impact of cloud feedbacks on Arctic climate under Greenhouse forcing. *Journal of Climate*, 17(3):603–615.

Verlinde, J., Harrington, J. Y., McFarquhar, G. M., Yannuzzi, V. T., Avramov, A., Greenberg, S., Johnson, N., Zhang, G., Poellot, M. R., Mather, J. H., Turner, D. D., Eloranta, E. W., Zak, B. D., Prenni, A. J., Daniel, J. S., Kok, G. L., Tobin, D. C., Holz, R., Sassen, K., Spangenberg, D., Minnis, P., Tooman, T. P., Ivey, M. D., Richardson, S. J., Bahrmann, C. P., Shupe, M., Demott, P. J., Heymsfield, A. J., and Schofield, R. (2007). The mixed-phase Arctic cloud experiment. *Bulletin of the American Meteorological Society*, 88:205.

Verlinde, J., Zak, B. D., Shupe, M. D., Ivey, M. D., and Stamnes, K. (2016). The ARM North slope of Alaska (NSA) sites. *Meteorological Monographs*, 57:8.1–8.13.

Vihma, T., Pirazzini, R., Fer, I., Renfrew, I. A., Sedlar, J., Tjernström, M., Lüpkes, C., Nygård, T., Notz, D., Weiss, J., Marsan, D., Cheng, B., Birnbaum, G., Gerland, S., Chechin, D., and Gascard, J. C. (2014). Advances in understanding and parameterization of small-scale physical processes in the marine Arctic climate system: a review. *Atmospheric Chemistry and Physics*, 14:9403–9450.

Vihma, T., Screen, J., Tjernström, M., Newton, B., Zhang, X., Popova, V., Deser, C., Holland, M., and Prowse, T. (2016). The atmospheric role in the Arctic water cycle: A review on processes, past and future changes, and their impacts. *Journal of Geophysical Research (Biogeosciences)*, 121:586–620.

Walsh, J. E. (2014). Intensified warming of the Arctic: Causes and impacts on middle latitudes. *Global and Planetary Change*, 117:52–63.

Walsh, J. E., Chapman, W. L., and Portis, D. H. (2009). Arctic cloud fraction and radiative fluxes in atmospheric reanalyses. *Journal of Climate*, 22:2316.

Wang, W. and Liang, S. (2009). Estimation of high-spatial resolution clear-sky long-wave downward and net radiation over land surfaces from MODIS data. *Remote Sensing of Environment*, 113(4):745–754.

Wei, T., Ding, M., Wu, B., Lu, C., and Wang, S. (2016). Variations in temperature-related extreme events (1975–2014) in Ny-Ålesund, Svalbard. *Atmospheric Science Letters*, 17(1):102–108.

Weill, A., Eymard, L., Vivier, F., Matulka, A., Loisil, R., Amarouche, N., Panel, J. M., Lourenco, A., Viola, A., Vitale, V., Argentini, S., and Kupfer, H. (2012). First observations of energy budget and bulk fluxes at ny Ålesund (svalbard) during a 2010 transition period as analyzed with the bear station. *ISRN Meteorology*, 2012(675820).

Weinbruch, S., Wiesemann, D., Ebert, M., Schütze, K., Kallenborn, R., and Ström, J. (2012). Chemical composition and sources of aerosol particles at Zeppelin Mountain (Ny-Ålesund, Svalbard): An electron microscopy study. *Atmospheric Environment*, 49:142 – 150.

Wendisch, M., Brückner, M., Burrows, J. P., Crewell, S., Dethloff, K., Lüpkes, C., Macke, A., Notholt, J., Quaas, J., Rinke, A., and Tegen, I. (2017). Understanding causes and effects of rapid warming in the Arctic. *EOS*, 98(8):22–26.

Wendisch, M., Macke, A., Ehrlich, A., Lüpkes, C., Mech, M., Chechin, D., Dethloff, K., Velasco, C. B., Bozem, H., and Brückner, M. (2019). The Arctic cloud puzzle: Using ACLOUD/PASCAL multiplatform observations to unravel the role of clouds and aerosol particles in Arctic amplification. *Bulletin of the American Meteorological Society*, 100(5):841–871.

Wex, H., Huang, L., Zhang, W., Hung, H., Traversi, R., Becagli, S., Sheesley, R. J., Moffett, C. E., Barrett, T. E., and Bossi, R. (2019). Annual variability of ice-nucleating particle concentrations at different Arctic locations. *Atmospheric Chemistry and Physics*, 19(7):5293–5311.

Wild, M., Hakuba, M. Z., Folini, D., Dörig-Ott, P., Schär, C., Kato, S., and Long, C. N. (2019). The cloud-free global energy balance and inferred cloud radiative effects: an assessment based on direct observations and climate models. *Climate Dynamics*, 52(7-8):4787–4812.

Wild, M. and Liepert, B. (2010). The Earth radiation balance as driver of the global hydrological cycle. *Environmental Research Letters*, 5(2):025203.

Winker, D. M., Vaughan, M. A., Omar, A., Hu, Y., Powell, K. A., Liu, Z., Hunt, W. H., and Young, S. A. (2009). Overview of the CALIPSO mission and CALIOP data processing algorithms. *Journal of Atmospheric and Oceanic Technology*, 26(11):2310.

Woods, C. and Caballero, R. (2016). The role of moist intrusions in winter Arctic warming and sea ice decline. *Journal of Climate*, 29:4473–4485.

Wu, B. (2017). Winter atmospheric circulation anomaly associated with recent arctic winter warm anomalies. *Journal of Climate*, 30(21):8469–8479.

Yamanouchi, T. (2018). Arctic warming by cloud radiation enhanced by moist air intrusion observed at Ny-Ålesund, Svalbard. *Polar Science*.

Yeo, H., Park, S.-J., Kim, B.-M., Shiobara, M., Kim, S.-W., Kwon, H., Kim, J.-H., Jeong, J.-H., Park, S. S., and Choi, T. (2018). The observed relationship of cloud to surface longwave radiation and air temperature at Ny-Ålesund, Svalbard. *Tellus B: Chemical and Physical Meteorology*, 70(1):1–10.

Yoshida, Y. and Asano, S. (2005). Effects of the vertical profiles of cloud droplets and ice particles on the visible and near-infrared radiative properties of mixed-phase stratocumulus clouds. *Journal of the Meteorological Society of Japan. Ser. II*, 83(4):471–480.

Yoshimori, M., Abe-Ouchi, A., and Laîné, A. (2017). The role of atmospheric heat transport and regional feedbacks in the Arctic warming at equilibrium. *Climate Dynamics*, 49:3457–3472.

Zängl, G., Reinert, D., Rípodas, P., and Baldauf, M. (2015). The ICON (ICOsahedral Non-hydrostatic) modelling framework of DWD and MPI-M: Description of the non-hydrostatic dynamical core. *Quarterly Journal of the Royal Meteorological Society*, 141:563–579.

Zhang, T., Stamnes, K., and Bowling, S. A. (1996). Impact of Clouds on Surface Radiative Fluxes and Snowmelt in the Arctic and Subarctic. *Journal of Climate*, 9:2110–2123.

Zhang, Y., Rossow, W. B., Lacis, A. A., Oinas, V., and Mishchenko, M. I. (2004). Calculation of radiative fluxes from the surface to top of atmosphere based on ISCCP and other global data sets: Refinements of the radiative transfer model and the input data. *Journal of Geophysical Research (Atmospheres)*, 109(D19):D19105.

Zygmuntowska, M., Mauritsen, T., Quaas, J., and Kaleschke, L. (2012). Arctic Clouds and Surface Radiation - a critical comparison of satellite retrievals and the ERA-Interim reanalysis. *Atmospheric Chemistry and Physics*, 12(14):6667–6677.

Acknowledgements

Erklärung

Ich versichere, daß ich die von mir vorgelegte Dissertation selbständig angefertigt, die benutzten Quellen und Hilfsmittel vollständig angegeben und die Stellen der Arbeit – einschließlich Tabellen, Karten und Abbildungen –, die anderen Werken im Wortlaut oder dem Sinn nach entnommen sind, in jedem Einzelfall als Entlehnung kenntlich gemacht habe; daß diese Dissertation noch keiner anderen Fakultät oder Universität zur Prüfung vorgelegen hat; daß sie – abgesehen von unten angegebenen Teilpublikationen – noch nicht veröffentlicht worden ist sowie, daß ich eine solche Veröffentlichung vor Abschluß des Promotionsverfahrens nicht vornehmen werde. Die Bestimmungen dieser Promotionsordnung sind mir bekannt. Die von mir vorgelegte Dissertation ist von PD. Dr. U. Löhnert betreut worden.

Cologne, 20 January 2020   Tatiana Nomokonova

Teilpublikationen

- Nomokonova T., Ebell K., Löhnert U., Maturilli M., Ritter C., and O'Connor E. (2019), Statistics on clouds and their relation to thermodynamic conditions at Ny-Ålesund using ground-based sensor synergy. *Atmospheric Chemistry and Physics*, vol. 19, no.6, pages 4105-4126, doi: 10.5194/acp-19-4105-2019.

- Nomokonova T., Ebell K., Löhnert U., Maturilli M., and Ritter C. (2019), The influence of anomalous atmospheric conditions at Ny-Ålesund on clouds and their radiative effect. *Atmospheric Chemistry and Physics Discussions*, 1-34, doi: 10.5194/acp-2019-985.

- Nomokonova T., and Ebell, K. (2019), Cloud microphysical properties retrieved from ground-based remote sensing at Ny-Ålesund (10 June 2016 – 8 October 2018). University of Cologne, PANGAEA, `https://doi.pangaea.de/10.1594/PANGAEA.898556`.

- Nomokonova, T., Ritter, C., Ebell, K. (2019), HATPRO microwave radiometer measurements at AWIPEV, Ny-Ålesund (2016 – 2018). PANGAEA, `https://doi.org/10.1594/PANGAEA.902183`.

- Wendisch M. et al. (2019), The Arctic Cloud Puzzle: Using ACLOUD/PASCAL Multi-Platform Observations to Unravel the Role of Clouds and Aerosol Particles in Arctic Amplification, *Bulletin of the American Meteorological Society.*, vol. 100, no.5, pages 841–871, doi:10.1175/BAMS-D-18-0072.1.